

# **MODELLING AND COMPUTATION IN GEOPHYSICAL EXPLORATION**

by

Yile Zhang

A thesis submitted in partial fulfillment of the requirements for the degree of

**Doctor of Philosophy**

in

**Applied Mathematics**

Department of Mathematical and Statistical Sciences

University of Alberta

©Yile Zhang, Winter 2016

# Abstract

Mathematical model and numerical computation play a pivotal role in modern geophysical exploration. By applying computational algorithms to the observed field data, the underground structure can be inferred. This process is generally referred as a geophysical inversion problem. However, due to the model complexity, numerical stability and computing time, solving a geophysical inversion problem is a very challenging task. A typical inversion problem may involve several million of unknowns, and this frequently requires considerable amount of computing time even by using a super-workstation.

This thesis focuses on modelling and developing fast and efficient numerical algorithms for geophysical exploration. By recognizing a Block-Toeplitz Toeplitz-Block (BTTB) structure in a potential field inversion problem and combining the conjugate gradient method with the BTTB structure, a class of efficient numerical schemes are proposed. From the simulation results applied to synthetic and field data, we conclude that the proposed schemes significantly improve the stability and accuracy of a downward continuation problem, and they are more superior to the existing methods. Since a regularization process inherently induces distortion in the inversion solution, we construct a novel non-regularized inversion scheme based on a multigrid (MG) technique. The MG based scheme not only preserves the stability

of a regularization method, but it also induces less distortion in the reconstructed magnetization solution.

We expand our 2D results to a 3D gravity field inversion by proposing a 2D multi-layer model to approximate the density distribution. Based on the multi-layer model, an efficient 3D inversion scheme is proposed, in which all formulation including the regularization, preconditioning and inversion are conducted under a BTTB-based framework. Mathematical analysis for convergence and consistency are presented, and a multi-resolution simulation confirms the efficiency and accuracy of the proposed numerical scheme.

As an indispensable tool in high precision exploration, electromagnetic (EM) method is frequently applied to reconstruct the conductivity distribution. We propose an implicit ADI-FDTD scheme to model the diffusion behavior of the EM wave. The time and space grids in our proposed scheme can be much larger than that used in the conventional Du-Fort-Frankel method, while more accurate numerical solution is obtained. Numerical analysis and computational simulation are presented to demonstrate the effectiveness of the proposed scheme.

# Preface

The research conducted for this thesis forms part of research collaboration with Prof. Yau Shu Wong and Dr. Jian Deng at the University of Alberta, Sha Lei and Julien Lambert at TerraNotes Ltd Geophysics, Prof. Dong Liang at York University, Dr. Wanshan Li at Shandong University, and Yuanfang Lin at East China Normal University. I was the key investigator of all the research projects in Chapters 2-5.

The main results of Chapter 2 of this thesis have been published as Yile Zhang, Yau Shu Wong, Yuanfang Lin, An Improved Conjugate Gradient Method for Downward Continuation of Potential Field Data, *Journal of Applied Geophysics*, 2016, 126, 74 - 86. I was responsible for algorithm design, numerical simulation and manuscript composition, Prof. Yau Shu Wong was involved in the scheme design, numerical analyses and manuscript improvement. Yuanfang Lin was involved in literature study.

The main results of Chapter 3 of this thesis have been published as Yile Zhang, Yau Shu Wong, Jian Deng, Sha Lei, and Julien Lambert, Numerical Inversion Schemes for Magnetization Using Aeromagnetic Data, *International Journal of Numerical Analysis and Modeling*, 2015, 12 (4) 684 - 703. I was responsible for the scheme design, numerical simulation and analysis, and manuscript writing, Prof. Yau Shu Wong provides the idea of the scheme and routine of research, and in-

volved in numerical analysis of simulation results, Dr. Jian Deng, Julien Lambert and Sha Lei were involved in the manuscript improvement, and Sha Lei was responsible for providing the geophysical data.

The main results of Chapter 4 of this thesis have been published as Yile Zhang, Yau Shu Wong, BTTB-based Numerical Scheme for 3D Gravity Field Inversion, *Geophysical Journal International*, 2015, 203(1), 243 - 256. I was responsible for the model construction and algorithm design, theoretical analysis, numerical simulation and manuscript writing. Prof. Yau Shu Wong was involved in algorithm design, numerical analysis for simulation, and manuscript improvement.

The main results of Chapter 5 of this thesis have been published as Wanshan Li, Yile Zhang, Yau Shu Wong and Dong Liang, ADI-FDTD Method for Two-dimensional Transient Electromagnetic Problems, *Communications in Computational Physics*, 2016, 19(1), 94 - 123. I am the corresponding author, and proposed the basic model and corresponding algorithm, I was also responsible for numerical simulation and manuscript writing. Dr. Wanshan Li was responsible for numerical simulation, theoretical proof, and manuscript writing. Prof. Yau Shu Wong gave the idea and the routine of the study, and involved in manuscript improvement. Prof. Dong Liang was involved in manuscript improvement.

# Acknowledgement

As time passing to the completion of my Ph.D study, first and foremost, I would like to express my very great appreciation to my supervisor Prof. Yau Shu Wong. I feel very lucky and grateful of being accepted as his PhD student. He showed me the skills of research, the way of professional presenting and discussion, how to solve mathematical problems from industrial areas and how to form good professional research habits. He always encourages me to pursue a higher goal in life, and provides invaluable suggestions in career planning. I am also very grateful for his careful reading through this long thesis and helping me with the structures, language and typos. The main part of this thesis comes from four papers we collaborated.

I am very grateful to all committee members of my thesis defense for their precious time and valuable work. Especially, I would like to thank Prof. Peter Minev, Prof. Cristina Anton, Prof. Bin Han and Prof. Xinwei Yu, Thanks for your invaluable time and patience for reading through this long thesis.

Special thanks go to my research group colleague Dr. Jian Deng, who always stands by me and give me good idea of research.

Finally, I would like to reserve my gratitude to my parent, Without their support, understanding and love, I would have never completed this thesis and my Ph.D program.

# List of Figures

2.1	Pseudo-magnetic field on the ground level ( $h=0$ m). . . . .	28
2.2	The upward continuation of the pseudo-magnetic field in Figure 2.1 to the elevation of (a) $h=50$ m; (b) $h=250$ m. . . . .	29
2.3	<i>RMS</i> vs $\mu$ graph for (a) TR method; (b) AIT method; (c) BTTB-RRCG method . . . . .	30
2.4	<i>RMS</i> vs $\mu$ graph for TR method under the different level of noise. . . . .	30
2.5	The downward continuation with $\Delta h = 200$ m for the 0.005% noised magnetic field in Figure 2.2(b) by using (a) TR; (b) AIT; (c) TS and (d) BTTB-RRCG method. . . . .	31
2.6	The downward continuation error distribution by (a) TR; (b) AIT; (c) TS and (d) BTTB-RRCG method. . . . .	32
2.7	The downward continuation error distribution for 5% noised data by (a) TR;(b) AIT; (c) BTTB-RRCG method. . . . .	35
2.8	Synthetic density model. . . . .	37
2.9	Generated field by density model in Figure 2.8. . . . .	37
2.10	The downward continuation results by (a) TR;(b) AIT; (c) BTTB-RRCG method. . . . .	38
2.11	The downward continuation error distribution for by (a) TR;(b) AIT; (c) BTTB-RRCG method. . . . .	38
2.12	(a) The real magnetic field data at $h = 0$ m;(b) The upward continuation by $\Delta = 200$ m of the field data in Figure 2.12(a) . . . . .	39
2.13	The downward continuation by $\Delta h = 200$ m for 2.5% noised real field data by (a) TR;(b) AIT; (c) BTTB-RRCG method. . . . .	41
2.14	The downward continuation error distribution for 2.5% noised real field data by (a) TR;(b) AIT; (c) BTTB-RRCG method. . . . .	41
2.15	The downward continuation by $\Delta h = 200$ m after tailoring for 2.5% noised real field data by (a) TR;(b) AIT; (c) BTTB-RRCG method. . . . .	42
2.16	The downward continuation error distribution after tailoring for 2.5% noised real field data by (a) TR;(b) AIT; (c) BTTB-RRCG method. . . . .	43
2.17	Convergence rate of BTTB-RRCG method in the real field data application, where $\mathbf{e} = \ \mathbf{AT}_h - \mathbf{T}_0\ _2$ . . . . .	44
3.1	Forward Model. . . . .	48
3.2	Two-grid and V-cyle MG. . . . .	52
3.3	Initial magnetization distribution. . . . .	56
3.4	Magnetic field data at different depths. . . . .	57

3.5	Convergence rate of CG, RRCG, PCG and MG method at tolerance= $1 * 10^{-3}$ .	60
3.6	Inversion of the magnetic field at $h=250$ m by CG, RRCG, PCG and MG method.	60
3.7	Error vs noise level for the CG, RRCG, PCG and MG method under tolerance= $10^{-2}$ .	62
3.8	Original field data and selected window W.	64
3.9	Test case I.	64
3.10	Inversion results for test case I with tolerance $3 * 10^{-1}$	65
3.11	Inversion result for test case I at depth $h=50$ m	67
3.12	Inversion result for test case I at depth $h=100$ m	68
3.13	Test case II.	69
3.14	Inversion result for test case II at $h = 100$ m.	70
3.15	Inversion result for test case II with tolerance = $1 * 10^{-2}$ .	71
4.1	Uniform splitting of a 3D forward gravity model.	87
4.2	Non-uniform splitting of a 3D forward gravity model.	88
4.3	Synthetic density model I.	99
4.4	Gravity field generated by synthetic model I, unit of the gravity field in mGal.	99
4.5	Inversion result with different constrains.	100
4.6	Inversion result of gravity field without noise and with 2% Gaussian noise.	102
4.7	Synthetic density model II.	102
4.8	Gravity field generated by the synthetic model II.	102
4.9	Inversion result for gravity field in Figure 4.8 with 2% Gaussian noise.	103
4.10	Real gravity field data.	104
4.11	Inversion results at location 1, 2 and 3 in Figure 4.10 at four different resolutions.	105
4.12	The logarithm of the number of unknowns versus the logarithm of the computing time.	105
4.13	Inversion with weighting parameter $\beta = 1.4$	107
4.14	Misfit versus the iteration steps.	107
5.1	Geometry for the 2D TEM problem with the double line source.	115
5.2	Comparison of analytical and numerical solutions computed by the ADI-FDTD and DF schemes for the vertical EMF ( $\partial_t B_z$ ) induced by a double line source on a half-space. Profiles are at (a)0.007 ms, (b)0.1 ms, (c)3 ms, (d)15 ms after the source current was switched off.	135
5.3	Relative $L_\infty$ and $L^2$ errors for the ADI-FDTD and DF schemes	136

5.4	Contours of electric field in a half-space computed by the ADI-FDTD scheme induced by a switched-off 500m wide double line source at the earth-air interface. Profiles are at (a)3 ms, (b)10 ms, (c)15 ms, (d)21 ms after source current was switched off. . . . .	136
5.5	Model geometry for half-space with large-contrast conductor. . . . .	139
5.6	Profiles of the vertical EMF ( $\partial_t B_z$ ) by the ADI-FDTD scheme for the half-space conductor with a 1000:1 contrast. The negative line source is on the right. Open marks indicate negative values and dark marks represent positive ones. . . . .	140
5.7	Profiles of the horizontal EMF ( $\partial_t B_x$ ) by the ADI-FDTD scheme for the half-space conductor with a 1000:1 contrast. The negative line source is on the right. Open marks indicate negative values. . . . .	140
5.8	Contours of electric field(the values are the logarithm of $E$ ) computed by the ADI-FDTD scheme(on the left) and the DF scheme(on the right) for the half-space with the conductor of 1000:1, induced by a switched-off 500m wide double line source at the earth-air interface. . . . .	144
5.9	Model geometry for overburden and half-space with small-contrast conductor. . . . .	146
5.10	Profiles of the vertical EMF ( $\partial_t B_z$ ) by the ADI-FDTD scheme for the half-space with small contrast conductor model. The negative line source is on the right. Open marks indicate negative values and dark marks represent positive ones. . . . .	147
5.11	Profiles of the horizontal EMF ( $\partial_t B_x$ ) by the ADI-FDTD scheme for the half-space with small contrast conductor model. The negative line source is on the right. Open marks indicate negative values. . . . .	147
5.12	Contours of electric field(the values are the logarithm of $E$ ) computed by the ADI-FDTD scheme(on the left) and the DF scheme(on the right) for the half-space with small contrast conductor model, induced by a switched-off 500m wide double line source at the earth-air interface. . . . .	149

# List of Tables

2.1	Computational errors using TR, AIT, TS and BTTB-RRCG methods	33
2.2	Error of downward continuation by using TR, AIT and BTTB-RRCG methods with different level of noise . . . . .	34
2.3	Storage and computing time by conventional and BTTB-RRCG methods . . . . .	35
2.4	Error of downward continuation by using TR, AIT and ITM methods for synthetic gravity data . . . . .	37
2.5	Error by TR, AIT and BTTB-RRCG methods for real field data . . .	43
3.1	Condition number of the coefficient matrix corresponding to different depths. . . . .	56
3.2	Computing time and number of V-cycles of MG with various grid levels. . . . .	57
3.3	Computing time and iteration numbers of various numerical inversion for synthetic data at $h=250m$ . . . . .	59
3.4	Relative error of CG and MG method at different depths and tolerance.	60
3.5	Relative error of CG, RRCG, PG and MG with different noise levels (%). . . . .	62
3.6	Computing time for test case I with tolerance $3 * 10^{-1}$ . . . . .	66
3.7	Computing time for test case I using RRCG and MG . . . . .	66
3.8	The computing time for test case II. . . . .	69
4.1	Computing time for inversion of gravity field real data . . . . .	105
5.1	Time steps in second for the ADI-FDTD and DF schemes . . . . .	134
5.2	CPU time in second for the ADI-FDTD and DF schemes . . . . .	136
5.3	Time steps in second for ADI-FDTD and DF schemes . . . . .	140

# Contents

1. Introduction . . . . .	1
1.1 Inverse source and scattering problem . . . . .	4
1.2 Organization of the Thesis . . . . .	6
2. Downward Continuation for Potential Field . . . . .	9
2.1 Mathematical Background . . . . .	13
2.2 BTTB-RRCG iterative scheme . . . . .	19
2.3 Simulation using synthetic data . . . . .	26
2.4 Applications using real field data . . . . .	39
2.5 Conclusion . . . . .	44
3. Numerical Inversion for Magnetization . . . . .	46
3.1 Magnetic Field Forward Model . . . . .	48
3.2 Numerical Simulations . . . . .	55
3.3 Concluding Remarks . . . . .	72
4. 3D Inversion for Gravity Field Data . . . . .	74
4.1 Gravity Field Forward Model . . . . .	78
4.2 BTTB-based Gravity Inversion . . . . .	86
4.3 BTTB-based regularization . . . . .	92
4.4 Numerical Results . . . . .	98
4.5 Concluding Remarks . . . . .	106
5. ADI-FDTD for 2-D Transient Electromagnetic Problems . . . . .	110
5.1 TEM Model . . . . .	114
5.2 Numerical Formulation for ADI-FDTD with Integral Boundary . . . . .	116
5.3 Stability analysis of ADI-FDTD in $L^2$ norm . . . . .	124
5.4 Convergence analysis of ADI-FDTD . . . . .	130
5.5 Numerical Simulations . . . . .	133
5.6 Concluding Remarks . . . . .	150
6. Conclusion . . . . .	152
Bibliography . . . . .	155

# Chapter 1

## Introduction

Inverse problems form the basis of modern geophysical exploration. In a practical survey, most of the observed fields are produced by natural sources, but artificial sources are frequently used to generate induced fields in some cases [123]. Consider that the underground geology and the external observed geophysical field are linked together by a physical law, it is feasible to infer the underground structure from the observed field.

Predicting the external observable field from given geophysical parameters is called a forward problem. Inversely, inferring the underground geological structure from the observed field is an inverse problem, and the reconstructed solution is an inverse problem solution.

Inverse problem is generally challenging in terms of computation and interpretation [71, 14]. From a numerical prospective, the data obtained from measurement is always polluted due to the fluctuation of the measuring apparatus, therefore an inversion scheme should be robust enough for large perturbation. From a modelling prospective, it is impossible to construct an accurate model for the underground structure since the natural geology can be extremely complex. Assumption

is usually required to keep the mathematical formulation simple. However, such simplification also makes the interpretation more difficult.

An effective way to enhance the inversion solution is to increase the inversion resolution. As a popular method in geophysical exploration, a seismic method possess more flexibility to achieve a high resolution than other methods [69, 39, 81]. By changing the location of a seismic wave field source, plentiful field data can be collected to reduce the uncertain of the underground geology. However, even for a seismic wave method, the accuracy and existence of an inversion solution can not be guaranteed without using a regularization [5].

The regularization is a critical topic in geophysical inversion. The definition of a well-posed problem is given by [48, 123], in which a well-posed mathematical model for a physical problem requires: 1. A solution exists; 2. The solution is unique and 3. The solution changes continuously with the initial conditions. Problems that are not well-posed are ill-posed. We define a general geophysical inversion problem as follows:

$$A(x) = d, x \in M, d \in D, \quad (1.0.1)$$

where  $D$  is the domain of observed data,  $M$  is the domain of geological model,  $A$  is the forward operator generating the data  $d$  from a given model  $x$ . Consider the case of a potential field problem, where the forward operator  $A$  is a linear operator. The observed data is always polluted and resulting a noisy data  $d_\varepsilon$ . Denote the inversion

solution by  $m$ , since the matrix  $A$  in (1.0.1) is usually full, huge and ill-conditioned, the numerical inversion solution  $\tilde{m}$  is sensitive to a small change of  $d_\varepsilon$ . For a non-linear inversion problem including an electromagnetic problem and a seismic wave problem, the non-linearity makes the noise effect even more complicated. It is not hard to conclude that all geophysical inversion problems are ill-posed.

However, an inversion problem which is ill-posed does not imply that the inversion solution of an ill-posed problem is useless. In 1977, Tikhonov proposed a clever way to solve an ill-posed problem [105], in which the problem is approximated by a family of well-posed problems by introducing additional prior information and constraints. Thereafter, the basic idea of a regularization has been developed and extensively applied to all geophysical inversion problems [123]. The regularization is capable of improving the robustness of a numerical scheme regardless of the problem dimension, and it has been reported that regularization is effective for 1D [55], 2D [96] and 3D [119] geophysical inversion problems. Many progress have been made in applying the Tikhonov regularization for geophysical inversion problems. However, in recent years, the geophysical database grows explosively due to the use of aero-survey and sensor techniques. Processing enormous field data is now routinely needed to handle survey from satellite data and high resolution data.

The trend of growing large field data exerts additional challenges to a numerical inversion scheme. Therefore, developing efficient computing methods for geophys-

ical inversion problem is of significance in theoretical study and practical applications. The main goal of this thesis is to make contributions in the following issues:

- (i) How to construct a fast inversion for large scale data without sacrificing the quality of the solution by using a modest computing resource.
- (ii) How to achieve a fast computation for regularization without simplification.
- (iii) How to perform a high-resolution inversion.
- (iv) How to carry out numerical analysis for inversion schemes under the geophysical background.

In the following section, we review the formulation of geophysical problems.

## **1.1 Inverse source and scattering problem**

Geophysical methods are based on studying the observed field generated by different geophysical parameter distributions. The most important geophysical fields are gravity field, magnetic field, electromagnetic field and seismic wave. Although these fields are generated by totally different physical parameters, the inversion process can be classified into two categories.

For the first type, once the underground parameters are fixed, the resulting fields are determined. A typical example is the gravity inversion, where the observed gravity fields are uniquely determined by the underground density distribution. The

forward model can be represented by

$$As = d, \tag{1.1.1}$$

where  $A$  is the forward operator,  $d$  is the observed field, and  $s$  is the parameter distribution that generate the field  $d$ . Note the (1.1.1) is a linear problem, and the parameter  $s$  itself is the source of the field, therefore the corresponding inversion problem is called inverse source problem. Recall that all potential field inversion problems are inverse source problems, and their formulation are usually given in the form of integral equations. The literature review for the source inverse problem can be found in Chapter 3 and Chapter 4.

In the second type of a forward problem, the generated field depends on not only the underground model, but also the imposed artificial source. Electromagnetic (EM) method is the most important scattering method. The secondary field in EM methods is determined by both the induced field and the underground geology consisting of the conductivity and the permeability. This type of inverse problem is called an inverse scattering problem, and can be written in the following form:

$$A(m, s) = d, \tag{1.1.2}$$

where  $m$  is the model parameters,  $s$  is the imposed source. Different from the inverse source problem, the inverse scattering problems are nonlinear problems, and the forward model is always given in terms of differential equations.

For the scattering problem, our study focuses on the electromagnetic problem.

The forward formulation of an electromagnetic problem is based on solving the Maxwell equation, and there are mainly two approaches:

- (i) Apply numerical method such as finite difference (FD), finite element (FE) and integral equation (IE) to solve the problem in time domain and to compute the transient solution directly.
- (ii) Compute the solution in a frequency domain by FD, FE or IE, and then transform the frequency domain solution into the time domain.

A literature review for the EM problems can be found in Chapter 5.

## **1.2 Organization of the Thesis**

The thesis is arranged into five chapters. The first chapter presents a brief introduction of the geophysical inversion problem, and the corresponding time-domain and frequency-domain formulation are reviewed. In the second chapter, a novel computation scheme for a downward continuation is investigated. In a time domain formulation of a downward continuation, the conjugate gradient (CG) method is implemented by utilizing the Block-Toeplitz Toeplitz-Block (BTTB) structure. Unlike a wavenumber domain regularization method, the BTTB-based CG method induces little artifacts near the boundary. The application of a re-weighted regularization in a space domain significantly improves the stability of the CG scheme for noisy data. The synthetic data with different level of noise and real field data are

used to validate the effectiveness of the proposed scheme. The continuation results are compared with recently proposed wavenumber domain methods and the Taylor series method.

In the third chapter, we study the magnetic field inversion problem. We show that a 3D magnetic field formulation can be converted into a 2D form. By constructing a multi-grid scheme, the system matrix preserve the BTTB structure at each grid level. Consequently, the storage and computational complexity can be greatly reduced. Comparing with a regularization method, the multigrid method induces much smaller distortion in an inversion process, and preserve the stability of a regularized method. These properties of the proposed BTTB-MG scheme make it a good alternative to a regularized method when a high accuracy is required for the inversion with perturbed data.

In the forth chapter, a 3D gravity field inversion problem is investigated. First, a novel model for a 3D gravity field formulation is presented, such that the complex 3D density model can be approximated by a sequence of 2D multi-layer models. The proof of the consistency and convergence for the proposed model are given. Differed from a conventional 3D inversion method, the proposed method directly generates a BTTB structure in each 2D layer, such that the 3D inversion scheme is as efficient as a 2D problem. Both regularization and optimal preconditioning operator can be constructed in terms of BTTB structure. Consequently, very efficient solvers can be developed, such that tremendous reduction in storage requirement

and computing time can be achieved. We applied the proposed scheme for real field data to reconstruct 3D underground density distribution under different resolutions.

The fifth chapter focuses on developing efficient numerical computation for electromagnetic forward model. An alternating direction finite-difference time-domain (ADI-FDTD) scheme is proposed for a 2D transverse electric (TE) mode electromagnetic (EM) propagation problem. Unlike the conventional upward continuation approach for the earth-air interface, an integral formulation for the interface boundary is developed and it can effectively incorporate to the ADI solver. Stability and convergence analysis together with an error estimate are presented. Numerical simulations are carried out to validate the proposed method, and the advantage of the present method over the popular Du-Fort-Frankel scheme is clearly demonstrated. The simulations of the electromagnetic field propagation in the ground with anomaly further verify the effectiveness of the proposed scheme.

Finally, it should be mentioned that four scientific papers have been written based on the work reported in this thesis. The four papers have been published in *International Journal of Numerical Analysis and Modeling*, *Geophysical Journal International*, *Communications in Computational Physics* and *Journal of Applied Geophysics*.

## Chapter 2

# Downward Continuation for Potential Field

Downward continuation is frequently applied to enhance the potential field data. It provides geological information at low elevation by using the field data from high elevation. In recent years, the aero-gravity and magnetic survey have been widely used in prospecting [120]. Hence, it is desirable to develop efficient and robust downward continuation methods to deal with large amounts of aero-potential field data. According to the physical law, the potential field data at higher elevation contains dim geophysical information, which makes the data less valuable. The potential field data can be enhanced by using a downward continuation technique, such that the potential field at lower elevation or even underground within the harmonic source-free region [78] can be effectively estimated.

In a wavenumber domain (Fourier spectral domain), the continuation can be carried out by multiplying a continuation factor with the spectrum of the observation data. Unfortunately, the downward continuation factor grows rapidly as the continuation distance increases. The high frequency components including noise in

the observation data will be amplified and thus resulting a severe polluted solution. Therefore, using downward continuation in a wavenumber domain is an inherently unstable process. Using appropriate filters or constrains, stable downward continuation can be constructed. Dean [32] proposed a method to constrain the high frequency components. The use of a Wiener filter is investigated in [20, 79]. Recently, Pavšteka et al. [78] propose a robust wavenumber domain method where the filter is designed based on the characteristics of Tikhonov regularization, Zeng et al. [117] use an adaptive iterative Tikhonov method to apply Tikhonov filter in each iteration in a wavenumber domain. The advantage of a wavenumber domain method is that the downward continuation process can be accelerated by fast Fourier transform (FFT). It has been proved that an appropriate designed filter can guarantee the accuracy and stability of downward continuation even for noisy data [78, 117].

Another type of downward continuation method is based on the Taylor expansion, where the potential field at one elevation can be expanded by the potential field and its vertical derivative terms at another elevation. The success of the Taylor series method depends on the accuracy and stability in computing the vertical derivative terms. Fedi and Florio [36, 35] propose ISVD method, where the odd vertical derivatives can be computed in a stable way, and the even order vertical derivative can be efficiently computed by finite difference. Zhang et al. [118] propose a truncated Taylor series iterative scheme to achieve robust and stable downward continuation. Ma et al [67] compute the downward continuation by adding an

upward continuation and a second vertical derivative at the observation plane, and the scheme can also be converted to an iterative version. The Taylor series method is capable of providing very accurate solution when the data are relatively clean, and the iterative Taylor series method usually has a fast convergence rate.

It should be noted that both the wavenumber domain methods and the Taylor series methods can be accelerated by FFT. However, the FFT itself can induce an artifact, and the FFT-induced artifact can be seen in many existing methods, this is particularly obvious in some iterative wavenumber domain methods [117]. The FFT-induced error in the downward continuation process has already been studied by researchers in [107, 24, 78]. To resolve the difficulty, either extrapolation is needed to extend the original data [78], or a smaller window should be used to exclude the results near the boundary. For the Taylor series methods, besides the FFT-induced error, another problem is the robustness for the noisy data. Although the ISVD method [36, 35] can be applied to compute the odd derivatives in a stable way, but the even derivatives are still computed by the standard finite difference which is sensitive to the noise. Other iterative methods such as that based on the Taylor series has a similar problem [118, 67]. Without a denoising procedure, it is hard to apply the Taylor series methods for the field data with more than 1% noise.

In summary, the FFT produces an efficient computation with the numerical complexity of order  $n \log n$ , where  $n$  is the number of unknowns. To apply the FFT, a continuation process including the regularization is usually converted into

the wavenumber domain. For this reason, regularized downward continuation in a space domain has seldom been investigated. Zhang and Wong [119] propose a numerical scheme for 3D gravity field inversion, where a special algebraic structure called Block-Toeplize Toeplize-Block (BTTB) matrix is utilized to make the scheme efficient.

In this chapter, we consider conjugate gradient (CG) method utilizing the BTTB structure for downward continuation problem. The BTTB structure is derived from the downward continuation formulation in space domain, and it has the same numerical efficiency as the FFT-based methods. However, compared with the FFT-based methods, the proposed method induces very small artifact near the boundary, such that neither extrapolation nor tailoring process are required to reduce the boundary error. This characteristic of the BTTB structure allows the use of an iterative scheme without accumulating the error near the boundary. Combining the BTTB structure with re-weighted regularized conjugate gradient method (BTTB-RRCG), a stable downward continuation method can be constructed. Here, all formulations are in time domain, such that various space domain regularization stabilizers can be applied. We compare the proposed computational scheme with other recently proposed schemes for downward continuation. The simulation results for synthetic and field data demonstrate that the proposed scheme is more accurate and robust for applications using clean and noisy data.

In section 2.1, the formulation of downward continuation is presented. We

briefly introduce the Tikhonov regularized method (TR) [78], adaptive iterative Tikhonov method (AIT) [117], and stable iterative Taylor series method (ITS) [67]. Section 2.2 focuses on the proposed BTTB-RRCG scheme. In Section 2.3, synthetic field data are used to validate the proposed numerical scheme, and the result is compared with those obtained by TR, AIT and ITS methods. A Gaussian noise from 0.1% to 5% of the maximum magnitude of the synthetic data are added to test the robustness. The error are analyzed by using RMS and the relative error in terms of  $L_2$  norm and  $L_\infty$  norm. Particularly, the FFT-induced error near the boundary is investigated. In section 2.4, we apply the proposed scheme to the field data, and similar to the synthetic case, the result is compared with other existing methods.

## 2.1 Mathematical Background

The relationship between the potential field data at two observation planes is given by [117]:

$$\mathbf{T}(x, y, h_0) = \frac{h_0 - h}{2\pi} \int_{-\infty}^{\infty} \int_{-\infty}^{\infty} \frac{\mathbf{T}(x', y', h) dx' dy'}{[(x - x')^2 + (y - y')^2 + (h - h_0)^2]^{3/2}}, \quad (2.1.1)$$

where  $x$  and  $y$  are the horizontal coordinates,  $\mathbf{T}(x, y, h_0)$  is the observation field at higher elevation  $h_0$ , and  $\mathbf{T}(x, y, h)$  is the unknown field at lower elevation  $h$  such that  $h_0 > h$ . The downward continuation process is to seek  $\mathbf{T}(x, y, h)$  at lower elevation from the potential field  $\mathbf{T}(x, y, h_0)$  at higher elevation.

Denote the kernel as  $\mathbf{K}$ , the integral equation (2.1.1) can be converted into the

following convolution form

$$\mathbf{T}(x, y, h_0) = \int_{-\infty}^{\infty} \int_{-\infty}^{\infty} \mathbf{K}(x - x', y - y', h_0 - h) \mathbf{T}(x', y', h) dx' dy', \quad (2.1.2)$$

which can be further simplified as

$$\mathbf{T}(h_0) = \mathbf{K} * \mathbf{T}(h), \quad (2.1.3)$$

where  $*$  denotes the convolution. According to the convolution theorem,

$$\mathcal{F}(\mathbf{T}(h_0)) = \mathcal{F}(\mathbf{K} * \mathbf{T}(h)) = \mathcal{F}(\mathbf{K}) \cdot \mathcal{F}(\mathbf{T}(h)), \quad (2.1.4)$$

therefore,

$$\mathbf{T}(h_0) = \mathcal{F}^{-1}(\mathcal{F}(\mathbf{K}) \cdot \mathcal{F}(\mathbf{T}(h))). \quad (2.1.5)$$

Since

$$\mathcal{F}(\mathbf{K}) = \int_{-\infty}^{\infty} \int_{-\infty}^{\infty} \mathbf{K}(x, y) e^{-2\pi i(ux+vy)} dx dy = e^{-(h_0-h)\sqrt{u^2+v^2}}, \quad (2.1.6)$$

denote  $\mathbf{T}(h_0)$  and  $\mathbf{T}(h)$  by  $\mathbf{T}_{h_0}$  and  $\mathbf{T}_h$ , respectively, then equation (2.1.3) can be rewritten into the following matrix form

$$\mathbf{T}_{h_0} = \mathbf{F}^{-1} \Lambda \mathbf{F} \mathbf{T}_h, \quad (2.1.7)$$

where  $\mathbf{F}$  and  $\mathbf{F}^{-1}$  are the Fourier matrices corresponding to a 2D Fourier transform, and  $\Lambda$  is the continuation kernel  $\mathbf{K}$  in the wavenumber domain given by (2.1.6).

Consider for  $h_0 - h > 0$ , the kernel  $e^{-(h_0-h)\sqrt{u^2+v^2}}$  is stable, since the high frequen-

cy component can be compressed. This explains why an upward continuation is a stable process.

According to (2.1.7), the most straightforward way to conduct the downward continuation is

$$\mathbf{T}_h = \mathbf{F}^{-1}\Lambda^{-1}\mathbf{F}\mathbf{T}_{h_0}, \quad (2.1.8)$$

where  $\Lambda^{-1}$  is given by  $e^{(h_0-h)\sqrt{u^2+v^2}}$ . Obviously, since  $h_0 - h > 0$ , the kernel given by  $e^{(h_0-h)\sqrt{u^2+v^2}}$  will amplify all frequency components in  $\mathbf{T}_{h_0}$ , such that the solution of  $\mathbf{T}_h$  will be polluted by the high frequency component or noise in  $\mathbf{T}_{h_0}$ . Denote  $\mathbf{T}_h$  by  $\mathbf{T}$ , (2.1.8) can be rewritten into a simplified form as

$$\hat{\mathbf{T}} = \Lambda^{-1}\hat{\mathbf{T}}_{h_0}, \quad (2.1.9)$$

where  $\hat{\mathbf{T}}$  and  $\hat{\mathbf{T}}_{h_0}$  are the potential field in wavenumber domain with heights  $h$  and  $h_0$ .

According to the analysis above, the downward continuation is an inherently unstable process, and conventionally, there are mainly two approaches to resolve this issue: Tikhonov regularization in wavenumber domain and the Taylor series method.

### 2.1.1 Wavenumber domain Tikhonov regularization method

Let us denote the downward continuation formulation (2.1.1) into the following form:

$$\mathbf{T}_{h_0} = \mathbf{A}\mathbf{T}, \quad (2.1.10)$$

where  $\mathbf{A}$  is the upward continuation operator. As we have discussed early, solving (2.1.10) is an ill-posed problem, which is equivalent to compute (2.1.9). Tikhonov and Arsenin [105] proposed an effective way to solve this kind of problem. Instead of solving (2.1.10) directly, they converted the problem into the following minimization problem:

$$\min\{\|\mathbf{W}_d(\mathbf{A}\mathbf{T} - \mathbf{T}_{h_0})\|^2 + \mu\|\mathbf{W}_m(\mathbf{T} - \mathbf{T}_{\text{ref}})\|^2\}, \quad (2.1.11)$$

where  $\mu$  is the regularization parameter,  $\mathbf{W}_d$  and  $\mathbf{W}_m$  are the data weighting matrix and model weighting matrix, respectively,  $\mathbf{T}_{\text{ref}}$  is the prior information, and  $\|\cdot\|$  denotes the L2-norm. In a downward continuation,  $\mathbf{T}_{\text{ref}}$  is usually a zero vector. Let  $\mathbf{W}_d$  and  $\mathbf{W}_m$  be the identity matrix, then the solution of (2.1.11) can be given by

$$\mathbf{T}_{\text{Tik}} = (\mathbf{A}^T\mathbf{A} + \mu\mathbf{I})^{-1}\mathbf{A}^T\mathbf{T}_{h_0}. \quad (2.1.12)$$

Convert (2.1.12) into a wavenumber domain, we have [117]:

$$\hat{\mathbf{T}}_{\text{Tik}} = \frac{\Lambda^2}{\Lambda^2 + \mu}\Lambda^{-1}\hat{\mathbf{T}}_{h_0} = \hat{\mathbf{L}}_{\text{Tik}}\Lambda^{-1}\hat{\mathbf{T}}_{h_0}. \quad (2.1.13)$$

Compare (2.1.13) with (2.1.9), it can be seen that  $\hat{\mathbf{L}}_{\text{Tik}}$  is the Tikhonov regularization filter in a wavenumber domain, which is given by

$$\hat{\mathbf{L}}_{\text{Tik}} = \frac{e^{-2\Delta h\sqrt{u^2+v^2}}}{e^{-2\Delta h\sqrt{u^2+v^2}} + \mu}. \quad (2.1.14)$$

where  $\Delta h = h_0 - h$  is the downward continuation distance.

Based on (2.1.14), Zeng et al. [117] proposed an iterative Tikhonov scheme in the following form:

$$\hat{\mathbf{T}}_n = \hat{\mathbf{T}}_{n-1} + \frac{e^{-2\Delta h\sqrt{u^2+v^2}}}{e^{-2\Delta h\sqrt{u^2+v^2}} + \mu} \Lambda^{-1} \hat{\mathbf{R}}_{n-1}, \quad (2.1.15)$$

with the initial value  $\mathbf{T}_0$  is given by  $\hat{\mathbf{T}}_0 = \hat{\mathbf{L}}_{\text{Tik}} \Lambda^{-1} \hat{\mathbf{T}}_{h_0}$ ,  $\hat{\mathbf{R}}_n = \hat{\mathbf{T}}_{h_0} - \Lambda^{-1} \hat{\mathbf{T}}_n$ .

Actually, the Tikhonov regularization (2.1.11) may have different forms with different Tikhonov regularization stabilizers. Applying the Tikhonov formulation given in [106], Pasteka et al. [78] proposed another efficient Tikhonov regularization filter in a wavenumber domain in the form of

$$\hat{\mathbf{L}}_{\text{Tik}} = \frac{1}{1 + \mu(u^2 + v^2)e^{\Delta h\sqrt{u^2+v^2}}}. \quad (2.1.16)$$

Our numerical simulations show that as a one-step Tikhonov regularization filter, (2.1.16) is better than (2.1.14) in the robustness and accuracy, while the iterative version of (2.1.14) is slightly better than (2.1.16).

### 2.1.2 Taylor series methods

Differed from the FFT-based iterative method, the Taylor series method is to express the potential field at the elevation  $h$  by the potential field at another elevation  $h_0$  as

$$\mathbf{T}(x, y, h) = \mathbf{T}(x, y, h_0) + \frac{\partial \mathbf{T}(x, y, h_0)}{\partial z} \Delta h + \frac{1}{2!} \frac{\partial^2 \mathbf{T}(x, y, h_0)}{\partial z^2} \Delta h^2 + \dots + \frac{1}{m!} \frac{\partial^m \mathbf{T}(x, y, h_0)}{\partial z^m} \Delta h^m, \quad (2.1.17)$$

where  $\Delta h = h_0 - h$ .

The ISVD method proposed by Fedi and Florio [36, 35] uses vertical integrating the field in a wavenumber domain to compute the odd vertical derivative, which has a good stability for noisy data. Ma et al. [67] introduced a method to remove the odd derivative from the Taylor formulation in the following form

$$\mathbf{T}(x, y, h) \approx 2\mathbf{T}(x, y, h_0) - \mathbf{T}(x, y, h_0 + \Delta h) + \frac{\partial^2 \mathbf{T}(x, y, h_0)}{\partial z^2} h_0^2, \quad (2.1.18)$$

where  $\mathbf{T}(x, y, h_0 + \Delta h)$  is the upward continuation of the observation field  $T(x, y, h_0)$  with a continuation distance  $\Delta h$ . Recall that an upward continuation is a stable process, therefore the downward continuation scheme (2.1.18) based on upward continuation should be stable.

Both the ISVD method and Taylor formulation (2.1.18) requires computing the second vertical derivative by a finite difference. From the Laplace equation, the second vertical derivative can be computed by a second order horizontal derivative in  $x$  and  $y$  direction. Although finite differencing is an efficient way to compute the

horizontal derivative [36], it is sensitive to noisy data. In our simulation, assume the grid size is given by  $h$  and to reduce the error to minimum, we apply a second order central scheme (2.1.19) to compute the second horizontal derivative in the interior, and the second order forward scheme (2.1.20) to compute the second horizontal derivative on the boundary, such that the overall numerical derivative is of second order accuracy.

$$f''(x) = \frac{f(x+h) - 2f(x) + f(x-h)}{h^2} \quad (2.1.19)$$

$$f''(x) = \frac{f(x+2h) - 2f(x+h) + f(x)}{h^2} \quad (2.1.20)$$

## 2.2 BTTB-RRCG iterative scheme

We now present a new approach for a downward continuation. Instead of converting the downward continuation formulation into a wavenumber domain as in (2.1.6), we work with a space domain formulation and discretize (2.1.1) as

$$T(x(i), y(i), h_0) = \sum_{j=1}^N \sum_{k=1}^M G(x(i), y(i), x'(j), y'(k), h_0 - h) T(x'(j), y'(k), h) \Delta x \Delta y, \quad i = 1, 2, \dots, N * M, (2.2.1)$$

where  $h_0$  and  $h$  are defined as before,  $N$  and  $M$  are the number of data grids in the  $x$  and  $y$  direction,  $\Delta x$  and  $\Delta y$  are the grid interval in the  $x$  and  $y$  direction. Denote the data points on the lower plane indicated by  $T(x'(i), y'(j), h)$ , where  $i = 1, \dots, N$ ,  $j = 1, \dots, M$ . Renumbering the data grids to  $T(x'(l), y'(l), h)$ ,

where  $l = 1, \dots, N * M$ , which means that we rearrange the index of the data without changing the total number of data points.

Thus, (2.2.1) can be rewritten as

$$T(x(i), y(i), h_0) = \sum_{l=1}^{N \times M} G(x(i), y(i), x'(l), y'(l), h_0 - h) T(x'(l), y'(l), h) \Delta x \Delta y, \quad i = 1, 2, \dots, N * M, \quad (2.2.2)$$

where

$$G(i, l, h) = \frac{h_0 - h}{[(x(i) - x(l))^2 + (y(i) - y(l))^2 + (h - h_0)^2]^{\frac{3}{2}}}. \quad (2.2.3)$$

By (2.2.2) and (2.2.3), the original downward continuation formulation (2.1.1) can be approximated by the linear system

$$\mathbf{T}_0 = \mathbf{GT}. \quad (2.2.4)$$

Here,  $\mathbf{T}_0$  is the discretized observation field,  $\mathbf{T}$  is the unknown field data, and  $\mathbf{G}$  is a  $(N \times M)$  by  $(N \times M)$  BTTB matrix generated from the discretization (2.2.2).

The BTTB matrix is given in the following form:

$$\mathbf{G}_{MN} = \begin{bmatrix} \mathbf{G}_{(0)} & \mathbf{G}_{(-1)} & \cdots & \mathbf{G}_{(2-M)} & \mathbf{G}_{(1-M)} \\ \mathbf{G}_{(1)} & \mathbf{G}_{(0)} & \mathbf{G}_{(-1)} & \cdots & \mathbf{G}_{(2-M)} \\ \vdots & \mathbf{G}_{(1)} & \mathbf{G}_{(0)} & \ddots & \vdots \\ \mathbf{G}_{(M-2)} & \cdots & \ddots & \ddots & \mathbf{G}_{(-1)} \\ \mathbf{G}_{(M-1)} & \mathbf{G}_{(M-2)} & \cdots & \mathbf{G}_{(1)} & \mathbf{G}_{(0)} \end{bmatrix}, \quad (2.2.5)$$

in which each block  $\mathbf{G}_{(m)}$  is a Toeplitz matrix given by

$$\mathbf{G}_{(m)} = \begin{bmatrix} g_0^{(m)} & g_{-1}^{(m)} & \cdots & g_{2-N}^{(m)} & g_{1-N}^{(m)} \\ g_1^{(m)} & g_0^{(m)} & g_{-1}^{(m)} & \cdots & g_{2-N}^{(m)} \\ \vdots & g_1^{(m)} & g_0^{(m)} & \ddots & \vdots \\ g_{N-2}^{(m)} & \cdots & \ddots & \ddots & g_{-1}^{(m)} \\ g_{N-1}^{(m)} & g_{N-2}^{(m)} & \cdots & g_1^{(m)} & g_0^{(m)} \end{bmatrix}, \quad m = 0, 1, \dots, M-1, \quad (2.2.6)$$

where  $g_i$  is constant along its diagonals and the value is defined by (2.2.3).

One important property of a BTTB matrix is that the first row and the first column contain all information of a given matrix. Consequently, for the matrix  $\mathbf{G}$  given by (2.2.5), we only need to store the first row and first column, such that the storage requirement for the sensitivity matrix can be dramatically reduced from  $(N * M)^2$  to  $2(N * M)$ . It should be noted that for the downward continuation problem, the BTTB matrix is always a symmetric matrix regardless of the choice for  $\Delta x$  and  $\Delta y$ . Hence, the storage requirement for the sensitivity matrix is further reduced to  $N * M$ .

Another important feature of BTTB structure is that any BTTB matrix can be embedded into a Block-Circulant Circulant-Block (BCCB) matrix as [15]:

$$\mathbf{C}_{MN} = \begin{bmatrix} \mathbf{G}_{MN} & \times \\ \times & \mathbf{G}_{MN} \end{bmatrix}, \quad (2.2.7)$$

such that the matrix-vector product for any BTTB matrix can be computed via

$$\begin{bmatrix} \mathbf{G}_{MN} & \times \\ \times & \mathbf{G}_{MN} \end{bmatrix} \begin{bmatrix} \mathbf{T} \\ \mathbf{0} \end{bmatrix} = \begin{bmatrix} \mathbf{G}_{MN} \mathbf{T} \\ \dagger \end{bmatrix}, \quad (2.2.8)$$

where  $\times$  is the BTTB matrix determined by  $\mathbf{G}_{MN}$ ,  $\mathbf{T}$  is a vector as defined in (2.2.4),  $\mathbf{0}$  is a zero vector with the same dimension as  $\mathbf{T}$ , and  $\dagger$  is the part to be dropped. The details of this operation can be found in [15].

The embedding of BTTB matrix in (2.2.7) is very critical. It is known [31] that the BCCB matrix  $\mathbf{C}$  can be diagonalized by the Fourier matrix  $\mathbf{F}$  and its conjugate transpose, i.e.,

$$\mathbf{C} = \mathbf{F}^* \hat{\Lambda} \mathbf{F}, \quad (2.2.9)$$

where  $\mathbf{F}$  is the Fourier matrix. Recall that  $\mathbf{F}$  in (2.1.8) is the Fourier transform operator. Applying the Fourier transform operator to a given matrix is equivalent to performing a premultiplication between Fourier matrix and the given matrix [15].

The Fourier matrix is given as:

$$(F_n)_{j,k} = \frac{1}{\sqrt{n}} e^{\frac{2\pi i j k}{n}}, \quad i = \sqrt{-1} \quad (2.2.10)$$

for  $0 \leq j, k \leq n - 1$ .

It should be noted that  $\hat{\Lambda}$  in (2.2.9) is totally different from  $\Lambda$  in (2.1.7). Recall in (2.1.7),  $\Lambda$  is the downward continuation kernel in a wavenumber domain, and it can be computed by (2.1.6). However,  $\hat{\Lambda}$  in (2.2.9) is the eigenvalues of  $\mathbf{C}$ , and it

has different dimension from  $\Lambda$ .

The computation of  $\hat{\Lambda}$  in (2.2.9) is different from computing  $\Lambda$  in (2.1.6). For an  $n$  by  $n$  circulant matrix  $\mathbf{C}$ , the  $\hat{\Lambda}$  can be computed via FFT by observing the first column of  $F_n$  is  $\frac{1}{\sqrt{n}}\mathbf{1}_n$ , where  $\mathbf{1}_n = (1, 1, \dots, 1)^T \in \mathbb{R}^n$  is the vector consisting of all ones. Let  $\mathbf{e}_1 = (1, 0, \dots, 0)^T \in \mathbb{R}^n$ , then by using (2.2.9), we have

$$\mathbf{F}_n \mathbf{C}_n \mathbf{e}_1 = \frac{1}{\sqrt{n}} \Lambda_n \mathbf{1}_n, \quad (2.2.11)$$

which implies that  $\hat{\Lambda}$  can be computed by applying fast Fourier transform to  $\mathbf{C}$ .

The BTTB matrix has many other attractive properties including the construction for an efficient preconditioner, and recent work on preconditioners has been reported in [15].

Now the downward continuation problem (2.1.1) is converted into solving the linear system (2.2.4). Similar to a wavenumber domain method, the Tihonov regularization (2.1.12) can also be applied. In this study, we consider using the conjugate gradient type method to solve the regularization problem (2.1.12), since theoretically it has a rapid rate of convergence [3]. Compared with the steepest decent method [114, 117], which can be regarded as first order gradient method, the conjugate gradient method is a second order gradient method. Combining the BTTB property (2.2.9) and (2.2.8) with the RRCG scheme in [123], we develop a BTTB-RRCG scheme. The details of the standard RRCG scheme can be found in [123]:

**RRCG.** For the minimization problem given in (2.1.11), denote the observation

field  $\mathbf{T}_{h_0}$  by  $\mathbf{d}$ , and the potential field at the target plane  $\mathbf{T}_h$  by  $\mathbf{m}$ . Let  $\mathbf{m}_0$  be an initial approximation,  $\alpha_0$  be the initial regularization parameter. The re-weighted regularized conjugate gradient (RRCG) algorithm is given as follows.

$$\mathbf{r}_0 = \mathbf{A}\mathbf{m}_0 - \mathbf{d}, \quad \mathbf{s}_0 = \mathbf{W}_m(\mathbf{m}_0 - \mathbf{m}_{\text{ref}}),$$

$$\mathbf{I}_0^{\alpha_0} = \mathbf{I}^{\alpha_0}(\mathbf{m}_0) = \mathbf{A}^T \mathbf{W}_d^2 \mathbf{r}_0 + \alpha_0 \mathbf{W}_m \mathbf{s}_0,$$

for  $n = 1, 2, 3 \dots$

$$\mathbf{r}_n = \mathbf{A}\mathbf{m}_n - \mathbf{d}, \quad \mathbf{s}_n = \mathbf{W}_m(\mathbf{m}_n - \mathbf{m}_{\text{ref}}),$$

$$\mathbf{I}_n^{\alpha_n} = \mathbf{I}^{\alpha_n}(\mathbf{m}_n) = \mathbf{A}^T \mathbf{W}_d^2 \mathbf{r}_n + \alpha_n \mathbf{W}_m \mathbf{s}_n,$$

$$\beta_n^{\alpha_n} = \|\mathbf{I}_n^{\alpha_n}\|^2 / \|\mathbf{I}_{n-1}^{\alpha_{n-1}}\|^2,$$

$$\tilde{\mathbf{I}}_n^{\alpha_n} = \mathbf{I}_n^{\alpha_n} \tilde{\mathbf{I}}_{n-1}^{\alpha_{n-1}}, \quad \tilde{\mathbf{I}}_0^{\alpha_0} = \mathbf{I}_0^{\alpha_0},$$

$$\tilde{k}_n^{\alpha_n} = (\tilde{\mathbf{I}}_n^{\alpha_n T} \tilde{\mathbf{I}}_n^{\alpha_n}) / \left[ \tilde{\mathbf{I}}_n^{\alpha_n T} (\mathbf{A}^T \mathbf{W}_d^2 \mathbf{A} + \alpha \mathbf{W}_m^2) \tilde{\mathbf{I}}_n^{\alpha_n} \right],$$

$$\mathbf{m}_{n+1} = \mathbf{m}_n - \tilde{k}_n^{\alpha_n} \tilde{\mathbf{I}}_n^{\alpha_n}, \quad \gamma = \|\mathbf{s}_{n+1}\|^2 / \|\mathbf{s}_n\|^2,$$

$$\alpha_{n+1} = \begin{cases} \alpha_n & \text{if } \gamma \leq 1 \\ \alpha_n / \gamma & \text{if } \gamma > 1 \end{cases}$$

By combining the discretization process and the properties of BTTB matrix with the RRCG algorithm, the BTTB-RRCG algorithm is given as follows:

**BTTB-RRCG.** For the downward continuation problem (2.1.10), denote the observation field  $\mathbf{T}_{h_0}$  by  $\mathbf{d}$ , and the potential field at the target plane  $\mathbf{T}_h$  by  $\mathbf{m}$ .

*Step 1.* Discretize the upward continuation operator (2.1.1) by using (2.2.2).

*Step 2.* Generate the matrix  $\mathbf{G}$  in (2.2.4) in the form of (2.2.5), and a compact storage format is used to store  $\mathbf{G}$ .

*Step 3.* Choose an appropriate regularization in time domain, and convert the problem (2.2.4) into a minimization problem (2.1.11). The regularization stabilizer is also in the form of BTTB matrix.

*Step 4.* Apply the RRCG algorithm mentioned above to the minimization problem. In each operation, the system matrix  $\mathbf{G}$  is embedded into a BCCB matrix as in (2.2.8), such that the matrix-vector product can be conducted by using (2.2.9) and (2.2.11).

The details of the compact storage in step 2 can be found in [15], and the regularization stabilizer in terms of BTTB structure has been reported in [119].

The initial regularization parameter  $\alpha_0$  is chosen according to a trial and error method. It should be noted that when the field data is clean without noise, the BTTB-CG method should have a better performance than the BTTB-RRCG method, since the regularization itself will inevitably introduce certain degree of distortion in the downward continuation solution. On the other hand, it has been shown that by applying a regularization, the stability of the gradient type methods can be greatly improved [123, 117].

Note that by using BTTB-RRCG algorithm proposed above, we can always find a unique solution of the minimization problem (2.1.11) by the following theorem:

**Theorem 1.1** [122]: Let  $A$  be an arbitrary linear continuous operator, acting from a complex Hilbert space  $M$  to a complex Hilbert space  $D$ , and  $W$  be an absolutely positively determined (APD) linear continuous operator in  $M$ . Then the Tikhonov

parametric functional

$$P^\alpha(m) = \|A\mathbf{m} - d\|^2 + \alpha\|W\mathbf{m}\|^2$$

has a unique minimum,  $m_\alpha \in M$ , and the regularized gradient type method converges to this minimum for any initial approximation  $m_0 : m_n \rightarrow m_\alpha, n \rightarrow \infty$ .

According to Theorem 1,1, the solution of proposed BTTB-RRCG is unique and convergent for any initial guess. In the next section, we will verify the proposed scheme by using synthetic and field data, and investigate the sensitivity of regularization parameter  $\alpha$  in the proposed BTTB-RRCG method.

## 2.3 Simulation using synthetic data

To validate the proposed BTTB-RRCG scheme, we now consider a test case with a synthetic magnetic field data. The computation is carried out by a laptop with i7-3630 CPU and 12G RAM. The numerical results will be compared with those obtained by the Tikhonov regularized method (TR) [78], the adaptive iterative Tikhonov method (AIT) [117] and the iterative Taylor series method (ITS) [67].

We consider two synthetic tests in this section. By tradition, the synthetic field is generated by a 3D synthetic susceptibility or density model. However, in the first synthetic test, we present another approach. First, we design a pseudo-magnetic field on the ground level ( $h = 0$  m), and we refer this to a pseudo-magnetic field since it is not generated by a 3D susceptibility model. Then, we realize an upward

continuation of the pseudo-magnetic field on the ground level to two different elevations  $h_1$  and  $h_2$  generating two synthetic fields  $\mathbf{T}_{h_1}$  and  $\mathbf{T}_{h_2}$ , where  $h_2 > h_1$ . Finally, we conduct a downward continuation for  $\mathbf{T}_{h_2}$  with a continuation distance  $\Delta h = h_2 - h_1$ , such that an inferred potential field  $\tilde{\mathbf{T}}_{h_1}$  can be estimated. By comparing  $\tilde{\mathbf{T}}_{h_1}$  with  $\mathbf{T}_{h_1}$ , and evaluating the statistics of the difference between  $\tilde{\mathbf{T}}_{h_1}$  and  $\mathbf{T}_{h_1}$ , we study the characteristics of the downward continuation.

Performing the synthetic downward continuation simulation in such way is reasonable, because we do not really need to compute the underground 3D susceptibility distribution. Moreover, it has been shown that with some assumptions, the 3D susceptibility distribution can be simplified into a 2D case [120]. Therefore, a pseudo-magnetic field distribution is sufficient. More importantly, we can now design the distribution of the magnetic field and include anomalies with various frequency components and anomalies near the boundary, such that the edge-effect can be investigated. However, in a traditional approach, the 3D susceptibility model is always in the interior of the model domain, and the generated field has a very small or zero value near the boundary. Consequently, there is almost no edge-effect in the computation. The synthetic field data is too simple to evaluate the performance of a downward continuation scheme for test cases with real field data, in which the fields are usually complicated near the boundary. The design of a pseudo-magnetic field on the ground level is also much more convenient than constructing a complicated 3D susceptibility distribution.

The pseudo-magnetic field on the ground level is shown in Figure 2.1, where  $\Delta x = \Delta y = 9.98$  m. The synthetic field contains two semi-circle anomalies on the upper left and lower right boundaries, and there is no other anomaly near the boundary. In the interior of the synthetic field, there are two circle anomalies with sharp boundary variation and a swirl shape anomaly with two shape corners. The synthetic field is designed to include the field variation with different frequencies, and the two semi-circle on the boundary is used to investigate the edge-effect of the scheme.

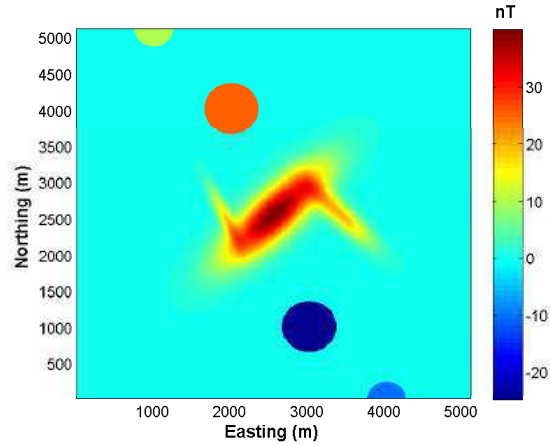


Figure 2.1: Pseudo-magnetic field on the ground level ( $h=0$  m).

We now conducted an upward continuation to the synthetic field as shown in Figure 2.1 with a continuation distance  $\Delta h = 50$  m and  $\Delta h = 250$  m, where the  $\mathbf{T}_{50}$  and  $\mathbf{T}_{250}$  are shown in Figure 2.2(a) and 2.2(b), respectively. Then, we carry out a downward continuation for the field at  $h = 250$ m as illustrated in Figure 2.2 with a continuation distance  $\Delta h = 200$  m, and the performance of the computational scheme can be evaluated by comparing the downward continuation field  $\tilde{\mathbf{T}}_{50}$  and

$\mathbf{T}_{50}$ . Note that the field data is slightly perturbed by adding 0.005% Gaussian noise to the maximum of the magnitude of  $\mathbf{T}_{250}$ .

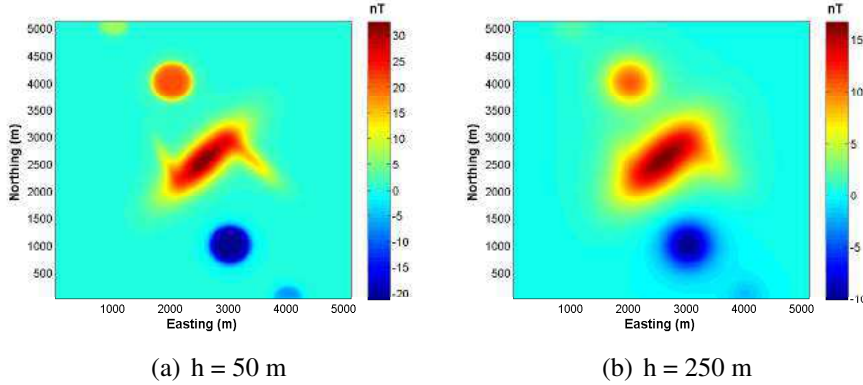


Figure 2.2: The upward continuation of the pseudo-magnetic field in Figure 2.1 to the elevation of (a)  $h=50$  m; (b)  $h=250$  m.

For the regularization parameters, an optimal regularization parameter can be determined using the  $C - norm$  method [78]. However, to compare with different regularization methods, we apply a straightforward procedure to evaluate the optimal regularization parameter  $\mu$  in the TR, AIT and BTTB-CG methods by plotting the  $RMS$  of the downward continuation error with different  $\mu$ , where the  $RMS$  is defined in (2.3.1). Since the exact downward continuation result is known, the value of  $\mu$  is obviously optimal. The  $RMS$  vs  $\mu$  curves for the TR, AIT and BTTB-RRCG method are shown in Figure 2.3.

In this study, optimal parameters used in the simulation are  $\mu_{TR} = 514$ ,  $\mu_{AIT} = 0.0157$ ,  $\mu_{RRCG} = 0.095$ . We have considered data with different level of noise from 0% to 5%. However, the optimal value for  $\mu$  is almost the same, since the optimal regularization parameter is not sensitive when the noise level is less than or equal

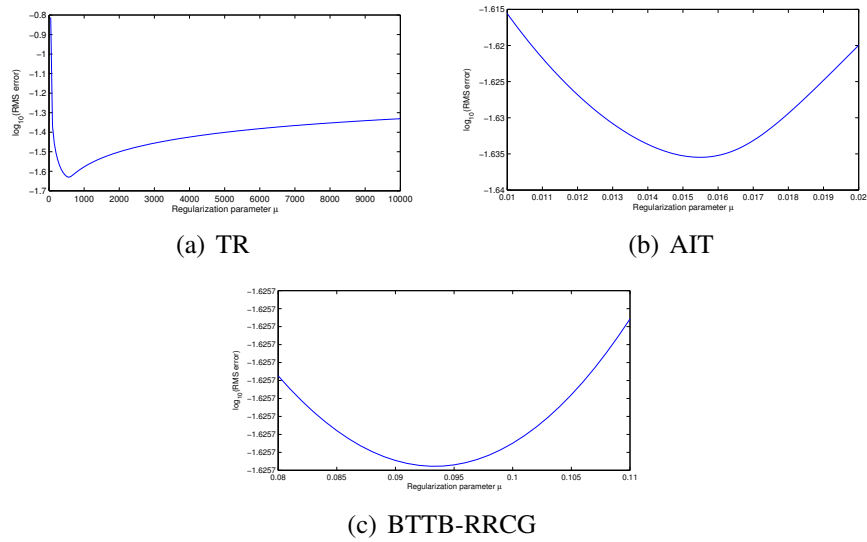


Figure 2.3:  $RMS$  vs  $\mu$  graph for (a) TR method; (b) AIT method; (c) BTTB-RRCG method

to 5%, and this has been confirmed for TR, AIT and BTTB-RRCG method. Using TR method as an example and introducing 0%, 2% and 4% noise to the data, we plot the  $RMS$  vs  $\mu$  graph as shown in Figure 2.4. It can be seen that the optimal regularization parameters for the data with different noise level are between 500 to 600, which are very similar.

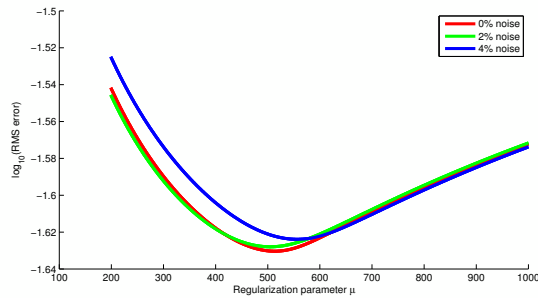


Figure 2.4:  $RMS$  vs  $\mu$  graph for TR method under the different level of noise.

The optimal iteration of AIT is 2 from a trial and error method, and it should be

noted that with more iterations used, the results deteriorate. By plotting the residue defined by  $\mathbf{e} = \|\mathbf{AT}_h - \mathbf{T}_0\|_2$  vs iteration number  $N$ , we can estimate the iteration numbers in the BTTB-RRCG. For the ITS method, once the noise is added, the iteration will amplify the noise if no denoising filter is applied. Therefore, we only consider a non-iterative version for ITS, and we rename the method as TS in the following. The downward continuation results for the field in Figure 2.2(b) with 0.005% Gaussian noise by TR, AIT, TS and BTTB-RRCG methods are illustrated in Figure 2.5.

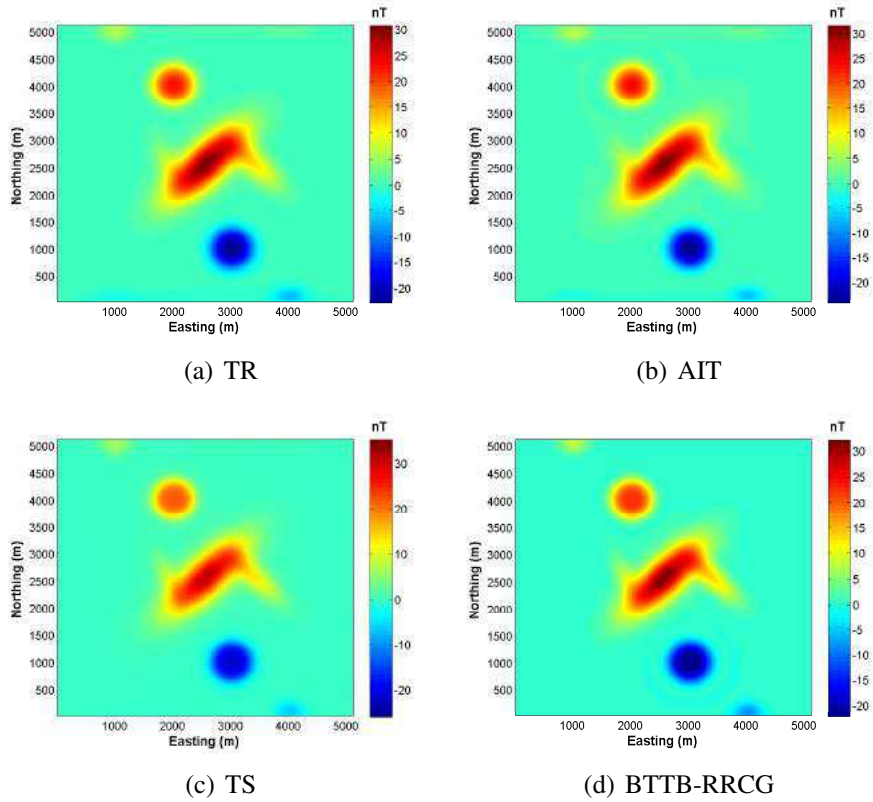


Figure 2.5: The downward continuation with  $\Delta h = 200$  m for the 0.005% noised magnetic field in Figure 2.2(b) by using (a) TR; (b) AIT; (c) TS and (d) BTTB-RRCG method.

The results shown in Figure 2.5 confirm that all four methods produce a stable solution. The error distribution is computed by plotting the difference between the continuation results at  $h = 50$  m in Figure 2.5 and the accurate field at  $h = 50$  m in Figure 2.2(a). The error distribution by the four methods are clearly shown in Figure 2.6.

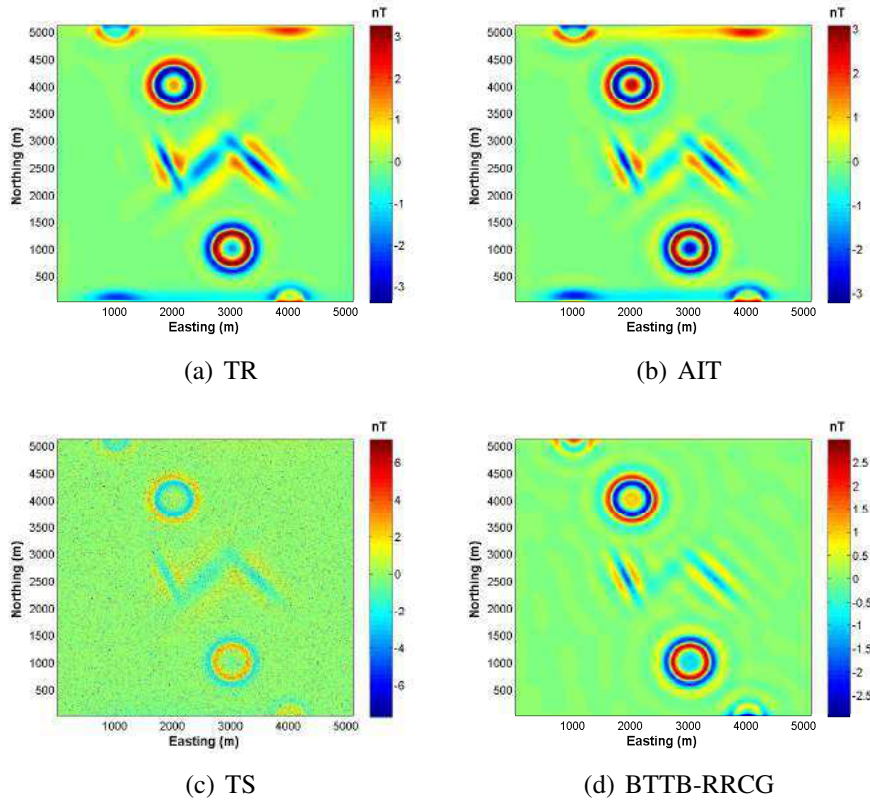


Figure 2.6: The downward continuation error distribution by (a) TR; (b) AIT; (c) TS and (d) BTTB-RRCG method.

To quantify the performance of these methods, we define the  $RMS$ ,  $RE_2$  and  $RE_\infty$  as

$$RMS = \sqrt{\frac{1}{N * M} \sum_{i=1}^N \sum_{j=1}^M (\mathbf{T}_{con} - \mathbf{T}_{real})^2}, \quad (2.3.1)$$

$$RE_2 = \frac{\|\mathbf{T}_{\text{con}} - \mathbf{T}_{\text{real}}\|_2}{\|\mathbf{T}_{\text{real}}\|_2}, \quad (2.3.2)$$

$$RE_\infty = \frac{\|\mathbf{T}_{\text{con}} - \mathbf{T}_{\text{real}}\|_\infty}{\|\mathbf{T}_{\text{real}}\|_\infty}. \quad (2.3.3)$$

Table 2.1 reports the performance of TR, AIT, TS and BTTB-RRCG in terms of  $RMS$ ,  $RE_2$ ,  $RE_\infty$  and the computing time.

Table 2.1: Computational errors using TR, AIT, TS and BTTB-RRCG methods

	TR	AIT	TS	BTTB-RRCG
$RMS$	0.0234	0.0233	0.0202	0.0187
$RE_2$	6.25%	6.17%	4.63%	3.99%
$RE_\infty$	17.00%	16.03%	21.76%	5.74%
Computing time (s)	0.065 s	0.068 s	0.092 s	6.738 s

From Figure 2.6, it can be seen that the edge-effect is clearly evident on the upper and lower boundary by the TR and AIT methods. In contrast, the edge effect is much smaller for the TS and the proposed BTTB-RRCG method. It is interesting to note that the  $RMS$  and  $RE_2$  for the TS are relatively low, however, the  $RE_\infty$  is quite high. From the error distribution illustrated in Figure 2.6(c), the effect due to noise is noticeable. From Figure 2.7(c) and Table 2.1, the BTTB-RRCG method produces good results in terms of  $RMS$ ,  $RE_2$  and  $RE_\infty$ . The BTTB-RRCG method requires more computing time than other methods, since it is an iterative scheme. However, the computing time per iteration is similar with the TR and AIT methods. Note that the numerical complexity of BTTB-RRCG is of order  $n \log n$ , which is same as a FFT base method. It can be easily verify that the error can not be reduced by increasing the field data resolution. Moreover, the edge-

effect is unavoidable by using wavenumber domain methods. For the Taylor series (TS) method without the use of a regularization, the performance is very sensitive to noise. Adding a 1% Gaussian noise to the field data, the  $RMS$ ,  $RE_2$  and  $RE_\infty$  of TS method increase rapidly to 0.2470, 695% and 4200%, respectively. By incorporating a denoising preprocessing, the robustness of TS can be improved. However, the denoising itself usually induces new errors. Therefore, in the following, we only compare the proposed method with regularized TR and AIT methods.

To further investigate the robustness, we increase the Gaussian noise from 1% to 5% in the synthetic field data. The errors of downward continuation solutions by various methods are shown in Table 2.2 and Figure 2.7.

Table 2.2: Error of downward continuation by using TR, AIT and BTTB-RRCG methods with different level of noise

% of noise	$RMS$			$RE_2$			$RE_\infty$		
	TR	AIT	BTTB	TR	AIT	BTTB	TR	AIT	BTTB
0%	0.0234	0.0233	0.0187	6.25%	6.17%	3.99%	16.99%	16.03%	5.74%
1%	0.0235	0.0233	0.0190	6.29%	6.17%	4.12%	17.04%	16.00%	6.38%
2%	0.0235	0.0233	0.0188	6.22%	6.20%	4.02%	17.04%	16.00%	7.16%
3%	0.0236	0.0233	0.0193	6.34%	6.17%	4.26%	17.48%	15.87%	7.86%
4%	0.0239	0.0235	0.0198	6.53%	6.28%	4.46%	18.05%	16.32%	9.61%
5%	0.0244	0.0233	0.0208	6.80%	6.20%	4.95%	18.95%	14.91%	10.71%

From Figure 2.7 and Table 2.2, we conclude that TR, AIT and BTTB-RRCG methods have a robust performance for noisy data, while the BTTB-RRCG method provides the most accurate solution in terms of  $RMS$  and  $RE_2$ . Moreover, the computed solutions by BTTB-RRCG have the smallest  $RE_\infty$  confirming the edge-effect is small compared with other two regularized methods.

Different from the conventional downward continuation methods, the proposed

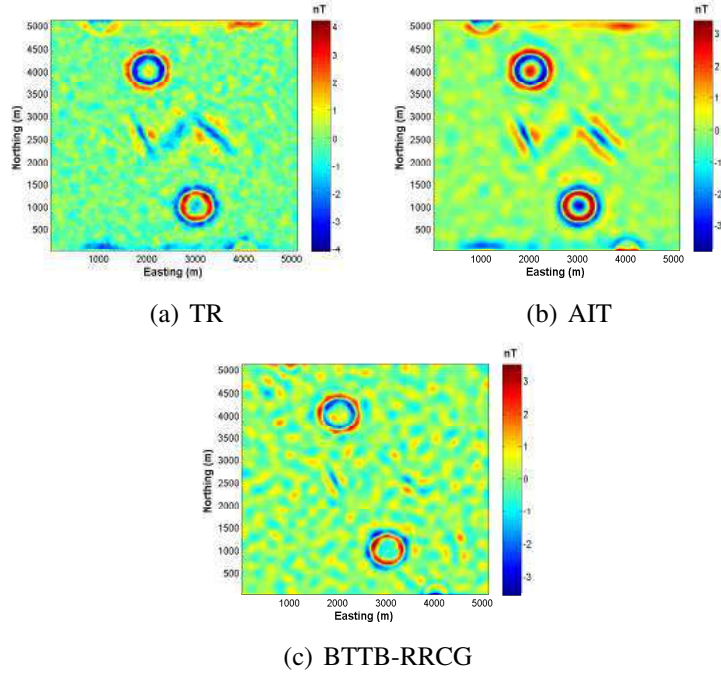


Figure 2.7: The downward continuation error distribution for 5% noised data by (a) TR;(b) AIT; (c) BTTB-RRCG method.

BTTB-RRCG method is an iterative method in space domain, which is seldom investigated due to the computation workload. However, by taking advantage of the BTTB structure makes the CG type methods as effective as wavenumber domain methods. Table 2.3 reports the computing time and storage requirement for various data sizes using the conventional CG method and the BTTB-RRCG method. The resolution of  $M * N$  implies that the field data is given by  $M$  by  $N$  matrix.

Table 2.3: Storage and computing time by conventional and BTTB-RRCG methods

Resolution	Conventional CG method		BTTB-RRCG	
	Storage cost	Time cost	Storage cost	Time cost
128*128	1.47 GB	260 seconds	0.31 MB	0.33 seconds
256*256	23.52 GB	1.16 hours	1.22 MB	1.63 seconds
512*512	376.32 GB	18.6 hours	4.95 MB	6.11 seconds
1024*1024	6000 GB	297 hours	30 MB	24.88 seconds

From Table 2.3, BTTB-RRCG is much more efficient than the conventional CG. Moreover, it is noted that as the size of the problem increases, both the computing cost and storage requirement for the conventional CG increases exponentially. In contrast, the computational complexity for the BTTB-RRCG increases linearly.

The second synthetic test focuses on the density model as shown in Figure 2.8, and the gravity field is generated by the synthetic density model. The density model consists of two dipping prisms underground, where the density of the long prism and the short prism are  $1.0\text{g/cm}^3$  and  $0.8\text{g/cm}^3$ . The depth from the ground to the top of the density anomaly is 100 m. The density anomalies are used to generate a gravity field at  $h = -50$  m and  $h = 200$  m as illustrated in Figure 2.9(a) and 2.9(b) respectively, where the grid interval is  $\Delta x = \Delta y = 20$  m. Denote the gravity field at  $h = -50$  m and  $h = 200$  m by  $\mathbf{T}_{-50}$  and  $\mathbf{T}_{200}$ , we add 2.5% Gaussian noise to  $\mathbf{T}_{200}$  and then apply the TR, AIT and the proposed BTTB-RRCG to conduct the downward continuation to  $\mathbf{T}_{200}$  with continuation distance  $h = 250$  m to compute the field  $\tilde{\mathbf{T}}_{-50}$ . The downward continuation is conducted to the underground, because within the harmonic source-free region, the downward continuation should be always feasible.

The continuation results are shown in Figure 2.10, and the error distribution is given in Figure 2.11. By comparing  $\tilde{\mathbf{T}}_{-50}$  in Figure 2.10 with  $\mathbf{T}_{-50}$  in Figure 2.9(a), we also report the error in terms of  $RMS$ ,  $RE_\infty$  and  $RE_2$  in Table 2.4.

From the downward continuation results in Table 2.4, the proposed BTTB-

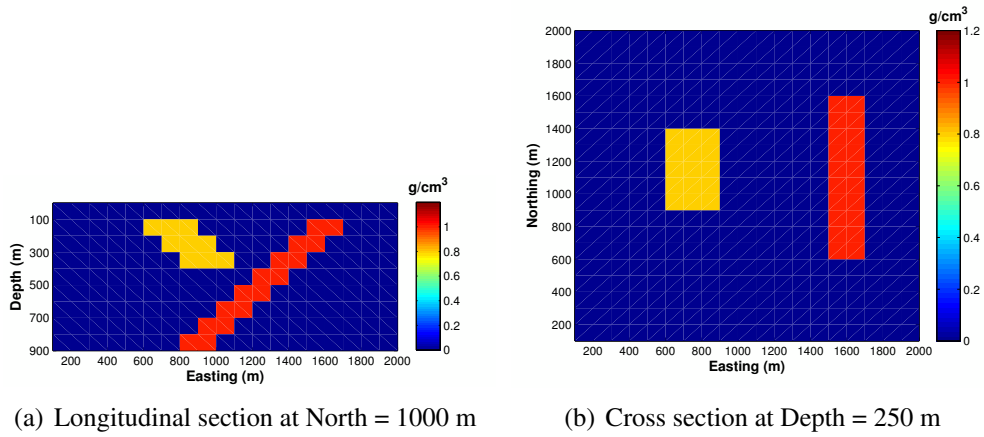


Figure 2.8: Synthetic density model.

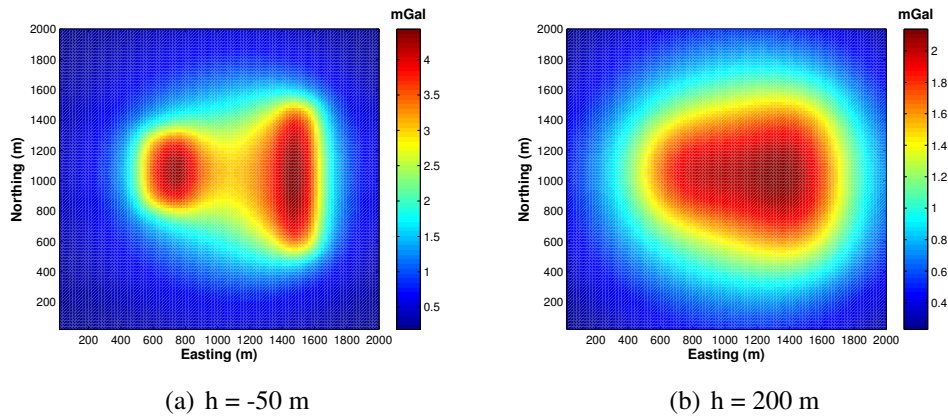


Figure 2.9: Generated field by density model in Figure 2.8.

Table 2.4: Error of downward continuation by using TR, AIT and ITM methods for synthetic gravity data

	TR	AIT	BTTB-RRCG
$RMS$	0.0648	0.0607	0.0430
$RE_{\infty}$	24.17%	23.52%	10.67%
$RE_2$	31.18%	31.58%	19.74%

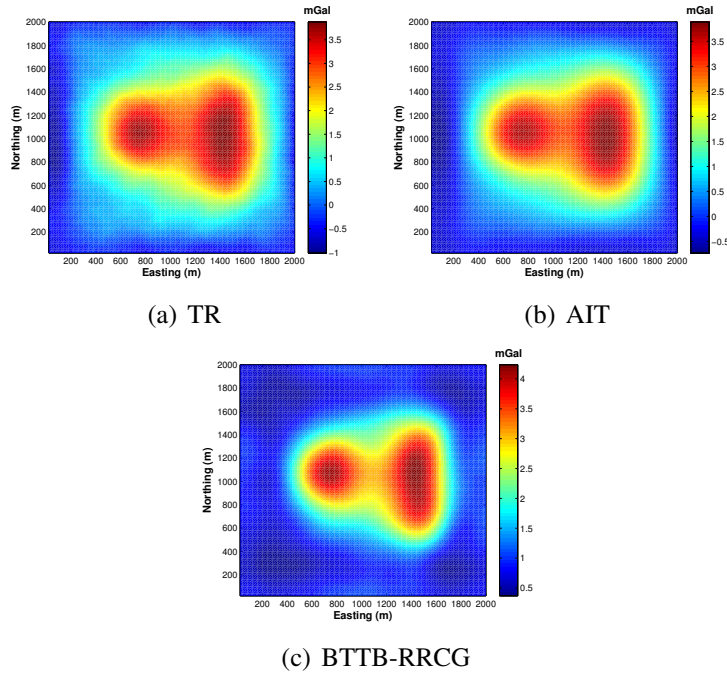


Figure 2.10: The downward continuation results by (a) TR;(b) AIT; (c) BTTB-RRCG method.

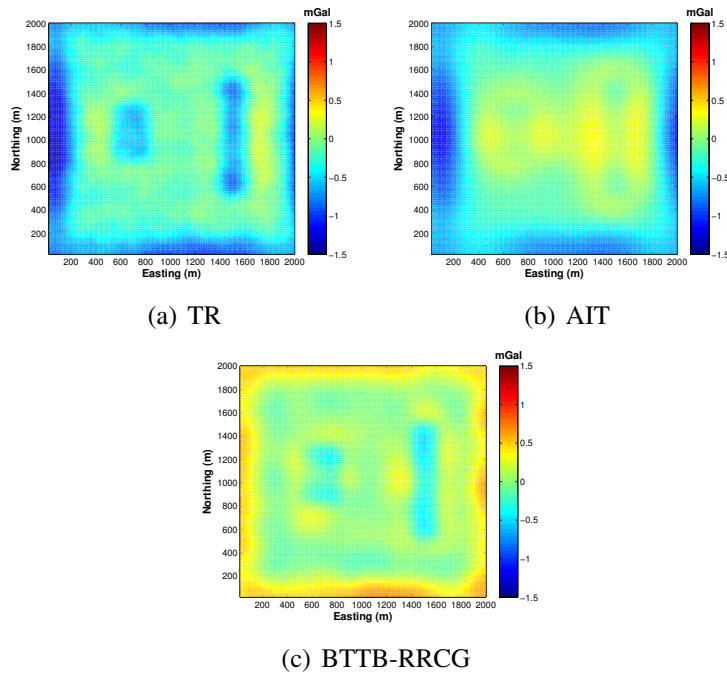


Figure 2.11: The downward continuation error distribution for by (a) TR;(b) AIT; (c) BTTB-RRCG method.

RRCG method is clearly more accurate than the TR and AIT method in terms of  $RMS$ ,  $RE_\infty$  and  $RE_2$ . More importantly, consider that for the density model in Figure 2.10, all anomalies are positive which means generated gravity fields should be positive. However, in Figure 2.10, both TR and AIT methods induce negative values on the left side. However, the proposed BTTB-RRCG scheme perfectly preserve the positivity property, and has a much smaller boundary effect than other two methods.

## 2.4 Applications using real field data

Now, we apply the proposed BTTB-RRCG scheme using real field data<sup>1</sup>. The field data shown in Figure 2.12(a) is the magnetic field distribution at the ground level, where the data grid size are  $\Delta x = \Delta y = 10$  m. The upward continuation of the field data to  $h = 200$  m is shown in Figure 2.12(b),

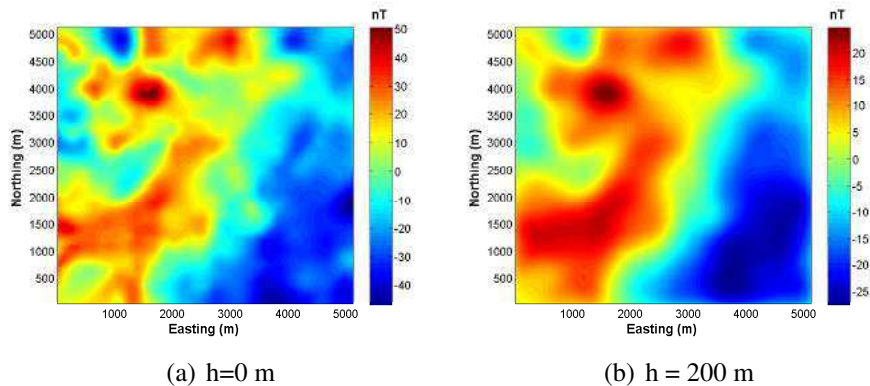


Figure 2.12: (a) The real magnetic field data at  $h = 0$  m;(b) The upward continuation by  $\Delta = 200$  m of the field data in Figure 2.12(a)

<sup>1</sup>The field data used in this thesis is provided by TerraNotes Ltd

By adding 2.5% Gaussian noise to the potential field in Figure 2.12(b), the TR, AIT and BTTB-RRCG methods are used for a downward computation with a continuation distance  $h = 200$  m. The same regularization parameter for the synthetic data is used for the real field data applications. In real applications, the exact downward continuation results are always unknown, therefore we can only have an estimation of the value for the optimal regularization parameters. In our study, we use the optimal regularization parameters obtained in the synthetic case for the real field data. Recall that in a downward continuation formulation (2.1.10), the upward continuation operator  $\mathbf{A}$  depends only on the  $\Delta x$ ,  $\Delta y$ , and  $h$ . Once these parameters are fixed, the spectral characteristic of the continuation operator is determined. In the first synthetic case,  $\Delta x = \Delta y = 9.98m$ , and  $h = 200m$ , while in the real field data,  $\Delta x = \Delta y = 10m$ , and  $h = 200m$ , which means that the spectral characteristic of the continuation operators are similar between the first synthetic case and real field case.

The downward continuation results for the real field data are shown in Figure 2.13, and their error distributions are illustrated in Figure 2.14.

From Figure 2.14(a) and 2.14(b), we observe that the edge-effect is evident near the boundary for the TR and AIT methods. A simple procedure to improve the computed solution is to remove a layer near the boundary. Figures 2.15 and 2.16 illustrate the solutions by tailoring 40 grids (i.e., 400 m) from the edge for the solutions shown in Figure 2.13 and 2.14. It is important to note that the solution

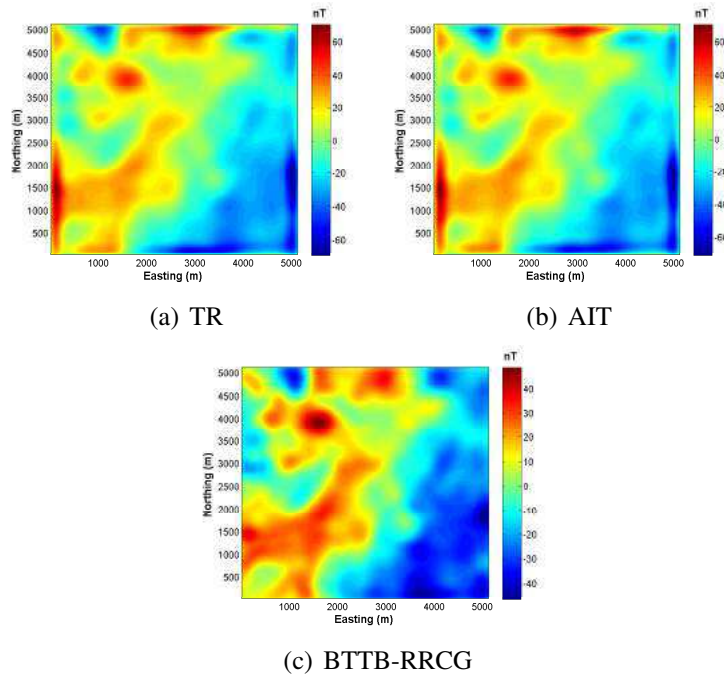


Figure 2.13: The downward continuation by  $\Delta h = 200$  m for 2.5% noised real field data by (a) TR;(b) AIT; (c) BTTB-RRCG method.

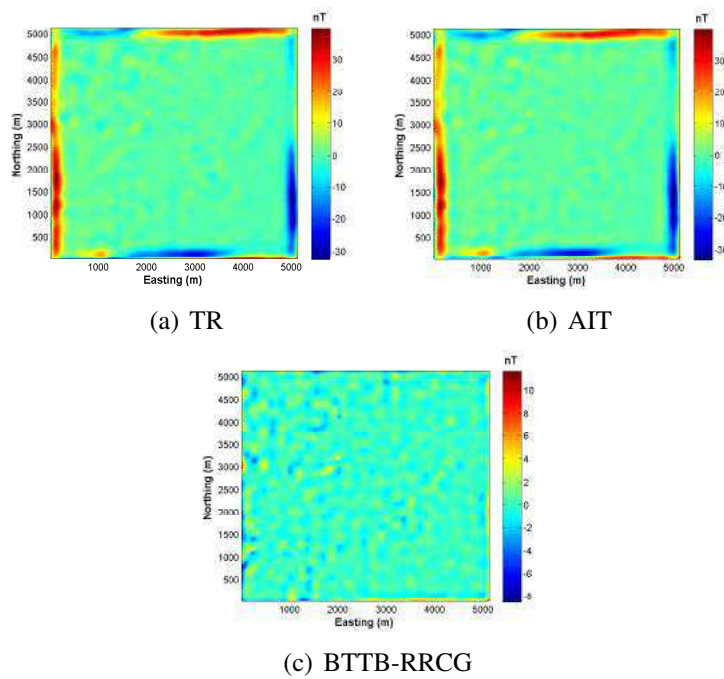


Figure 2.14: The downward continuation error distribution for 2.5% noised real field data by (a) TR;(b) AIT; (c) BTTB-RRCG method.

computed by the BTTB-RRCG method is very stable and with little edge effect. The BTTB-RRCG scheme is an accurate scheme even without the use of any extrapolating and tailoring process.

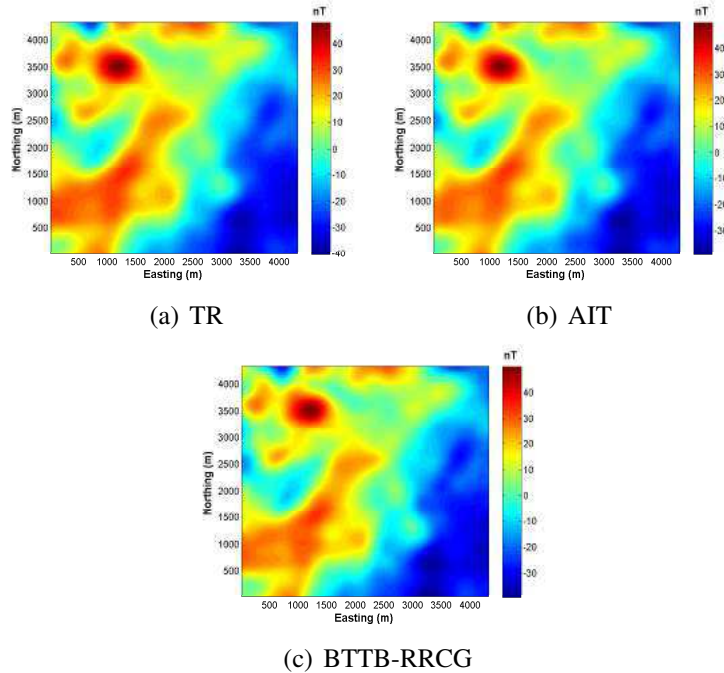


Figure 2.15: The downward continuation by  $\Delta h = 200$  m after tailoring for 2.5% noised real field data by (a) TR;(b) AIT; (c) BTTB-RRCG method.

From the tailored computed solutions for downward continuation shown in Figures 2.15 and 2.16, it is clear that the BTTB-RRCG method is robust and accurate for the real field data compared with TR and AIT methods. By evaluating downward continuation results by TR, AIT and BTTB-RRCG methods in terms of *RMS*, Table 2.5 reports the errors in terms of  $L_2$  and  $L_\infty$  norm. Figure 2.17 displays the convergence rate of the BTTB-RRCG using real field data. It is noted that the residue reaches a steady state after 15 iterations, hence the iteration can be

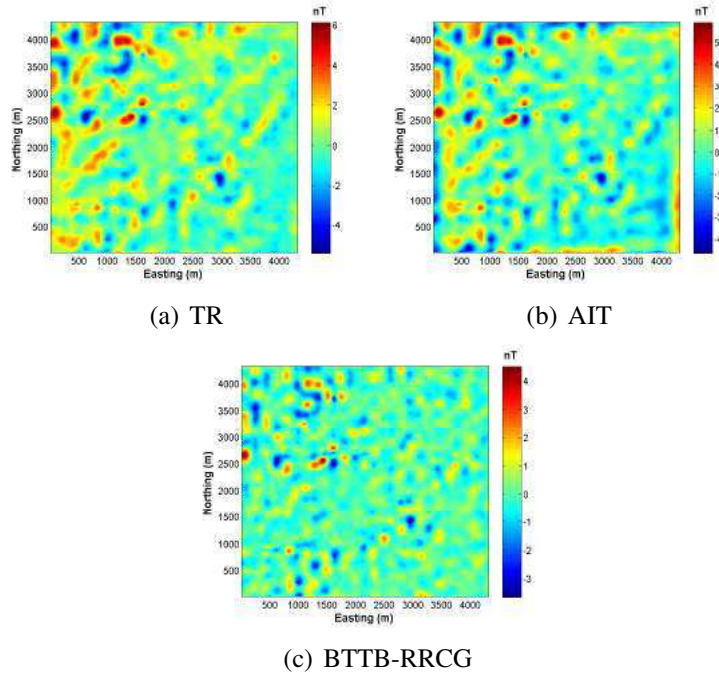


Figure 2.16: The downward continuation error distribution after tailoring for 2.5% noised real field data by (a) TR;(b) AIT; (c) BTTB-RRCG method.

terminated much earlier than the prescribed 35 iterations.

Table 2.5: Error by TR, AIT and BTTB-RRCG methods for real field data

	TR	AIT	BTTB-RRCG
$RMS$	0.0348	0.0357	0.0240
$RE_2$	3.39%	3.55%	1.61%
$RE_\infty$	6.02%	6.52%	3.37%

The robustness and accuracy of the proposed BTTB-RRCG method are verified by the simulation results based on test cases using synthetic and field data. The CG type method is a popular iterative technique for solving large scale linear equations, and it is particularly efficient for large sparse matrices. The main computational work per iteration is typically depended on the matrix-vector product operation. In the present applications, the matrix  $\mathbf{A}$  is a full matrix, and without taking advantage

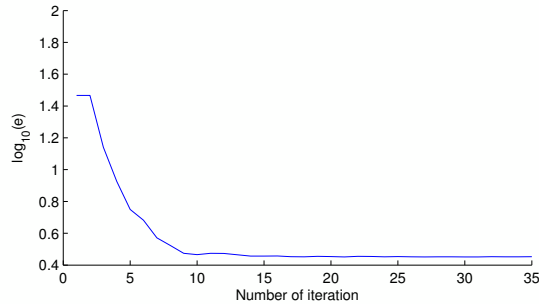


Figure 2.17: Convergence rate of BTTB-RRCG method in the real field data application, where  $\mathbf{e} = \|\mathbf{A}\mathbf{T}_h - \mathbf{T}_0\|_2$ .

of BTTB structure, it requires considerable computing resources. We compare the computational complexity using the conventional RRCG method and the BTTB-RRCG method. The results speak for itself. It is clear that the utilizing the BTTB-structure dramatically reduces both the storage and computing cost, and a large scale downward continuation problem can be computed with a modest computing resource.

## 2.5 Conclusion

In this chapter, we propose efficient approach by utilizing the BTTB structure with the re-weighted regularized conjugate gradient method. Not only the BTTB structure greatly enhance the stability and robustness of the downward continuation computation, but the computation workload and storage requirement are also significantly reduced. We demonstrate that compared with the conventional wavenumber domain FFT-based methods, the BTTB-RRCG scheme induce negligible artifact near the boundary. The simulation results using the clean and highly perturbed

synthetic field data as well as the real field data verify that the proposed method are more accurate and robust compared to the Taylor-series and wavenumber domain regularized methods.

It is also easier to implement various regularization stabilizers directly in time domain instead of wavenumber domain. By plotting the residue at each iteration, we can quickly estimate the number of iterations required for the BTTB-RRCG method. The BTTB structure allows the design of an optimal preconditioner to further accelerate the convergence rate, in which the preconditioner is also in the form of BTTB matrix.

The work presented in this chapter has been published in Journal of Applied Geophysics [121].

## Chapter 3

# Numerical Inversion for Magnetization

Magnetic field survey is a popular tool for fast mapping of large areas in geophysical and environmental study. A typical survey consists of mapping one or more components of the earth geomagnetic field in order to analyze the magnetic anomalies. The magnetic anomalies mapping is generally used in many geological applications such as estimating the basement topography, assessing the depth in oil exploration and the magnetic polarization in mineral prospecting.

Recall that for the potential field inversion problem, the model can be expressed mathematically as an integral formulation, which can be converted into linear equations  $\mathbf{A}\mathbf{u} = \mathbf{b}$ , where  $\mathbf{b}$  is the observation magnetic field data, and the matrix  $\mathbf{A}$  is often large, dense and ill-conditioned [29].

Instead of using a 3D potential field inversion [64, 82], 2-D model is more preferred in many cases, and this is particularly true for the aero-magnetic survey. The simplicity of a 2-D model also makes the 2-D inversion practical and efficient. The inversion for tabular magnetic anomalies or thin layer magnetic anomalies have been investigated in [40, 87, 6, 88, 111].

For an irregular raw data, it can be rewritten into a uniform data conveniently by

the use of a regridding procedure. Many efficient methods have been developed, for instance, Briggs [10] proposed a minimum curvature method for regrid non-uniform data. Cordell and Blakely [25, 9] presented an equivalent layer method (ELM), in which a fictitious source layer is introduced, and then the non-uniform data points are interpolated on a uniform grid according to the source layer. The advantage of implementing the ELM has been reported by Cooper [23], and a comparative study of ELM and the minimum curvature method can be found in [70].

Once the field data are gridded regularly, the linear system of a magnetic inversion problem leads to a symmetric Block-Toeplitz Toeplitz-Block (BTTB) matrix, which has a similar form as the downward continuation problem discussed in Chapter 2. Actually, in the study of interpolating the potential field data, the BTTB structure has already been noticed. Rauth and Strohmer [89] investigated the potential field gridding problem by interpolating the non-uniform field data into a uniform field data, where a trigonometric polynomial is used to approximate the magnetic field, and the coefficients of the polynomial are computed by solving a BTTB system.

In this chapter, we investigate fast magnetic field inversion scheme. Particular attention is focused on incorporating the BTTB structure to develop efficient numerical inversion algorithms based on the multigrid (MG) technique. A comparative study of the MG and conjugate gradient type methods is presented, and the performance of these methods is validated by numerical simulations applied to

the synthetic field data and the real geophysical data. We show that the BTTB-MG technique is robust, accurate, and compared with regularized methods, it provides more information.

### 3.1 Magnetic Field Forward Model

Assuming that the magnetic data covers an area which is filled with a set of vertical prisms with arbitrary horizontal section and the bottom at infinity, the magnetic anomaly reduced to the pole is given by a layer of poles on the top of each prism as shown in Figure 3.1.

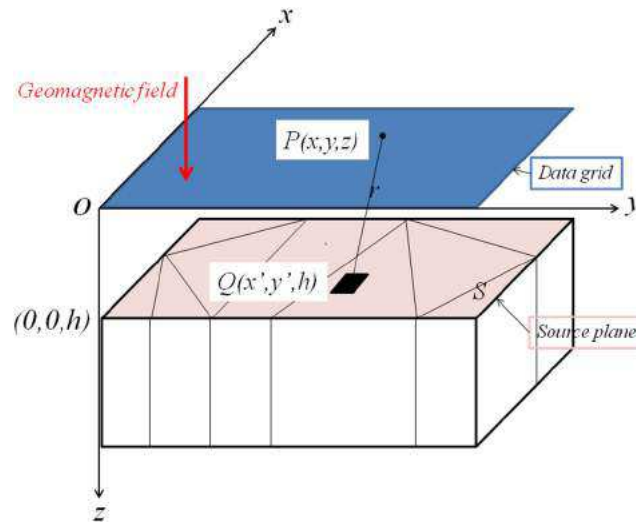


Figure 3.1: Forward Model.

The magnetization is defined as the magnetic moment ( $\mathbf{M}$ ) per volume given by

$$\mathbf{J} = \frac{d\mathbf{M}}{dv}, \quad (3.1.1)$$

which is induced by the earth magnetic field, and it is the source of the magnetic

anomaly. To determine the magnetic field generated by magnetization, the concept of magnetic scalar potential  $\psi$  is introduced. When there is no free current, the magnetic scalar potential can be used to determine the magnetic H-field especially for the permanent magnets in the following way:

$$\mathbf{H} = -\nabla\psi. \quad (3.1.2)$$

It is known that the magnetic potential generated by  $d\mathbf{M}$  at an arbitrary point  $P$  is defined by  $d\psi = \frac{d\mathbf{M}\cdot\mathbf{r}}{\rho}$ , where  $\mathbf{r}$  is a coordinate of  $P$ , and  $\rho$  is the distance from  $P$  to  $dv$ . According to (3.1.1),

$$d\psi = - \left[ \mathbf{J} \cdot \nabla \left( \frac{1}{\rho} \right) \right] dv. \quad (3.1.3)$$

Thus, the magnetic potential at the point  $P$  generated by a prism is given by

$$\psi = - \int_V \left[ \mathbf{J} \cdot \nabla \left( \frac{1}{\rho} \right) \right] dv. \quad (3.1.4)$$

According to the Gauss formula, (3.1.4) can be further rewritten as

$$\psi = \int_S \frac{(\mathbf{J} \cdot d\mathbf{S})}{\rho} - \int_V \left( \frac{\text{div}\mathbf{J}}{\rho} \right) dv. \quad (3.1.5)$$

where  $V$  is the volume of magnetization, and  $S$  is the surface area of the magnetization. By assuming that in each prism, the value of magnetization  $\mathbf{J}$  is uniform, and the magnetization in the prisms have the same direction, then  $\text{div}\mathbf{J} = 0$ , and only the first term in (3.1.5) is retained. The integral on the side facing the prisms can be neglected, since the bottom is assumed to be infinitely deep and the upper

surface can be regarded as the source plane. Hence, (3.1.5) can be simplified as

$$\psi = \int_S \frac{J_n}{\rho} dS, \quad (3.1.6)$$

where  $J_n$  is the vertical magnetization in the  $n$ th prism. Here, the magnetic potential  $\psi$  is a function of the coordinate point  $P$ . If we denote the position of  $dv$  as  $Q$ , and the coordinate  $Q$  as  $\mathbf{r}'$ , then  $\rho = |\mathbf{r} - \mathbf{r}'|$ . According to (3.1.2), the magnetic field generated by each prism is given by

$$\mathbf{H} = -\nabla\psi = -\nabla \int_S \frac{J_n}{|\mathbf{r} - \mathbf{r}'|} dS, \quad (3.1.7)$$

in which the vertical magnetic field is

$$H_z = \int_S \frac{J_n(z - z')}{|\mathbf{r} - \mathbf{r}'|^3} dS. \quad (3.1.8)$$

Now, consider all prisms as a whole, thus the magnetic field at the point  $P$  is generated by all prisms. By (3.1.8), denote the  $J_n$  as a function of coordinate, then the magnetic anomaly is described by the convolution of two functions: the kernel depending on the positions of the observations and the other describing the distribution of magnetization as the following:

$$H_z(x, y, z) = \iint_S m(x', y', z') G(x, y, z, x', y', z') dx' dy', \quad (3.1.9)$$

where

$$G(x, y, z, x', y', z') = \frac{z - z'}{[(x - x')^2 + (y - y')^2 + (z - z')^2]^{\frac{3}{2}}}. \quad (3.1.10)$$

It is interesting to note that the kernel in (3.1.10) has exactly the same format as that in Chapter 2 of a downward continuation formulation. Similarly, the forward model of a magnetic field problem can be written as

$$\mathbf{b} = \mathbf{A}\mathbf{u}, \quad (3.1.11)$$

where  $\mathbf{b}$  is the observed magnetic field,  $\mathbf{u}$  is the magnetization distribution, and  $\mathbf{A}$  is the magnetic forward operator.

### 3.1.1 Multigrid techniques

It is well-known that the convergence of CG type methods depends on the condition number of the matrix  $\mathbf{A}$ . In a magnetic inversion problem, the system matrix in (3.1.11) is usually very ill-conditioned and with a large condition number. Multigrid (MG) technique is developed based on multilevel iterative methods, and it has generally been regarded that MG is an optimal iterative method for solving large positive definite systems resulting from elliptic partial differential equations. The technique is optimal since the convergence rate is independent of the condition number of  $\mathbf{A}$  and the size of the linear system.

When solving a linear system by a classical relaxation scheme based on the Jacobi or Gauss-Seidel method, we note that the high frequency error can be eliminated very quickly, but it is hard to remove the low frequency error. Consequently, a rapid error reduction is typically observed at the initial stage, and after that the

error decreases very slowly leading to a slow convergence rate.

Suppose we want to solve a linear system (3.1.11), instead of applying an iterative scheme directly, we now consider the solution being computed by applying a relaxation scheme to multilevel or multigrid systems

$$\mathbf{A}^j \mathbf{u}^j = \mathbf{b}^j, \quad (3.1.12)$$

where  $\mathbf{A}^j$  denotes the matrix at different grid levels with  $\mathbf{A}^1 = \mathbf{A}$  known as the finest grid, and the matrices  $\mathbf{A}^j$ ,  $j = 2, 3, \dots$  are referred as the coarse grid levels,  $\mathbf{b}^j$  and  $\mathbf{u}^j$  are the observed field and inverted solution in each level. The coefficient matrix  $\mathbf{A}^j$  for  $j > 1$  can be constructed using the same way as for  $\mathbf{A}^1$  but with a coarser mesh. The superior performance of a MG method is achieved due to the fact that the low frequency error on the fine grid can be regarded as the high frequency error on the coarse grid. Thus by employing a relaxation scheme to a sequence of various grid levels, the high and low frequency error components can be eliminated rapidly and this ensures a fast convergence rate for a MG method.

The idea of a MG approach can be easily explained by a two-grid method as illustrated in Figure 3.2.

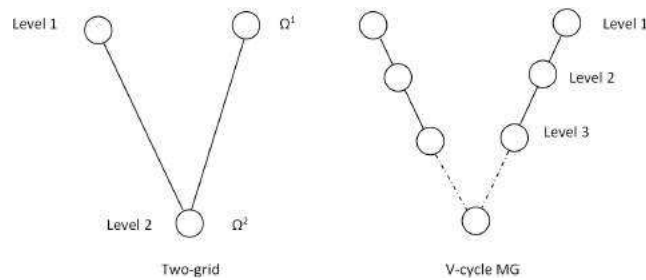


Figure 3.2: Two-grid and V-cycle MG.

Recall that if  $\bar{\mathbf{u}}$  is the computed solution of  $\mathbf{A}\mathbf{u} = \mathbf{b}$ , the residual is defined by

$$\mathbf{r} = \mathbf{b} - \mathbf{A}\bar{\mathbf{u}} = \mathbf{A}(\mathbf{u} - \bar{\mathbf{u}}) = \mathbf{A}\mathbf{e}, \quad (3.1.13)$$

where  $\mathbf{e}$  is the error vector. By solving  $\mathbf{A}\mathbf{e} = \mathbf{r}$ , we can then improve the numerical solution, such that

$$\mathbf{u} = \bar{\mathbf{u}} + \mathbf{e}. \quad (3.1.14)$$

Let  $\Omega^1$  and  $\Omega^2$  denote the fine grid (i.e. level 1) and the coarse grid (i.e. level 2). In a two-grid method, starting with an initial approximation  $\mathbf{u}^0$ , the algorithm is given as

- (i) Smoothing step: In  $\Omega^1$ , apply relaxation (3.1.15)  $v_1$  time,  $\mathbf{u}^1 \rightarrow S(\mathbf{u}^1, \mathbf{b}^1)$ ,
- (ii) Compute the residual and transfer from  $\Omega^1$  to  $\Omega^2$ :

$$\mathbf{r}^1 = \mathbf{b}^1 - \mathbf{A}^1\mathbf{u}^1, \quad \mathbf{r}^2 = \mathbf{R}_1^2\mathbf{r}^1,$$

- (iii) In  $\Omega^2$ , solve the error equation:  $\mathbf{A}^2\mathbf{e}^2 = \mathbf{r}^2$ ,
- (iv) Interpolate error from  $\Omega^2$  to  $\Omega^1$  and improve the approximation:  $\mathbf{u}^1 \rightarrow \mathbf{u}^1 + \mathbf{I}_2^1\mathbf{e}^2$ ,
- (v) Correction step: Apply relaxation again  $v_2$  time,  $\mathbf{u}^1 \rightarrow S(\mathbf{u}^1, \mathbf{b}^1)$ ,
- (vi) Repeat the procedure until a stopping criteria such as  $\|\mathbf{r}^1\| < \varepsilon$  is achieved.

Here,  $S(\mathbf{u}^1, \mathbf{b}^1)$  denotes a smoothing or a relaxation process which will be defined shortly. Dropping the superscript index for the matrix  $\mathbf{A}$ , let  $\mathbf{A} = \mathbf{D} - \mathbf{L} - \mathbf{L}^T$ ,

where  $\mathbf{L}$  is the lower triangular of matrix  $\mathbf{A}$ ,  $\mathbf{u}^0$  is an initial approximation, the weighted Jacobi relaxation is selected as a smoothing operator such that  $S(\mathbf{u}^1, \mathbf{b}^1)$  is defined by

$$\mathbf{u}^1 = [(1 - \omega)\mathbf{I} + \omega\mathbf{D}^{-1}(\mathbf{L} + \mathbf{L}^T)]\mathbf{u}^0 + \omega\mathbf{D}^{-1}\mathbf{b}^1, \quad (3.1.15)$$

where  $\omega$  is a parameter, which can be estimated by a formula proposed in [100]:

$$\omega \leq \frac{a_{0,0}}{\rho(\mathbf{A})}, \quad (3.1.16)$$

where  $a_{0,0}$  is the first element of the matrix  $\mathbf{A}$  and  $\rho(\mathbf{A})$  is the spectral radius of  $\mathbf{A}$ . Note that  $\mathbf{R}_1^2$  is a restriction operator which is used to transfer the residual from a fine grid denoted as grid 1 to coarse grid denoted as grid 2, and  $\mathbf{I}_2^1$  is an interpolation operator which is used to interpolate the error from a coarse grid to a fine grid. Also, (i) is generally referred as the smoothing step, and (iii) is the correction step in an MG cycle.

The most important advantage of using BTTB structure in the multi-grid method is that, in step (iii), the system matrix of at coarser level always keep the BTTB structure as the original system. This means that in each level, we are able to apply the efficient FFT to accelerate the computation. By repeatedly applying a two-grid method, we can construct an efficient multigrid method, and the V-cycle MG is shown in Figure 3.2. The details on the construction of the coarse grid coefficient matrices, the restriction and interpolation operators can be found in [11].

## 3.2 Numerical Simulations

To validate the effectiveness of the proposed BTTB-MG scheme, we consider the following test cases. The proposed BTTB-MG method will be assessed and compared with the BTTB-RRCG method based in terms of efficiency, accuracy and robustness. The computation is carried out using a laptop computer with Intel i7-3632QM 2.2 Hz and 12G RAM. For the MG method, the level of grids in the V-cycle will be determined, and  $v_1 = v_2 = 1$  will be used in the smoothing and correction steps.

### 3.2.1 Synthetic data

The first test case is constructed as in Figure 3.3, which illustrates an initial magnetization distribution. The reason we use this synthetic data has been discussed in Chapter 2, and it is considered to be the source generating the magnetic field solution for the magnetic inversion problem. In Figure 3.4, we display the computed magnetic field data generated by the given synthetic magnetization distribution with different depth  $h = 50\text{m}, 100\text{m}, 200\text{m}, 250\text{m}$ , respectively. By applying the magnetic inversion scheme to these synthetic magnetic field data, we can evaluate the performance of the BTTB-MG scheme, and compare it with the proposed BTTB-RRCG scheme. First, let the relative error (RE) be defined as:

$$RE = \frac{\|\mathbf{U}_{\text{inv}} - \mathbf{U}_{\text{exact}}\|_{\infty}}{\|\mathbf{U}_{\text{exact}}\|_{\infty}} \times 100\%, \quad (3.2.1)$$

Table 3.1: Condition number of the coefficient matrix corresponding to different depths.

Depth (m)	Condition Number
50	$1.2410 \cdot 10^8$
100	$5.8372 \cdot 10^8$
200	$2.1781 \cdot 10^9$
250	$3.2852 \cdot 10^9$

where  $\mathbf{U}_{\text{inv}}$  is the computed inverse solution,  $\mathbf{U}_{\text{exact}}$  is the exact solution.

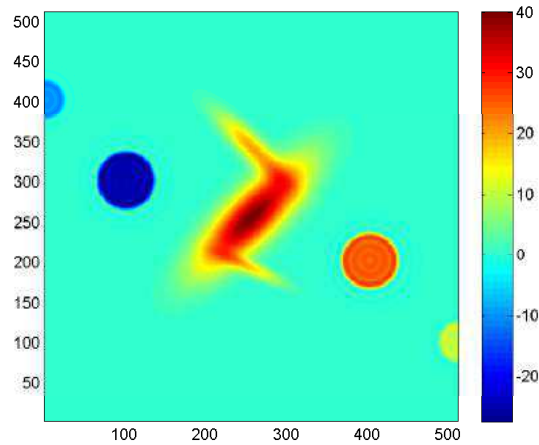


Figure 3.3: Initial magnetization distribution.

In Table 3.1, we list the condition number of the coefficient matrix  $\mathbf{T}$  in (3.1.11) for a range of depths from  $h = 50$  m to 250 m. The condition number increases as the depth is increasing, therefore, within the 250 m depth, that the largest condition number appears at the maximum depth. Hence, the synthetic field data at  $h = 250$  m is chosen as the test case in which the simulation data will be inverted. Instead of using fixed iteration numbers as in Chapter 2, the stopping criterion used in this

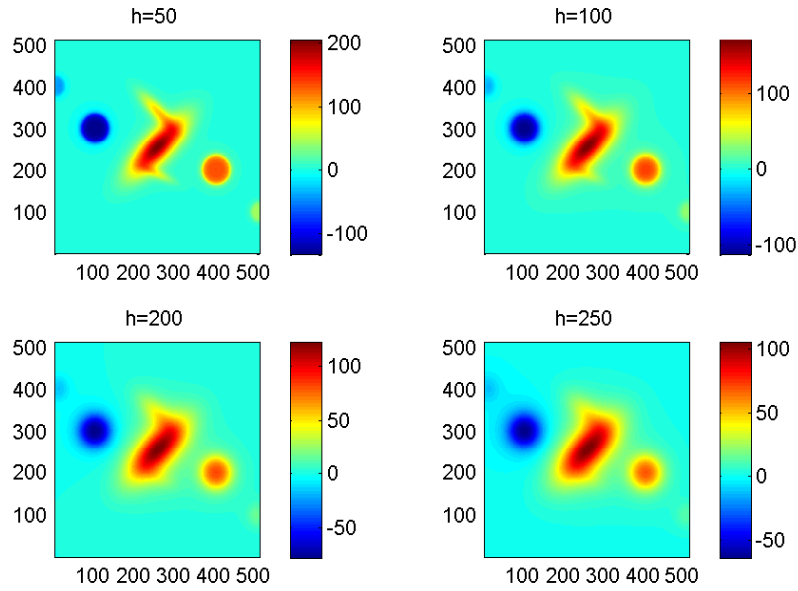


Figure 3.4: Magnetic field data at different depths.

computation is

$$\frac{\|\mathbf{r}_n\|_\infty}{\|\mathbf{r}_0\|_\infty} < tol,$$

where  $tol$  is the tolerance of the iteration,  $\mathbf{r}_n$  is the residue at the  $n$ -step iterations,  $\mathbf{r}_0$  is the initial residue. For the multigrid method, to determine the optimal level of the grid in V-cycle iteration scheme, we report the level of grids vs the computing time and number of cycles in the following Table 3.2.

Table 3.2: Computing time and number of V-cycles of MG with various grid levels.

Level	Tol= $10^{-3}$		Tol= $10^{-4}$	
	$T_{MG}$ (s)	$N$	$T_{MG}$ (s)	$N$
2	7.122357	24	62.540190	203
3	3.575487	11	32.270307	97
4	3.248739	10	33.257580	103
5	3.209048	10	33.601279	103

In Table 3.2, we present the MG results where the level denotes the number of grid levels used in a V-cycle,  $T$  is the computing time in second,  $N$  is the number of cycles to reach a given tolerance. It is clear that a good performance is achieved when the grid level is greater than two. However, for the inversion problem considered here, taking three grid levels in a V-cycle seems to suffice, and a 50% reduction in computing time over a two-grid method is achieved. However, it should be noted that the number of multigrid levels is problem dependent and also depends on the resolution of grids. We use three level grid in the following problem because the field data used in the simulation has very similar resolution with the case we tested above. While for the data with different resolution, more work is needed to find the optimal grid level.

To compare the effectiveness of various numerical inversion schemes, Table 3.3 reports the inversion of the synthetic magnetic field data at  $h = 250$  m by CG, Preconditioned CG (PCG), RRCG and MG methods, where all numerical schemes are taking advantage of the BTTB structure. Particularly, the preconditioner used in the PCG method is constructed according to (4.2.9) in Chapter 4. Here,  $N$  denotes the number of iterations in CG type methods and the number of cycles in MG method, and N/A means that the scheme fails to converge within 2000 iterations. In Figure 3.5, we plot the convergence rate for the CG, PCG, RRCG and MG methods.

From the results presented in Table 3.3 and Figure 3.5, we note that the pre-

Table 3.3: Computing time and iteration numbers of various numerical inversion for synthetic data at  $h=250\text{m}$ .

Tolerance	$T_{CG}$ (s)	$N$	$T_{RRCG}$ (s)	$N$	$T_{PCG}$ (s)	$N$	$T_{MG}$ (s)	$N$
$1 * 10^{-2}$	0.678969	9	9.323636	50	0.547881	7	0.585323	2
$1 * 10^{-3}$	1.330730	19	31.220969	167	1.175903	14	3.219449	11
$1 * 10^{-4}$	3.477457	53	N/A	N/A	2.692719	35	27.853854	97
$1 * 10^{-5}$	11.896358	182	N/A	N/A	7.668079	99	306.236100	1026

conditioned CG (PCG) is the most efficient in term of computing time needed to reach a given accuracy, and it then follows by the CG, MG and RRCG. Although the RRCG method has been a robust method used in many geophysical applications, it has a slow convergence rate and fails to reach a given tolerance within 2000 iterations when a small tolerance is required as indicated in Table 3.3. When the tolerance is in the level of  $1 * 10^{-2}$  or  $1 * 10^{-3}$ , the performance of the CG, PCG and MG are comparable in terms of convergence rate and the computing time required. In Figure 3.6, the computed solutions of the four methods for the inversion problem are displayed.

In Table 3.4, we present the relative errors between the accurate distribution and the inversion solution computed by the CG and MG methods for the test cases using the synthetic data. For a given depth, the relative error can be reduced by setting a smaller tolerance. It is observed that for a fixed tolerance, the error increases as the depth is increasing.

The test cases investigated here are constructed based on synthetic data, and they are essentially noise-free data. However, the accuracy and effectiveness of an inversion algorithm can not be guaranteed if the data is contaminated with noise. In

Table 3.4: Relative error of CG and MG method at different depths and tolerance.

Depth (m)	CG				MG			
	$10^{-2}$	$10^{-3}$	$10^{-4}$	$10^{-5}$	$10^{-2}$	$10^{-3}$	$10^{-4}$	$10^{-5}$
50	6.55%	2.83%	1.30%	0.52%	6.72%	4.32%	2.13%	1.75%
100	11.54%	3.55%	2.33%	0.97%	14.00%	9.77%	5.09%	3.70%
200	21.78%	14.95%	8.62%	6.7%	24.11%	16.47%	10.43%	7.75%
250	24.42%	19.28%	12.97%	6.67%	27.20%	21.25%	15.00%	9.87%

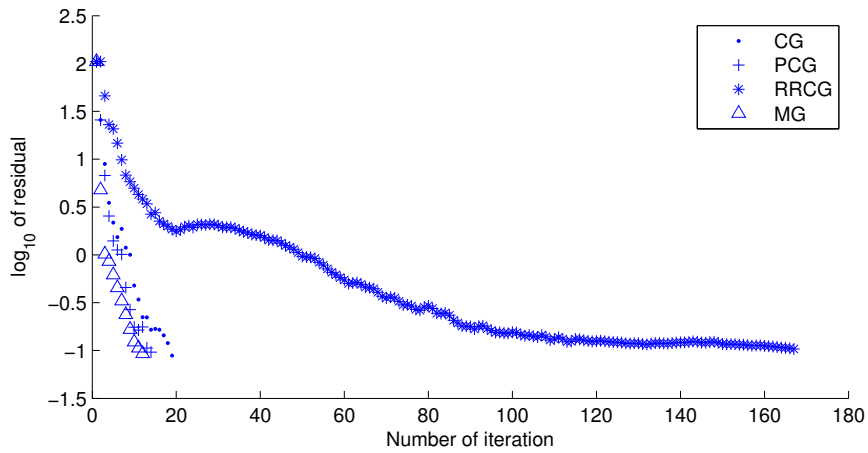


Figure 3.5: Convergence rate of CG, RRCG, PCG and MG method at tolerance= $1 * 10^{-3}$ .

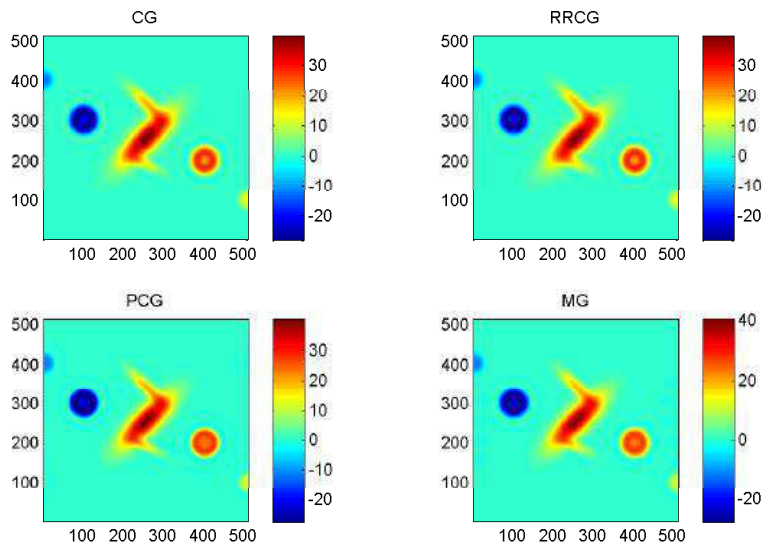


Figure 3.6: Inversion of the magnetic field at  $h=250$  m by CG, RRCG, PCG and MG method.

reality, the magnetic field data obtained by measurement are always contaminated with noise. Thus, it is important to study the robustness of numerical inversion schemes.

Let  $\mathbf{A}$  be the potential field resulted from a synthetic magnetization distribution, and  $\mathbf{E}$  be the matrix with coefficients generated randomly in the range  $[0, 1]$  drawn from the standard normal distribution. Considering the noise in the observation data is caused from the measuring apparatus, the noisy observation data  $\hat{\mathbf{A}}$  with a noise level of  $\alpha\%$  can be defined by  $\hat{\mathbf{A}} = \mathbf{A} + \alpha\% * \mathbf{E}$ .

In Table 3.5 and Figure 3.7, the performance of the CG, PCG, RRCG and MG methods are compared when the observation data with different level of noise are inverted. When the noise level is 0%, the test case converts to the original clean synthetic magnetic field data. It is observed that although the CG and PCG are very effective when applied to clean data, their performances deteriorated rapidly when noise is added in the field data. The RRCG is a very reliable method, and the relative error remains almost at the same level even when a 20% noise is introduced. The MG method is not sensitive when the noise level is less than 10%, but the noise effect becomes noticeable when the noise level is greater than 10%. Unlike the RRCG, a regularization procedure is not incorporated to the MG method. Therefore, the performance could be improved if a suitable regularization is introduced.

From the computational results presented for the synthetic data, it is clear that both CG and PCG methods are sensitive to the noisy data, thus the methods can not

Table 3.5: Relative error of CG, RRCG, PG and MG with different noise levels (%).

	0%	1%	4%	8%	12%	16%	20%
CG	24.42%	24.46%	24.25%	26.13%	$4.8 \cdot 10^4$	$6.7 \cdot 10^4$	$8.0 \cdot 10^4$
RRCG	26.51%	26.51%	26.40%	25.63%	25.34%	25.00%	24.09%
PCG	25.80%	60.36%	$7.2 \cdot 10^6$	$1.4 \cdot 10^7$			
MG	27.20%	27.19%	27.24%	26.60%	27.78%	29.49%	32.90%

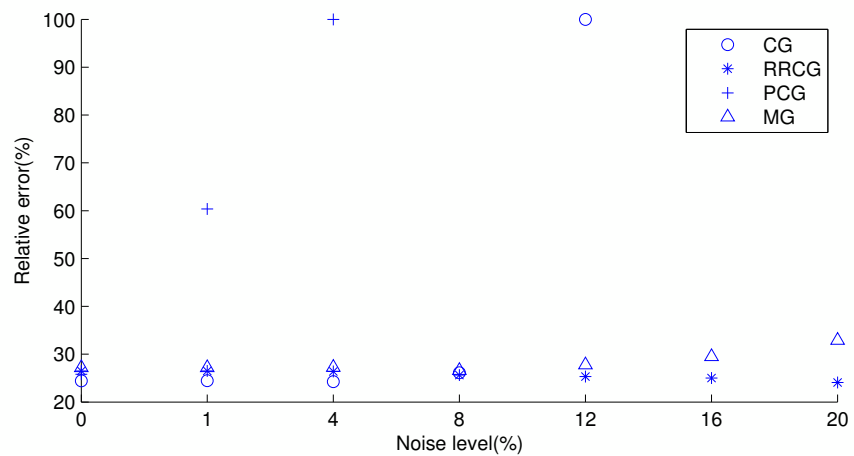


Figure 3.7: Error vs noise level for the CG, RRCG, PCG and MG method under tolerance= $10^{-2}$ .

be used for real field data. The proposed BTTB-MG and BTTB-RRCG methods are more robust than the CG and PCG methods. However, the BTTB-MG method is non-regularized, and is more accurate in term of relative error.

### **3.2.2 Real Data**

Given a real geophysical data, the numerical inversion program provides an estimate of magnetization of underground rocks at certain depth  $h$ . Generally speaking,  $h$  is an unknown, and by producing a sequence of magnetization at various depths, it would provide useful information for the geologists or geophysicists to interpret the computation results and to study how dependent the results are on the variations of  $h$ .

In order to reduce the numerical artifact introduced by the numerical scheme near the boundary, we adjust the results presented in the window shown in Figure 3.8 which is obtained by removing the shadow layer from the original data. Note that the shadow layer has a thickness of only five grid points, and the original data field usually covers several hundred grid points in both directions.

#### **3.2.2.1 Test case I**

For the first test case, the magnetic field data covers a square area with 6000m in both the x- and y- directions, and the interval between each grids is 12m. Thus the resolution of the magnetic field data is 500 by 500 as shown in the Figure 3.9.

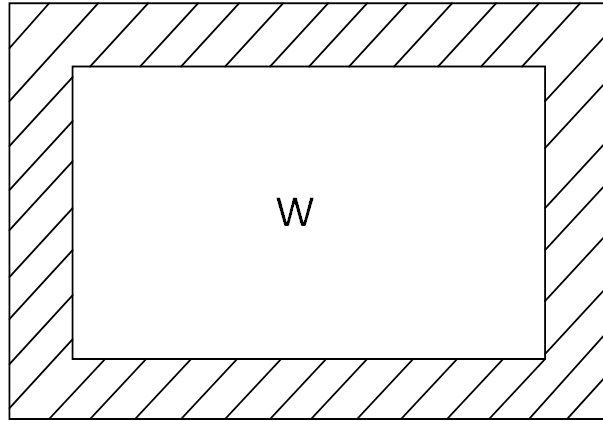


Figure 3.8: Original field data and selected window  $W$ .

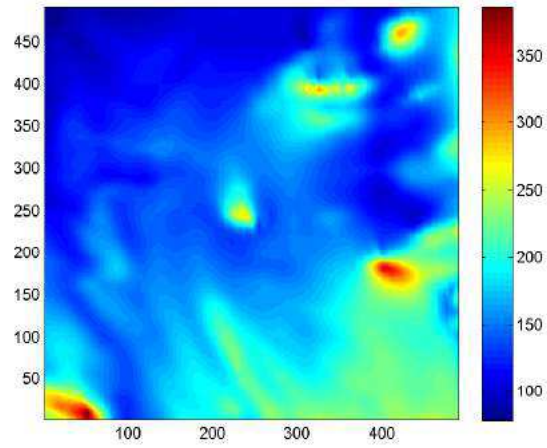


Figure 3.9: Test case I.

Let the tolerance of the inversion program be  $3 * 10^{-1}$ , the computed inversion results at depth  $h = 50$  m, 100 m and 150 m using the RRCG and MG methods are shown in Figure 3.10. Note that the tolerance used here is relatively large, this is because for the real geophysical field data, the schemes can hardly converge with small tolerance. The corresponding computing time are listed in Table 3.6.

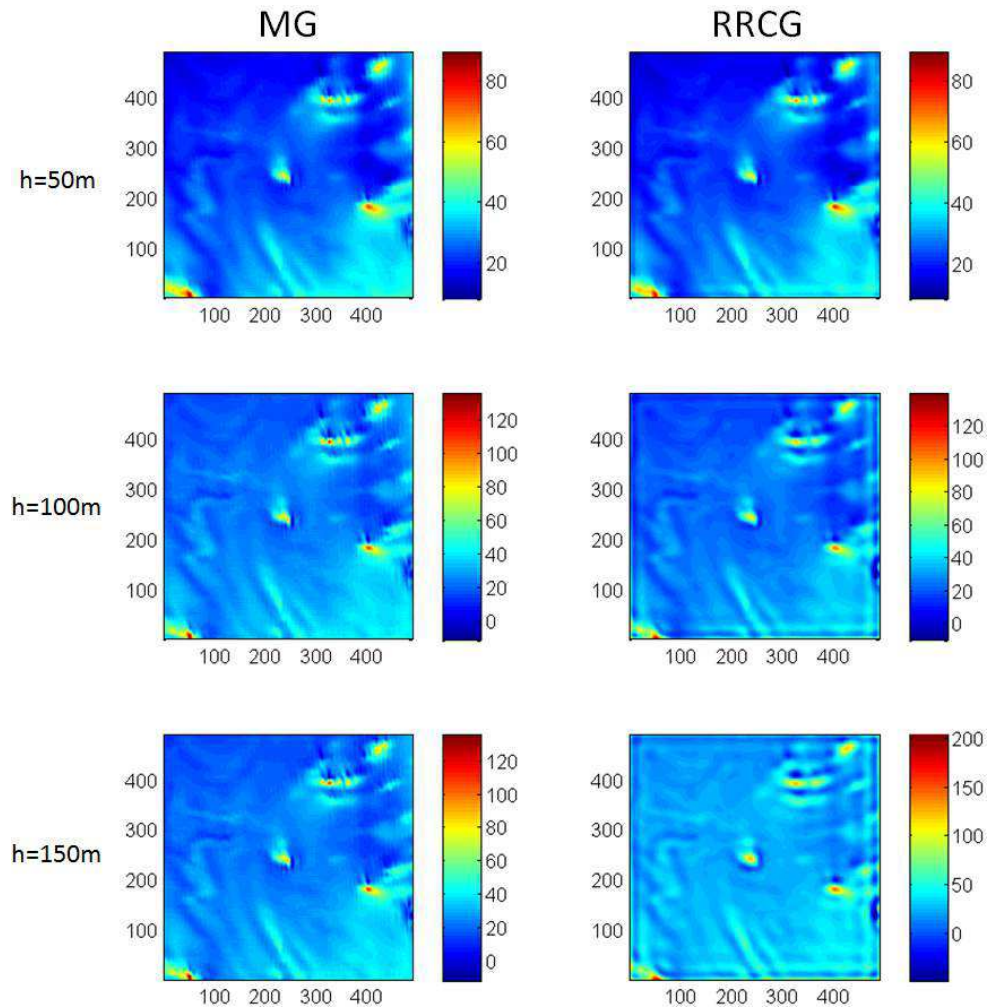


Figure 3.10: Inversion results for test case I with tolerance  $3 * 10^{-1}$

From the results presented in Figure 3.10 and Table 3.6, we observe that the magnetic inversions using the RRCG are in good agreement with those computed

Table 3.6: Computing time for test case I with tolerance  $3 * 10^{-1}$

Depth (m)	$T_{\text{RRCG}}$ (s)	$T_{\text{MG}}$ (s)
50	1.102995	0.466652
100	2.121059	0.964995
150	3.515279	1.404609

by MG. At  $h = 50$  m, the two results are almost identical. However, as  $h$  increases, the RRCG produces noticeable artifacts near the boundary. To investigate the sensitivity of the RRCG and MG methods to the given tolerance, we carry out the simulation with fixed depths, namely  $h=50$  m and  $h=100$  m, and examine the inversion solutions at two values of tolerances. Figure 3.11 and 3.12 present the numerical inversion results, and the corresponding computing time are reported in Table 3.7. As expected, the computed solutions are less sensitive when  $h$  is small as shown in Figure 3.11. Figure 3.12 displays the RRCG and MG results when  $h = 100$  m and the tolerances are set at  $4 * 10^{-1}$  and  $2 * 10^{-1}$ , respectively. Here, the difference between the inversion results corresponding with two tolerances are obvious. Moreover, the artifacts resulting from RRCG at  $\varepsilon = 2 * 10^{-1}$  is also noticeable. From the computing time reported in Tables 3.6 and 3.7, it is clear that MG is more efficient and requires less computing time than the RRCG for all cases tested.

Table 3.7: Computing time for test case I using RRCG and MG

Depth (m)	Tolerance	$T_{\text{RRCG}}$ (s)	$T_{\text{MG}}$ (s)
50	$\varepsilon = 4 * 10^{-1}$	0.894744	0.304539
50	$\varepsilon = 2 * 10^{-1}$	2.557688	0.964625
100	$\varepsilon = 4 * 10^{-1}$	1.576802	0.549794
100	$\varepsilon = 2 * 10^{-1}$	4.114992	2.068582

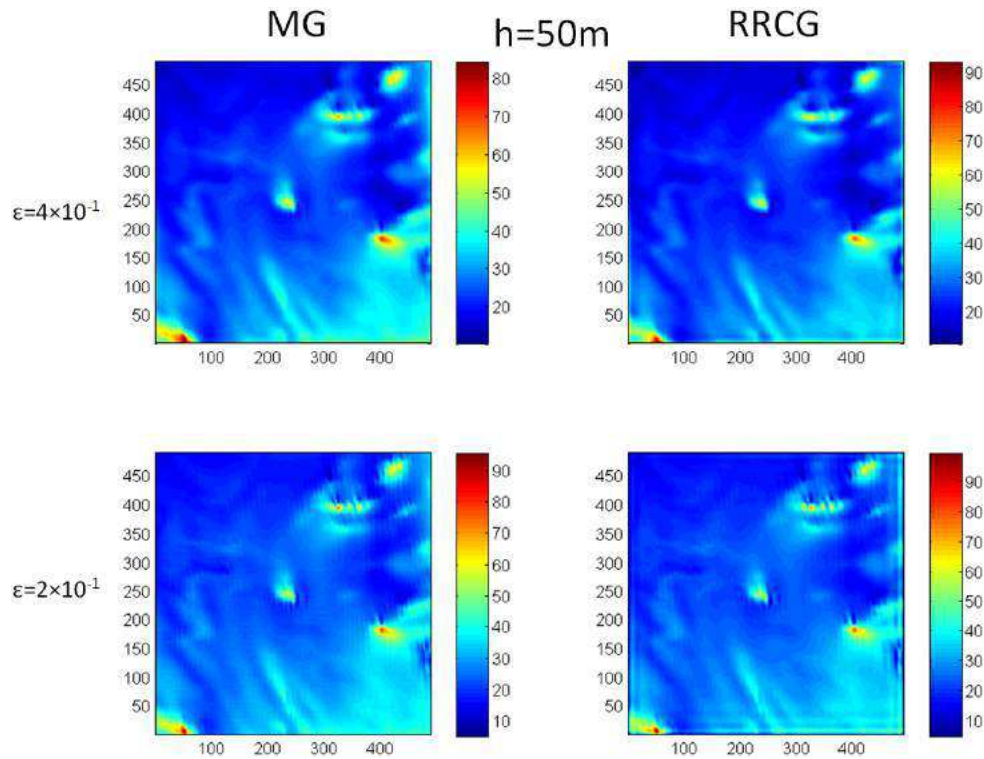


Figure 3.11: Inversion result for test case I at depth  $h=50$  m

### 3.2.2.2 Test case II

In the second test case, the real magnetic field data is given as a rectangle area with length=14040 m, width=8720 m, and the interval between each grids is 20 m. The real magnetic field is defined by a two-dimensional grid of 702 by 436 as shown in Figure 3.13.

To further evaluate the two numerical inversion schemes, Figure 3.14 presents the computed solutions using RRCG and MG methods at a fixed depth  $h=100$ m for tolerance  $1 * 10^{-1}$ ,  $5 * 10^{-2}$  and  $1 * 10^{-2}$ . In Figure 3.15, the inversion results at various depths  $h=50$  m, 100 m and 150 m are illustrated. The computing time

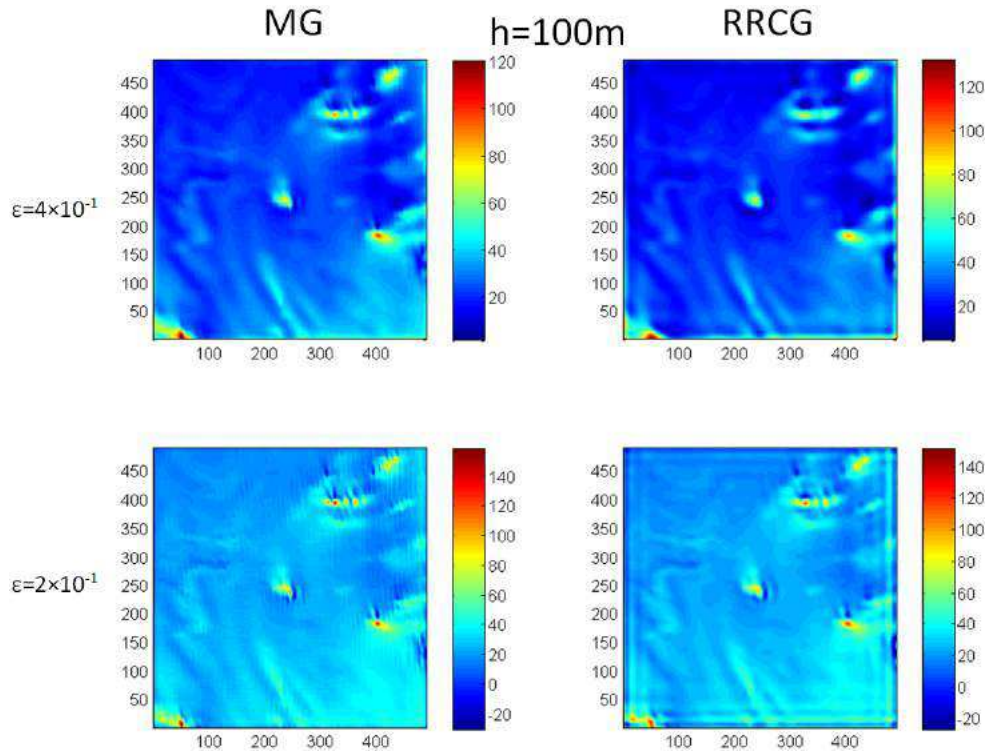


Figure 3.12: Inversion result for test case I at depth  $h=100\text{m}$

required by the two methods are reported in Table 3.8.

From the results applied to test case II, we note that when the depth  $h$  is small, the inversion results produced by RRCG and MG methods are very similar. However, the discrepancy in terms of the maximum and minimum recovered magnetization become noticeable as the depth increases and when the tolerance is decreasing. It is noted that both methods are capable of capturing similar underground geological features, but the RRCG produces larger artifacts near the boundary. The superior performance of the MG method over the RRCG is also clearly demonstrated by the significant saving in computing time as shown in Table 3.8.

Recall that in Chapter 2, we have shown that the BTTB-RRCG method produces

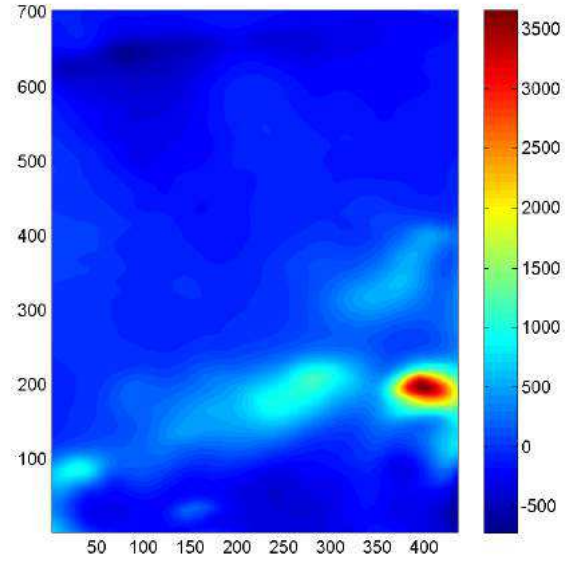


Figure 3.13: Test case II.

Table 3.8: The computing time for test case II.

Depth (m)	Tolerance	$T_{\text{RRCG}}$ (s)	$T_{\text{MG}}$ (s)
100	$\varepsilon = 1 * 10^{-1}$	2.626800	0.700371
100	$\varepsilon = 5 * 10^{-2}$	8.858662	2.744200
100	$\varepsilon = 1 * 10^{-2}$	144.395461	46.382697
50	$\varepsilon = 1 * 10^{-2}$	33.221171	15.612463
200	$\varepsilon = 1 * 10^{-2}$	352.861550	75.893122

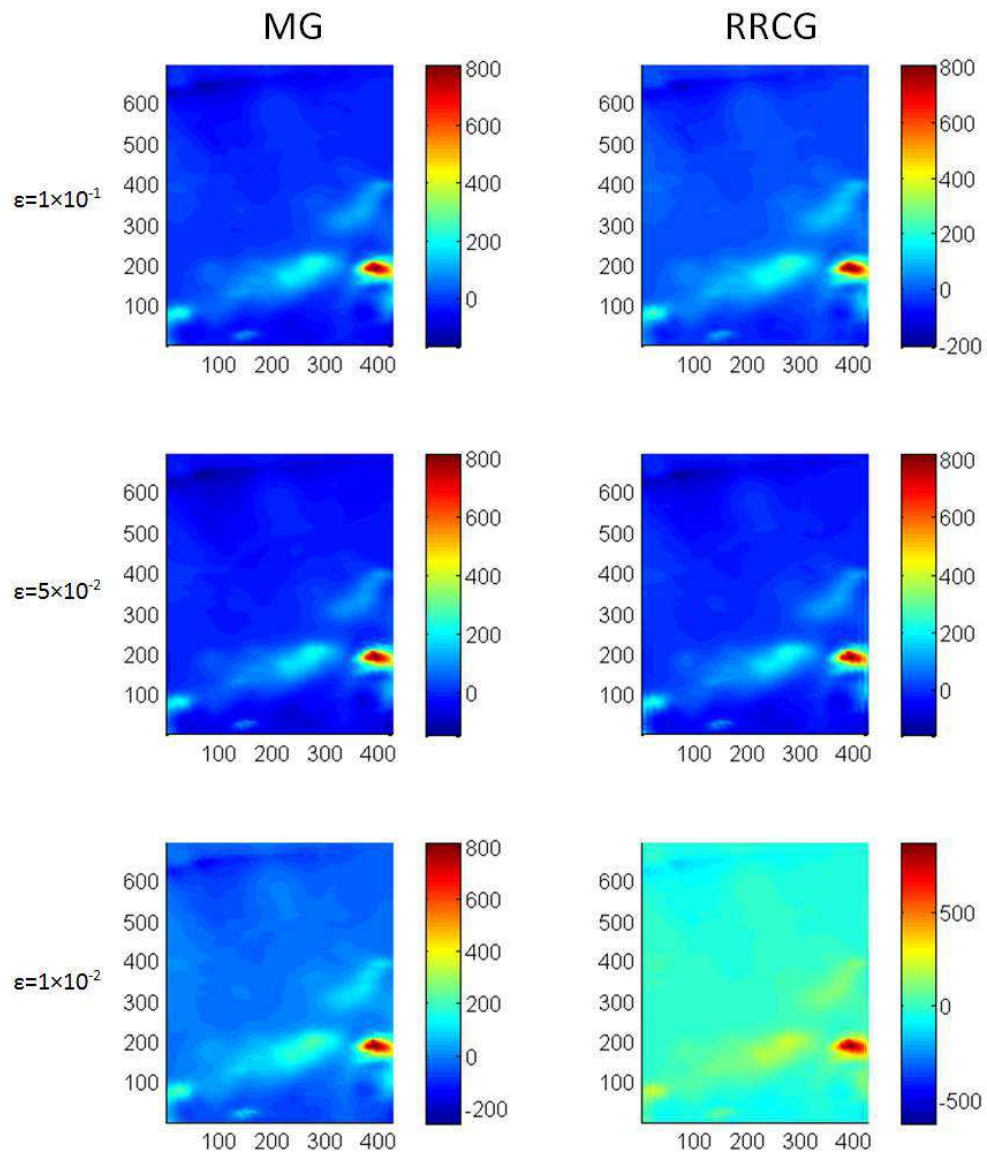


Figure 3.14: Inversion result for test case II at  $h = 100\text{m}$ .

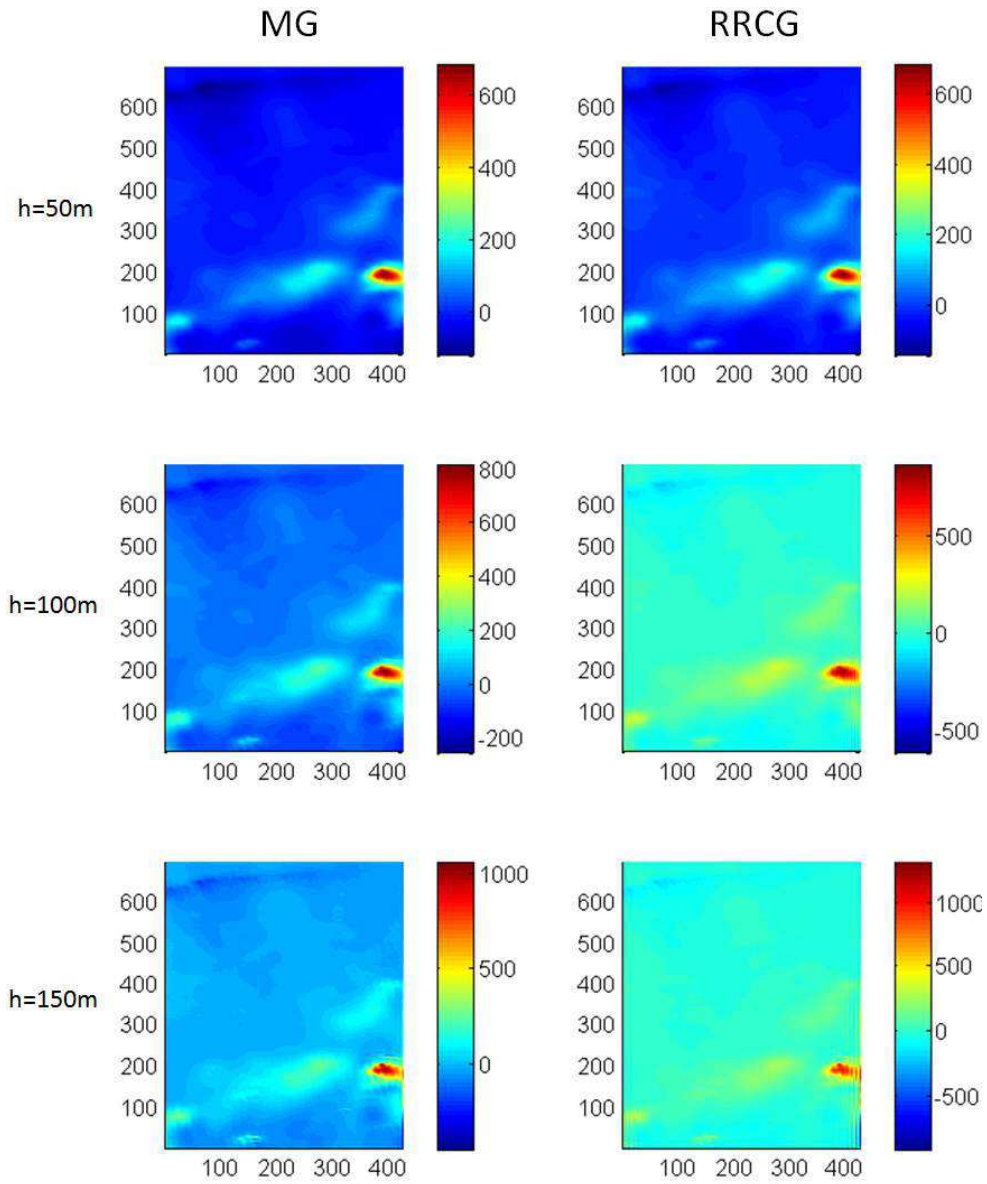


Figure 3.15: Inversion result for test case II with tolerance =  $1 * 10^{-2}$ .

much smaller edge-effect than the wavenumber domain method. However, applying to the same field data, proposed BTTB-MG method has a smaller edge-effect than the BTTB-RRCG method even when a small tolerance is applied. On the other hand, for the field data with modest noise level, the BTTB-MG method is as stable as BTTB-RRCG method.

It should be noted that when the noise level is high, the regularization should be used, and the BTTB-MG method can also be implemented by incorporating the regularization stabilizers.

### 3.3 Concluding Remarks

In this chapter, efficient multi-grid inversion schemes for magnetization inversion is developed. It is important to recognize that the inversion results can be computed by solving a symmetric Block-Toeplitz Toeplitz-Block (BTTB) system. The linear system is frequently large, dense and ill-conditioned. Direct implementation of the matrix coefficients will require considerable storage and leading to the requirement of large computing resources for the solution. By taking advantages of a symmetric BTTB property, the storage requirement can be reduced from  $O(N^2)$  to  $O(N)$  and the computational work for a typical iterative scheme decreases to  $O(N \log N)$  instead of  $O(N^2)$ . Therefore, efficient numerical inversion schemes can be developed, and they are capable of dealing with a large scale inversion problem.

It has been demonstrated that the RRCG and MG methods are effective numer-

ical tools for the inversion problems. Both methods have been tested to problems generated by synthetic data and real magnetic field data. Based on the numerical simulation, we conclude that for the field data with moderate perturbation, the BTTB-MG technique has a superior performance compared to the BTTB-RRCG method, in particular, the artifact near the boundary resulting from BTTB-MG is much less than that produced by the BTTB-RRCG. Moreover, significant saving in computing time is achieved by the BTTB-MG for all cases tested in this paper.

As a powerful structure in geophysical problem, the BTTB structure can be generalized to the 3D inversion problems, which will be discussed in the next chapter.

The work reported in this chapter has already been published in *International Journal of Numerical Analysis and Modeling* [120].

# Chapter 4

## 3D Inversion for Gravity Field Data

Gravity field survey is an essential step in prospecting of large areas in geophysical and environmental study. In many applications, meaningful underground information can be obtained from the density distribution. Similar to the magnetic field, inversion can be used to deduce the density from the observation gravity field, and the inversion solution is then sought by repeatedly computing the underground density according to the observation gravity. Unfortunately, there exists some structures producing a zero external gravity field. Therefore, for a given field data, there are infinite underground models generating exactly the same field. Hence, it is impossible to seek an exact solution from an inversion process. However, using prior information and/or applying regularization, we can obtain meaningful information from the observation.

In general, two techniques are commonly used for the three-dimension inversion schemes. The first one is based on the structural inversion, in which the structure information is obtained from inversion results, such as the Euler deconvolution [104], wavelet analysis [50], signal analysis [91, 7] and so on. The structural inversion techniques also include using models with certain properties such as inversion for

tabular anomalous [40, 87, 6, 88, 111], inversion for interfacing surface or anomaly boundaries [95, 83, 85].

The other technique is the generalized inversion based on discretizing the 3D underground into cells with constant susceptibility or density. To guarantee a unique solution, regularization or prior information should be incorporated. In particular, a smoothness regularization [64, 65] can be employed to produce a smooth inversion solution, whereas a focusing regularization [84, 125, 122, 124] is appropriate for a compact solution. The inversion solution largely depends on which stabilizer is used, but it may not be consistent with the real geological features. In some applications, adding prior information from previous experience or borehole data can result in certain geologic constraints [60]. To reduce the uncertainty in the inversion solution, cell-based inversion methods utilizing the assumption of certain physical property have been reported [12, 58]. For large scale potential field data, 3D inversion computation is a very challenging task and the solution requires significant computer resource. Hence, it is desirable to develop efficient numerical inversion schemes so that the solution can be computed rapidly with modest computing time and storage requirement. Recently, wavelet based methods [66, 29] have been considered to compress the sensitivity matrix by dropping small wavelet coefficients. Similar work includes the foot-print technique [26, 126], in which the threshold value to the sensitivity matrix is defined by users. Both wavelet method and moving foot-print technique aim at representing a dense matrix by a sparse ma-

trix. They can be applied to data domain and model domain [84, 4, 29, 46, 30]. In addition, down-sampling in data domain and model domain can further reduce the computation load with a cost of lowering the resolution of the inversion solution.

Compared with the 2-D problem in Chapters 2 and 3, a 3-D inversion produces a much larger system with dense and ill-conditioned matrix. The storage requirement of 3-D problem is of order  $O(n^2)$  and computational work per iteration of  $O(n^2)$ , while the  $n$  in 3-D can be significantly larger than that in 2-D problem. However, the computational complexity can be dramatically reduced from  $O(n^2)$  to  $O(n \log n)$  by using FFT based methods for regular field data. Pilkington applies a 2D Fourier transform for the 3-D magnetic field inversion. A 3-D Fourier transform method for the potential field inversion is also reported [13]. As discussed before, for an irregular or non-uniform data, fast gridding algorithms [10, 25, 9, 23] are available to convert irregular data into regular data, and the computational complexity is  $O(n)$ .

In this chapter, we propose a novel numerical scheme based on a 2-D multi-layer model for a 3-D gravity field inversion. The consistency and convergence are studied, and an error estimate is derived. Unlike the previous FFT-based schemes where FFT is applied to the kernel, the present scheme is directly applied by discretizing the proposed multi-layer model in the space domain, such that a BTTB structure is obtained. Moreover, the FFT is employed by embedding the BTTB matrix into a BCCB matrix. The BTTB-based scheme has attractive features in constructing preconditioning operator and regularization. Differed from the popular Conjugate

Gradient (CG) inversion scheme reported by Pilkington [82] utilizing a simple preconditioner in the form of diagonal matrix, the preconditioner presented here is optimal and it is in the form of BCCB matrix. Using recent mathematical results and properties related to BCCB and BTTB structures, optimal preconditioned CG solver can be accelerated by FFT, and a good convergence rate can be achieved. We also incorporate the regularization into the BTTB framework. To the best of our knowledge, the application of FFT for a general stabilizer have not been reported.

For a large scale 3-D inversion problem, the computation time usually can not be predetermined until the whole inversion is completed. In our work, numerical analysis including the convergence order of the computational scheme is presented. Useful information can then be extracted by carrying out inversions with various resolutions, and a reasonable computing time can be estimated for solving a large scale problem. We propose an improved penalty function so that it allows negative values in the recovered model unlike the conventional positive constrain in terms of logarithm substitution. Similar to a 2-D case, the numerical experiments presented in this study also indicates that the BTTB-based scheme induces little artifact at the boundary for a 3-D model, while the conventional FFT-based method produces significant error deteriorating the inversion solution. We validate the efficiency and the effectiveness of the BTTB-based inversion schemes, numerical simulations using synthetic and field data are reported. The computing time to recover a model with large number of unknowns is estimated confirming the proposed scheme is

capable of solving large scale inversions with a modest computing resource.

## 4.1 Gravity Field Forward Model

The gravity potential generated by a 3D density model is given by the first-kind Fredholm equation [122],

$$\mathbf{U}_g(\mathbf{r}') = \iiint_D K_g(\mathbf{r}, \mathbf{r}') \rho(\mathbf{r}) dv, \quad (4.1.1)$$

where  $\rho(\mathbf{r})$  is the density distribution,  $K_g(\mathbf{r}, \mathbf{r}')$  is the gravity potential Green's function. Since the division of the cells is determined before the inversion, then  $\rho(\mathbf{r})$  becomes constant in each prism, such that

$$\mathbf{U}_g(\mathbf{r}') = \sum_{i=1}^{N_m} \rho_i \iiint_D K_g(\mathbf{r}_i, \mathbf{r}') dv. \quad (4.1.2)$$

From equation (4.1.2),  $\iiint_D K_g(\mathbf{r}, \mathbf{r}') dv$  can be computed analytically [74]. Consequently, the coefficient matrix of the resulting linear system can be determined exactly. However, evaluating (4.1.2) for each cell is time consuming. An alternative procedure for solving (4.1.1) is to employ numerical discretization:

$$\mathbf{U}_g(\mathbf{r}') = \sum_{i=1}^{N_m} K_g(\mathbf{r}_i, \mathbf{r}') \rho_i \Delta x_i \Delta y_i \Delta z_i. \quad (4.1.3)$$

Both (4.1.2) and (4.1.3) lead to a linear system

$$\mathbf{d}_g = \mathbf{A}_g \rho. \quad (4.1.4)$$

It has been shown [124] that numerical discretization given in (4.1.3) can be as accurate as using the analytic solution (4.1.2), but the computational speed using discretization could be at least ten times faster. Therefore, numerical discretization is frequently preferred in real applications. Consider applying a discretization and let the general form of a potential field forward model be given by:

$$\mathbf{G}\mathbf{m} = \mathbf{d}, \quad (4.1.5)$$

where  $\mathbf{m}$  is the known underground model,  $\mathbf{G}$  is the sensitivity matrix, in which each element represents the effect of the  $\mathbf{m}_i$  to a observation point, and  $\mathbf{d}$  is the external field generated by the model. To achieve a unique solution with a specific physical property, instead of solving (4.1.5) directly, the Tikhonov regularization [105] is introduced, and we consider

$$\min \Phi = \|\mathbf{W}_d(\mathbf{d} - \mathbf{G}\mathbf{m})\|^2 + \mu\|\mathbf{W}_m(\mathbf{m} - \mathbf{m}_{\text{ref}})\|^2, \quad (4.1.6)$$

where  $\mu$  is the regularization parameter,  $\mathbf{m}_{\text{ref}}$  is the prior information,  $\mathbf{W}_d$  and  $\mathbf{W}_m$  are the data weighting matrix and the model weighting matrix, respectively. Other regularization terms can be used in (4.1.6) to achieve particular properties. The minimization problem can be solved by the following matrix equation:

$$(\mathbf{G}^T\mathbf{W}_d^T\mathbf{W}_d\mathbf{G} + \mu\mathbf{W}_m^T\mathbf{W}_m)\mathbf{m} = \mathbf{G}^T\mathbf{W}_d^T\mathbf{W}_d\mathbf{G}\mathbf{d} + \mu\mathbf{W}_m^T\mathbf{W}_m\mathbf{m}_{\text{ref}}. \quad (4.1.7)$$

Many efficient iterative schemes have been proposed to solve (4.1.7) [75, 64, 65, 82, 30]. It is not hard to verify that the matrix-vector product is the major

computational operation in an iterative scheme. Since  $\mathbf{G}$  is an  $n$ -by- $n$  full matrix, the cost for a matrix-vector product is  $O(n^2)$ .

### 4.1.1 Gravity field multi-layer model

Let  $\mathbf{g}(\mathbf{r})$  and  $\mathbf{U}_g(\mathbf{r})$  denote the gravity field and gravity potential at location  $\mathbf{r}$ . According to the potential theory,

$$\mathbf{g}(\mathbf{r}) = \nabla \mathbf{U}_g(\mathbf{r}), \quad (4.1.8)$$

since

$$\mathbf{U}_g(\mathbf{r}') = \gamma \iiint_D \frac{1}{|\mathbf{r} - \mathbf{r}'|} \rho(\mathbf{r}') dv, \quad (4.1.9)$$

then

$$\mathbf{g}(\mathbf{r}') = \gamma \iiint_D \frac{\mathbf{r} - \mathbf{r}'}{|\mathbf{r} - \mathbf{r}'|^3} \rho(\mathbf{r}') dv. \quad (4.1.10)$$

In real applications, the anomalous gravity field generated by an anomalous density underground is recorded. The real density distribution  $\rho(\mathbf{r})$  is a function of the location, and it can be decomposed into homogenous background density  $\rho_b$  which is a constant value and the anomalous density  $\Delta\rho(\mathbf{r})$ . Thus, the anomalous density  $\Delta\rho(\mathbf{r})$  can be calculated as the difference between the real density  $\rho(\mathbf{r})$  and the background homogenous density  $\rho_b$ :

$$\Delta\rho(\mathbf{r}) = \rho(\mathbf{r}) - \rho_b.$$

Therefore, a gravity anomaly is given by

$$I_3 = \Delta g_z(\mathbf{r}') = \gamma \iiint_D \Delta \rho(\mathbf{r}) \frac{z - z'}{|\mathbf{r} - \mathbf{r}'|^3} dv. \quad (4.1.11)$$

To solve the first-kind Fredholm equation (4.1.11), numerical discretization similar to (4.1.2) or (4.1.3) can be applied. However, instead of discretizing (4.1.11) directly, we consider splitting a 3D density model into a sequence of 2D models.

**Theorem 3.1** (Approximation of a forward model). A 3D density forward model  $\mathbf{I}_3$  given in (4.1.11) can be approximated by a 2D layer model  $\mathbf{I}_2$  as the following:

$$\mathbf{I}_2 \approx \gamma \iint_S \Delta m(x, y, h) \frac{t(h - z')}{|\mathbf{r} - \mathbf{r}'|^3} dx dy, \quad (4.1.12)$$

and the error of the approximation is bounded by

$$|\mathbf{I}_3 - \mathbf{I}_2| \leq C \frac{t}{h^2},$$

where  $t$  is thickness of the layer,  $h$  is the depth from the ground to the top of the layer, and  $C$  is a constant related to the maximum density contrast.

*Proof:* Assuming  $t$  is the thickness of the layer and  $h$  is the depth from the ground to the top of the layer, then the absolute value of the difference between  $\mathbf{I}_3$  and its approximation  $\mathbf{I}_2$  is given by

$$\begin{aligned} |\mathbf{I}_3 - \mathbf{I}_2| &= \left| \iiint_V \rho(x, y, z) \frac{z - z'}{|(x - x')^2 + (y - y')^2 + (z - z')^2|^{3/2}} dx dy dz \right. \\ &\quad \left. - \iint_S \rho(x, y, h) \frac{t(h - z'){|(x - x')^2 + (y - y')^2 + (h - z')^2|^{3/2}} dx dy \right| \\ &= \left| \iiint_V \rho(x, y, z) K(x, y, z) dx dy dz - t \iint_S \rho(x, y, h) K(x, y, h) dx dy \right| \end{aligned}$$

$$\begin{aligned}
&= \left| \iiint_V \rho(x, y, z)K(x, y, z)dxdydz - \int_h^{h+t} \iint_S \rho(x, y, h)K(x, y, h)dxdydz \right| \\
&\leq \iiint_V |\rho(x, y, z)K(x, y, z) - \rho(x, y, h)K(x, y, h)|dxdydz \\
&\leq \iiint_V |z - h| \sup_{z \in [h, h+t]} \left| \frac{\partial}{\partial z} [\rho(x, y, z)K(x, y, z)] \right| dxdydz \\
&\leq t \iiint_V \sup_{z \in [h, h+t]} |\partial_z \rho K(x, y, z) + \rho \partial_z K(x, y, z)| dxdydz.
\end{aligned}$$

Since

$$\begin{aligned}
&|\partial_z \rho K(x, y, z) + \rho \partial_z K(x, y, z)| \\
&= \left| \rho_z K(x, y, z) + \rho \frac{\partial}{\partial z} \frac{z - z'}{((x - x')^2 + (y - y')^2 + (z - z')^2)^{3/2}} \right| \\
&= \left| \rho_z \frac{z - z'}{[(x - x')^2 + (y - y')^2 + (z - z')^2]^{3/2}} + \right. \\
&\quad \left. \rho \frac{[(x - x')^2 + (y - y')^2 + (z - z')^2]^{1/2} - 3(z - z')^2}{[(x - x')^2 + (y - y')^2 + (z - z')^2]^{5/2}} \right| \\
&\leq \frac{1}{h} \left[ |\rho_{z_{\max}}| \frac{1}{h} + |\rho_{\max}| \frac{1}{h^3} + 3|\rho_{\max}| \frac{1}{h^2} \right] \\
&\leq |\rho_{z_{\max}}| \frac{1}{h^2} \quad \text{as } h \rightarrow \infty.
\end{aligned}$$

Therefore,

$$\begin{aligned}
|\mathbf{I}_3 - \mathbf{I}_2| &\leq t \iiint_V |\partial_z \rho K(x, y, z) + \rho \partial_z K(x, y, z)| dxdydz \\
&\leq \frac{t}{h^2} |\rho_{z_{\max}}| V = C \frac{t}{h^2}. \quad \blacksquare
\end{aligned}$$

According to Theorem 3.1 and considering the linearity and additivity of the potential fields, the error of the resulting gravity field is strictly bounded when approximating a 3D density model by a 2D multi-layer model. Since the goal is to seek the underground density distribution from a observed gravity field, we need

to verify that using the same data set, the inversion solution by solving a sequence of 2D models is converging to the solution of original 3D model. To prove the convergence, we use the Theorem 3.2 stated in the following.

**Theorem 3.2** (Approximation to the identity). Suppose that the least decreasing radial majorant of  $\varphi$  is integrable; i.e. let  $\psi(x) = \sup_{|y| \geq |x|} |\varphi(y)|$ , and we suppose  $\int_{\mathbf{R}^n} \psi(x) dx = A < \infty$ . Then with the same  $A$ ,

$$(a) \sup_{\varepsilon > 0} |(f * \varphi_\varepsilon)(x)| \leq AM(f)(x), f \in L^p(\mathbf{R}^n), 1 \leq p \leq \infty.$$

$$(b) \text{ If in addition } \int_{\mathbf{R}^n} \varphi(x) dx = 1, \text{ then } \lim_{\varepsilon \rightarrow 0} (f * \varphi_\varepsilon)(x) = f(x) \text{ almost everywhere.}$$

$$(c) \text{ If } p < \infty, \text{ then } \|f * \varphi_\varepsilon - f\|_p \rightarrow 0, \text{ as } \varepsilon \rightarrow 0.$$

By using Theorem 3.2, we are able to obtain the following Theorem 3.3 for the convergence of the solution:

**Theorem 3.3** (Convergence). Assume  $\mathbf{b}$  is the observation field data, let  $\mathbf{u}_3 = \mathbf{I}_3^{-1}(\mathbf{b})$  be the exact solution obtained by solving a 3D forward model, and  $\mathbf{u}_2 = \mathbf{I}_2^{-1}(\mathbf{b})$  be the numerical solution by solving a 2D forward model, then

$$|\mathbf{u}_3 - \mathbf{u}_2| \leq M_1 \frac{t}{h^2} + M_2 \frac{t^2}{h^3},$$

where  $t$  is the thickness of the layer,  $h$  is the depth from the ground to the top of the layer,  $M_1$  and  $M_2$  are constants.

*Proof:* Suppose we have  $u_3 = \rho(x, y, z)$  and  $u_2 = m(x, y, h)$ , such that

$$\iiint_D \rho(x, y, z) K(x - x', y - y', z - z') dx dy dz = b,$$

$$\iiint_D m(x, y, h)K(x - x', y - y', h - z')dxdydz = b,$$

then,

$$\begin{aligned} & \iiint_D \rho(x, y, z)K(x - x', y - y', z - z')dxdydz - \\ & \quad \iiint_D m(x, y, h)K(x - x', y - y', h - z')dxdydz \\ &= \iiint_D [\rho(x, y, z) - m(x, y, h)]K(x - x', y - y', z - z')dxdydz + \\ & \quad \iiint_D m(x, y, h)[K(x - x', y - y', z - z') - K(x - x', y - y', h - z')]dxdydz \\ &= \text{part I} + \text{part II} = 0. \end{aligned}$$

According to the mean value theorem,

$$\text{part II} \leq \iiint_D m(x, y, h)t \sup_{z \in [h, h+t]} \partial_z K(x - x', y - y', z - z')dxdydz.$$

Since

$$\begin{aligned} & \partial_z \frac{z - z'}{[(x - x')^2 + (y - y')^2 + (z - z')^2]^{3/2}} \\ &= \frac{1}{[(x - x')^2 + (y - y')^2 + (z - z')^2]^{3/2}} - \frac{3(z - z')^2}{[(x - x')^2 + (y - y')^2 + (z - z')^2]^{5/2}} \\ &\leq \frac{1}{(z - z')^3} + \frac{3(z - z')^2}{(z - z')^5} \leq \frac{4}{h^3}, \end{aligned}$$

therefore,

$$\begin{aligned} \text{part II} &\leq \frac{4t}{h^3} \iiint_D m(x, y, h)dxdydz \leq M \frac{t^2}{h^3}, \\ |\text{part I}| &= |\text{part II}| \leq M \frac{t^2}{h^3}. \end{aligned} \tag{4.1.13}$$

Now, what we actually want is to investigate is  $|\rho(x, y, z) - m(x, y, h)|$ , which is

given in part I. Let

$$f(x, y, z) = \rho(x, y, z) - m(x, y, h),$$

and set

$$H(x, y, z) = \frac{1}{(x^2 + y^2 + z^2)^{\frac{3}{2}}},$$

then choose

$$H_\varepsilon(x, y, z) = \frac{1}{\varepsilon^3} \frac{1}{\left(\left(\frac{x}{\varepsilon}\right)^2 + \left(\frac{y}{\varepsilon}\right)^2 + \left(\frac{z}{\varepsilon}\right)^2\right)^{\frac{3}{2}}} = H(x, y, z).$$

According to Theorem 3.2 (c),

$$f(x, y, z) \approx \lim_{\varepsilon \rightarrow 0} f * H_\varepsilon(x, y, z) = f * H(x, y, z),$$

therefore

$$\begin{aligned} |f(x', y', z')| &= f * H(x', y', z') \\ &= \left| \int_D f(x, y, z) H(x' - x, y' - y, z' - z) dv \right| \\ &\leq \left| \int_D f(x, y, z) K(x' - x, y' - y, z' - z) dv \right| \\ &+ \left| \int_D f(x, y, z) (H(x' - x, y' - y, z' - z) - K(x' - x, y' - y, z' - z)) dv \right|. \end{aligned}$$

Since

$$\begin{aligned} &|H(x - x', y - y', z - z') - K(x - x', y - y', z - z')| \\ &= \frac{|1 - (z - z')|}{\left|[(x - x')^2 + (y - y')^2 + (z - z')^2]^{\frac{3}{2}}\right|} \end{aligned}$$

$$\leq \frac{\frac{1}{2}h}{h^3} \leq \frac{1}{2h^2},$$

and recalling (4.1.13),

$$|\rho(x, y, z) - m(x, y, h)| = |f(x, y, z)| \leq M_1 \frac{t}{h^2} + M_2 \frac{t^2}{h^3}. \quad \blacksquare$$

## 4.2 BTTB-based Gravity Inversion

The most attractive feature of using a 2D multi-layer model is that the resulting linear system in each layer has a BTTB structure. Denote the dimension of each layer as  $N$ -by- $M$ , then by discretizing (4.1.12), the 2D equation can be expressed as

$$d(x(i), y(i), z(i)) = Ct \sum_{j=1}^N \sum_{k=1}^M K(x(i), y(i), z(i), x'(j), y'(k), h) m(x'(j), y'(k), h) \Delta x \Delta y, \quad (4.2.1)$$

which can then be rewritten as

$$d(x(i), y(i), z(i)) = Ct \sum_{l=1}^{N \times M} K(x(i), y(i), z(i), x'(l), y'(l), h) m(x'(l), y'(l), h) \Delta x \Delta y, \quad (4.2.2)$$

where

$$K(i, l, h) = \frac{h - z}{[(x(i) - x(l))^2 + (y(i) - y(l))^2 + (h - z)^2]^{3/2}}. \quad (4.2.3)$$

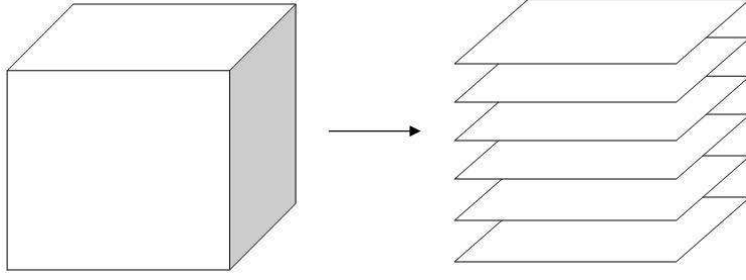


Figure 4.1: Uniform splitting of a 3D forward gravity model.

Thus, equation (4.1.12) can be approximated by a sequence of linear systems

$$\mathbf{d}_i = \mathbf{G}_i \mathbf{m}_i, \quad i = 1, \dots, N_l, \quad (4.2.4)$$

where  $\mathbf{d}_i$  is the  $N \times M$  gravity field generated by the  $i$ th layer,  $\mathbf{m}_i$  is the density in the  $i$ th layer,  $N_l$  is the number of layers in a multi-layer model, and  $\mathbf{G}_i$  is  $(N \times M)$  by  $(N \times M)$  BTTB matrix at the corresponding layer. The BTTB matrix is given as in (2.2.5).

Now, consider splitting a 3D density model into a sequence of 2D model as shown in Figure 4.1. Suppose a 3D model is split into  $N_l$  layers, then the forward model for the potential field become

$$\mathbf{d} = \mathbf{T}_1 \mathbf{m}_1 + \mathbf{T}_2 \mathbf{m}_2 + \dots + \mathbf{T}_{N_l} \mathbf{m}_{N_l}, \quad (4.2.5)$$

where  $\mathbf{T}_k$  is the BTTB matrix defined in (2.2.5),  $\mathbf{m}_k$  is the density distribution at the  $k$ th layer,  $k = 1, 2, \dots, N_l$ . Thus, (4.2.5) can be rewritten as

$$\mathbf{d} = \mathbf{T} \mathbf{m}, \quad (4.2.6)$$

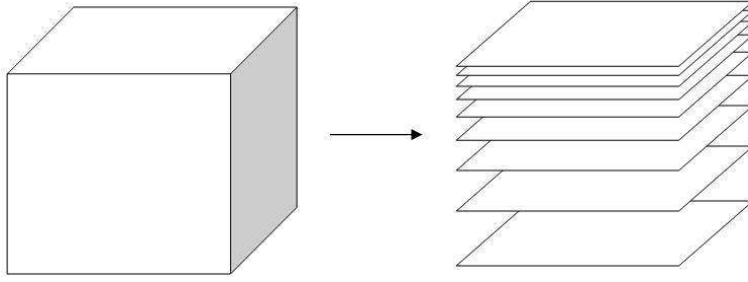


Figure 4.2: Non-uniform splitting of a 3D forward gravity model.

where

$$\mathbf{T} = \begin{bmatrix} \mathbf{T}_1 & \mathbf{T}_2 & \cdots & \mathbf{T}_{N_t} \end{bmatrix}, \quad \mathbf{m} = \begin{bmatrix} \mathbf{m}_1 & \mathbf{m}_2 & \cdots & \mathbf{m}_{N_t} \end{bmatrix}^T.$$

Different from (3.1.11), the coefficient matrix  $\mathbf{T}$  here is a non-square matrix, therefore solving equation (4.2.6) is an inherently under-determined problem.

Another important feature of a multi-layer model is that the thickness of each layer is not fixed. According to Theorem 3.1 and Theorem 3.3, the error in the inversion solution is proportional to the layer thickness  $t$ , and inversely proportional to the depth of the layer  $h$ . Therefore, as illustrated in Figure 4.2, the thickness of a shallow layer can be chosen smaller, and the thickness of a deeper layer can be chosen larger. The BTTB structure always exists and is independent with respect to the vertical splitting of the density model.

### 4.2.1 Preconditioner for BTTB system

A powerful tool to accelerate the convergence rate for the CG iterative method is to introduce a preconditioning operator. To be an effective preconditioner the operator

must be a good approximation to the original matrix and the inverse must be easier computed. For a sparse matrix problem, popular and effective preconditioning can be constructed based on incomplete Gaussian elimination or approximate Cholesky factorization, etc. For a full matrix problem considered in this study, the preconditioning is usually based on a diagonal matrix [82]. However, by utilizing the BTTB framework, we can now construct an optimal preconditioner [17]. Starting with a general block matrix  $\mathbf{A}$ :

$$\mathbf{A} = \begin{bmatrix} \mathbf{A}_{1,1} & \mathbf{A}_{1,2} & \cdots & \mathbf{A}_{1,m} \\ \mathbf{A}_{2,1} & \mathbf{A}_{2,2} & \cdots & \mathbf{A}_{2,m} \\ \vdots & \ddots & \ddots & \vdots \\ \mathbf{A}_{m,1} & \mathbf{A}_{m,2} & \cdots & \mathbf{A}_{n,m} \end{bmatrix}, \quad (4.2.7)$$

where  $\mathbf{A}_{i,j} \in \mathbb{C}^{n \times n}$ . Define the matrix operator

$$c_{\hat{\mathbf{V}} \otimes \hat{\mathbf{U}}}(\mathbf{A}_{mn}) = (\hat{\mathbf{V}} \otimes \hat{\mathbf{U}})^* \delta[(\hat{\mathbf{V}} \otimes \hat{\mathbf{U}}) \mathbf{A}_{mn} (\hat{\mathbf{V}} \otimes \hat{\mathbf{U}})^*] (\hat{\mathbf{V}} \otimes \hat{\mathbf{U}}), \quad (4.2.8)$$

where  $\delta[\mathbf{A}]$  denotes the diagonal matrix of  $\mathbf{A}$ , and  $\hat{\mathbf{V}}$  and  $\hat{\mathbf{U}}$  are  $m$ -by- $m$  and  $n$ -by- $n$  unitary matrix. Let

$$\mathcal{M}_{\mathbf{V} \otimes \mathbf{U}} \equiv \{(\mathbf{V} \otimes \mathbf{U})^* \Lambda_{mn} (\mathbf{V} \otimes \mathbf{U}) \mid \Lambda_{mn} \text{ is any } mn\text{-by-}mn \text{ diagonal matrix}\},$$

where  $\mathbf{V}$  and  $\mathbf{U}$  are any given  $m$ -by- $m$  and  $n$ -by- $n$  unitary matrix, respectively,  $\otimes$  is the tensor product, then the optimal preconditioner can be obtained from the following theorem.

**Theorem 3.4** [15]. For any arbitrary matrix  $\mathbf{A}_{mn} \in \mathbb{C}^{mn \times mn}$  given in (4.2.7), let

$c_{\mathbf{V} \otimes \mathbf{U}}(A_{mn})$  be the minimizer of  $\|\mathbf{W}_{mn} - \mathbf{A}_{mn}\|_{\mathcal{F}}$  over all  $\mathbf{W}_{mn} \in \mathcal{M}_{\mathbf{V} \otimes \mathbf{U}}$ , where  $c_{\mathbf{V} \otimes \mathbf{U}}$  is the point operator. Then the optimal preconditioner for matrix (4.2.7) is given by

$$c_{\mathbf{V}, \mathbf{U}}^{(2)}(\mathbf{A}_{mn}) = c_{\mathbf{V} \otimes \mathbf{U}}(\mathbf{A}_{mn}).$$

According to Theorem 3.4 and for any BTTB matrix, the optimal preconditioner  $c_{\mathbf{F}, \mathbf{F}}^{(2)}(\mathbf{A}_{mn})$  can also be expressed in the form of BCCB matrix [15]:

$$c_{\mathbf{F}, \mathbf{F}}^{(2)}(\mathbf{A}_{mn}) = \frac{1}{mn} \sum_{j=0}^{m-1} \sum_{k=0}^{n-1} \left( \sum_{p-q \equiv j \pmod{m}} \sum_{r-s \equiv k \pmod{n}} (\mathbf{A}_{p,q})_{rs} \right) (\mathbf{Q}^j \otimes \mathbf{Q}^k) \quad (4.2.9)$$

## 4.2.2 BTTB-based least squares solver

Since the system (4.2.6) is a non-square matrix, the solution can be computed by considering the problem

$$\min \Phi = \|\mathbf{d} - \mathbf{T}\mathbf{m}\|_2, \quad (4.2.10)$$

which can be solved by applying the CG method to the normal equation

$$\mathbf{T}^*(\mathbf{d} - \mathbf{T}\mathbf{m}) = 0. \quad (4.2.11)$$

To avoid explicitly forming  $\mathbf{T}^*\mathbf{T}$ , CG method applied to the normal equation (CGNR) [8, 77] was developed. The preconditioned CGNR (PCG NR) method for solving (4.2.11) is given in the following.

**PCG NR.** Let  $\mathbf{m}_0$  be an initial guess to  $\mathbf{T}\mathbf{m} = \mathbf{d}$ , and let  $\mathbf{C}$  be a given preconditioner.

$$\mathbf{r}_0 = \mathbf{d} - \mathbf{T}\mathbf{m}_0$$

$$\mathbf{p}_0 = \mathbf{s}_0 = \mathbf{C}^{-1*}\mathbf{T}^*\mathbf{r}_0$$

$$\gamma_0 = \|\mathbf{s}_0\|_2^2$$

for  $k = 0, 1, 2, \dots$

$$\mathbf{q}_k = \mathbf{T}\mathbf{C}^{-1}\mathbf{p}_k$$

$$\alpha_k = \gamma_k / \|\mathbf{q}_k\|_2^2$$

$$\mathbf{m}_{k+1} = \mathbf{m}_k + \alpha_k \mathbf{C}^{-1}\mathbf{p}_k$$

$$\mathbf{r}_{k+1} = \mathbf{r}_k - \alpha_k \mathbf{q}_k$$

$$\mathbf{s}_k = \mathbf{C}^{-1*}\mathbf{T}^*\mathbf{r}_{k+1}$$

$$\gamma_{k+1} = \|\mathbf{s}_{k+1}\|_2^2$$

$$\beta_k = \gamma_{k+1} / \gamma_k$$

$$p_{k+1} = s_{k+1} + \beta_k p_k.$$

The PCGMR can be used to solve non-square matrix system (4.2.6). It should be noted that a regularization can also be added to the normal equation. Recall that the objective function to be minimized is

$$\min \Phi = \|\mathbf{W}_d(\mathbf{d} - \mathbf{T}\mathbf{m})\|^2 + \mu\|\mathbf{W}_m(\mathbf{m} - \mathbf{m}_{\text{ref}})\|^2. \quad (4.2.12)$$

where  $\mu$  is the regularization parameter,  $\mathbf{m}_{\text{ref}}$  is the prior information,  $\mathbf{W}_d$  and  $\mathbf{W}_m$  are the data weighting matrix and the model weighting matrix respectively.

When no prior information is available, we set  $\mathbf{m}_{\text{ref}} = 0$ , such that the mini-

mization problem (4.1.6) can be rewritten in the following form [16],

$$\min \Phi = \left\| \begin{bmatrix} \mathbf{W}_d \mathbf{d} \\ 0 \end{bmatrix} - \begin{bmatrix} \mathbf{W}_d \mathbf{T} \\ \mu \mathbf{W}_m \end{bmatrix} \mathbf{m} \right\|^2. \quad (4.2.13)$$

By setting

$$\hat{\mathbf{T}} = \begin{bmatrix} \mathbf{W}_d \mathbf{T} \\ \mu \mathbf{W}_m \end{bmatrix}, \quad \hat{\mathbf{d}} = \begin{bmatrix} \mathbf{W}_d \mathbf{d} \\ 0 \end{bmatrix},$$

the PCGNR can now be applied to (4.2.12). By changing the structure of  $\mathbf{W}_m$ , different type of regularization can be developed, and this will be discussed in next section.

## 4.3 BTTB-based regularization

### 4.3.1 Smoothness stabilizer

The aim of a stabilizing functional or stabilizer is to select an appropriate model according to prior information or the geological knowledge provided by a user. When some prior information is available, the simplest regularization is to minimize the difference between the current model and the prior model:

$$\Phi_m(\mathbf{m}) = \iiint_V (\mathbf{m} - \mathbf{m}_{\text{ref}})^2 dv, \quad (4.3.1)$$

such that the weighting matrix  $\mathbf{W}_m$  in (4.1.6) is the identity matrix  $\mathbf{I}$ .

To generate a smooth transition, consider a smoothness regularization [64, 65, 58] as follows

$$\Phi_m(\mathbf{m}) = \alpha_s \iiint_V w_s \{w(z)[\mathbf{m} - \mathbf{m}_{\text{ref}}]\}^2 dv \quad (4.3.2)$$

$$+ \alpha_x \iiint_V w_x \left\{ \frac{\partial w(z)[\mathbf{m} - \mathbf{m}_{\text{ref}}]}{\partial x} \right\}^2 dv \quad (4.3.3)$$

$$+ \alpha_y \iiint_V w_y \left\{ \frac{\partial w(z)[\mathbf{m} - \mathbf{m}_{\text{ref}}]}{\partial y} \right\}^2 dv \quad (4.3.4)$$

$$+ \alpha_z \iiint_V w_z \left\{ \frac{\partial w(z)[\mathbf{m} - \mathbf{m}_{\text{ref}}]}{\partial z} \right\}^2 dv, \quad (4.3.5)$$

here,  $w_s$ ,  $w_x$ ,  $w_y$ ,  $w_z$ ,  $\alpha_s$ ,  $\alpha_x$ ,  $\alpha_y$  and  $\alpha_z$  are the weighting parameters which are chosen to balance the importance among (4.3.2) (4.3.3) (4.3.4) and (4.3.5),  $w(z)$  is the depth weighting function to counteract the geometric decay of the kernels. The smoothness stabilizing functional can be efficiently utilized by using BTTB structure. Assuming a 3D density or susceptibility model is split into  $N_l$  layers as displayed in Figure 4.1, and denote the density distribution in  $i$ th layer as  $\mathbf{M}^{(i)}$ ,  $i = 1, \dots, N_l$ , then the  $\mathbf{M}^{(i)}$  can be given in the following form,

$$\mathbf{M}^{(i)} = \begin{bmatrix} m_1^{(i)} & m_{N+1}^{(i)} & \dots & m_{(M-1)N+1}^{(i)} \\ m_2^{(i)} & m_{N+2}^{(i)} & \dots & m_{(M-1)N+2}^{(i)} \\ \vdots & \vdots & \ddots & \vdots \\ m_N^{(i)} & m_{2N}^{(i)} & \dots & m_{MN}^{(i)} \end{bmatrix}, \quad (4.3.6)$$

such that the density distribution in a 3D model can be reformed into a vector as

$$\mathbf{m} = \left[ m_1^{(1)} \quad m_2^{(1)} \quad \dots \quad m_{MN}^{(1)} \quad m_1^{(2)} \quad \dots \quad m_{MN}^{(2)} \quad m_1^{(3)} \quad \dots \quad m_{MN}^{(N_i)} \right]^T \quad (4.3.7)$$

From (4.3.6) and (4.3.7), the partial derivative in (4.3.3) (4.3.4) and (4.3.5) can be denoted as

$$\frac{\partial \mathbf{m}}{\partial x} = \frac{1}{\Delta x} \begin{bmatrix} \mathbf{T}^{(1)} & & & \\ & \mathbf{T}^{(2)} & & \\ & & \ddots & \\ & & & \mathbf{T}^{(N_i)} \end{bmatrix} \mathbf{m} = \mathbf{A} \mathbf{m}, \quad (4.3.8)$$

where

$$\mathbf{T}^{(i)} = \begin{bmatrix} \mathbf{T}_1 & & & \\ & \mathbf{T}_2 & & \\ & & \ddots & \\ & & & \mathbf{T}_M \end{bmatrix}, \quad \mathbf{T}_j = \begin{bmatrix} 1 & -1 & & \\ & 1 & -1 & \\ & & \ddots & \ddots \\ & & & 1 \end{bmatrix}_{N \times N} \quad (4.3.9)$$

$$\frac{\partial \mathbf{m}}{\partial y} = \frac{1}{\Delta y} \begin{bmatrix} \mathbf{G}^{(1)} & & & \\ & \mathbf{G}^{(2)} & & \\ & & \ddots & \\ & & & \mathbf{G}^{(N_i)} \end{bmatrix} \mathbf{m} = \mathbf{B} \mathbf{m}, \quad (4.3.10)$$

where

$$\mathbf{G}^{(i)} = \begin{bmatrix} \mathbf{I} & -\mathbf{I} & & & \\ & \mathbf{I} & -\mathbf{I} & & \\ & & \ddots & \ddots & \\ & & & \mathbf{I} & -\mathbf{I} \\ & & & & \mathbf{I} \end{bmatrix}_{M \times M}, \mathbf{I} \text{ is } N \times N \text{ identity matrix.} \quad (4.3.11)$$

$$\frac{\partial \mathbf{m}}{\partial z} = \mathbf{C} \mathbf{m}, \quad (4.3.12)$$

where

$$\mathbf{C} = \frac{1}{\Delta z} \begin{bmatrix} \mathbf{I} & -\mathbf{I} & & & \\ & \mathbf{I} & -\mathbf{I} & & \\ & & \ddots & \ddots & \\ & & & \mathbf{I} & -\mathbf{I} \\ & & & & \mathbf{I} \end{bmatrix}_{N_t \times N_t}, \mathbf{I} \text{ is } MN \times MN \text{ identity matrix.} \quad (4.3.13)$$

Since  $\mathbf{A}$ ,  $\mathbf{B}$  and  $\mathbf{C}$  are BTTB matrices, the overall smoothness regularization can be expressed in a BTTB framework. Notice that, other regularization stabilizers can also be transformed into BTTB form, such as the minimization of the Laplacian of model parameters [122]:

$$\Phi_m(\mathbf{m}) = \|\nabla^2 \mathbf{m}\|^2. \quad (4.3.14)$$

In addition to the smoothness stabilizer, the focusing regularization has been proposed to achieve compact inversion results. The minimum support (MS) stabi-

lizer [122] and the minimum gradient support (MGS) stabilizer [27] can be incorporated into the BTTB framework.

### 4.3.2 Reweighted parameter, depth weighting function and positivity constraint

Using the BTTB framework, we now define a data misfit functional  $\Phi_d = \|\mathbf{d} - \mathbf{T}\mathbf{m}\|_2$  and apply the regularization stabilizer  $\Phi_m$  presented in Section 4.3.1. To achieve a meaningful and accurate inversion solution in real applications, more factors including regularization parameter  $\alpha$ , depth weighting function  $w(z)$ , and positivity constraint should be considered.

The regularization parameter  $\alpha$  determines the degree of smoothness or compactness. However, choosing an appropriate value for  $\alpha$  is a hard problem. The prior information and the degree of perturbation will be useful to estimate  $\alpha$  [1], and the cross-validation method is also available [8]. The trial and error method [33, 108] and the L-curve technique [49] are frequently used when little prior information is known. Here, the trial and error method is employed to determine the initial value for the regularization parameter  $\alpha_0$ .

In this study, the solver is based on the re-weighted regularized conjugate gradient method (RRCG) given in section 2.2, where the regularization parameter  $\alpha$  will be updated in each iteration.

Since the gravity potential kernel decreases with the depth, the inversion with

a smoothness regularization tends to generate a density distribution concentrating near the surface. It has been shown that using a weighting function [64, 65] is an effective way to counteract the decay of a kernel, and the weighting function is given in the form of

$$w(z) = \frac{1}{(z + z_0)^\beta}, \quad (4.3.15)$$

where  $\beta$  is chosen in the range of  $1.0 < \beta < 1.5$ .

To guarantee the positivity of the inversion solution, conventionally a logarithmic substitution  $m = \ln(k)$  [65] is used such that the recovered model is strictly positive. Here, we propose a positivity constraint in the form of a linear penalty function:

$$p(x) = \begin{cases} x & x \geq 0 \\ Cx & x < 0 \end{cases}, \quad (4.3.16)$$

where  $C$  is the penalty parameter controlling the constraint degree. The proposed penalty function allows a negative value in the recovered model. Particularly, the penalty parameter provides a flexibility to recover the model for different field data. Notice that, the parameter  $C$  can be chosen larger if the field data is strictly positive, and  $C$  should be smaller if there exists negative field data. Numerical experiments show that for the field data without negative value, the parameter  $C$  can be chosen from 200 to 4000, and the inversion results are not sensitive to a wide range of values for  $C$ .

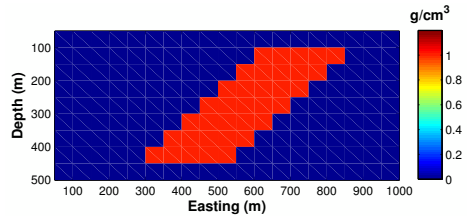
Compared with the FFT-based methods, another advantage of the BTTB structure is that it produces little artifacts near the boundary. This attractive property makes the BTTB structure has potential to be a powerful tool in many other geophysical applications.

## 4.4 Numerical Results

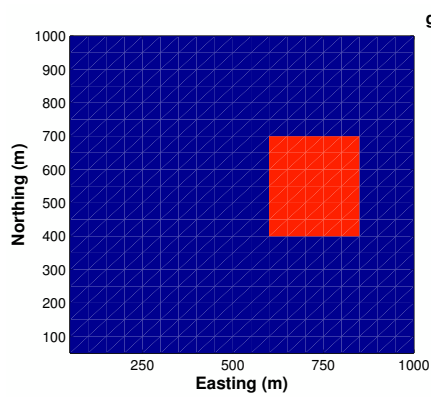
To demonstrate the power of the proposed BTTB-based scheme, computational simulations using the synthetic data and the field data are reported. The synthetic density models tested in this section have also been investigated for 3D numerical inversions [64, 65, 93]. All computation was performed on a Laptop with i7-3632QM CPU and 12GB RAM.

### 4.4.1 Synthetic data

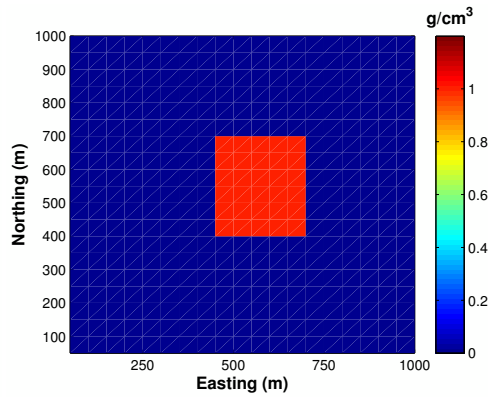
The first test case is taken from a numerical example investigated by many researchers [64, 65, 93], where Figure 4.3 represents a synthetic density model consisting of a dipping dyke with density  $1.0 \text{ g/cm}^3$ . By inverting the resultant gravity field shown in Figure 4.4, and compare the inversion result with the original synthetic density model, we evaluate the effectiveness of the proposed inversion scheme.



(a) Longitudinal section at North = 500m



(b) Cross section at Depth = 75m



(c) Cross section at Depth = 225m

Figure 4.3: Synthetic density model I.

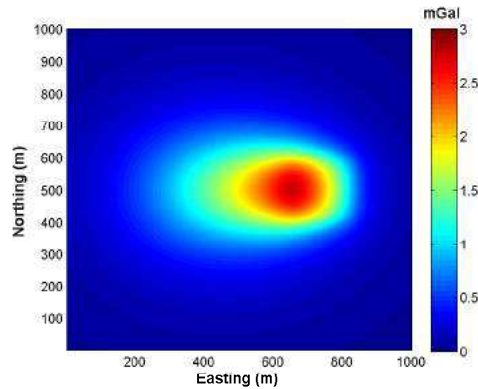
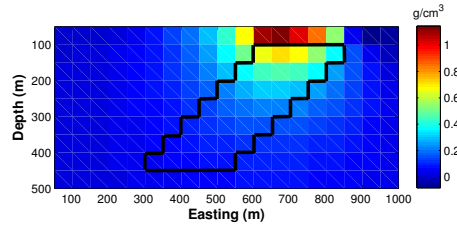
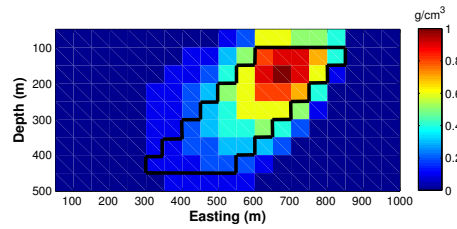
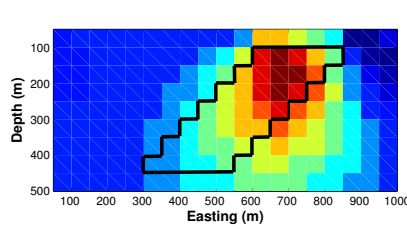


Figure 4.4: Gravity field generated by synthetic model I, unit of the gravity field in mGal.



(a) Inversion without constrain



(b) Inversion with depth weighting constrain (c) Inversion with positivity and depth weighting constrain

Figure 4.5: Inversion result with different constraints.

The dimension of the generated field is 1000m by 1000m as shown in Figure 4.4. We vertically split the density model every 50m into 10 layers, and in each layer, the cell size is chosen to be 50m by 50m, such that there are 20 by 20 cells in each layer. Note that the cell number in the model is related to a given resolution, for example, when a recovered resolution is  $20 \times 20 \times 10$  for the synthetic model I, the density model contains 4,000 cells. In Figure 4.5, the effect due to the depth weighting function (4.3.15) and positivity constraint (4.3.16) are displayed. The exact density distribution is contoured by black line. Without the depth weighting and positivity constraint, Figure 4.5(a) reveals that the density tends to concentrate at the surface and some negative values are observed. In Figure 4.5(b), the solution has a vertical resolution due to the use of the depth weighting function. The application of a depth weighting can offset the decay of the kernel such that each model parameter

is provided with an equal opportunity to have anomalous values [64, 65]. Without a negative penalty function, part of the solutions could remain negative. The effect of a penalty function is clearly shown in Figure 4.5(c). When applying a depth weighting and positivity constraint together, the vertical resolution and the density value are well recovered as illustrated in Figure 4.5(c).

In investigating the robustness of the proposed scheme, an extra 2% Gaussian noise is added to the resultant observation data. The inversion results using the perturbed data are shown in Figure 4.6. It is observed that the dipping shape in recovered model is accurate, and this confirms that the numerical scheme is robust even when the perturbed data is used. To examine the sensitivity effect due to the parameter  $\alpha$ , Figure 4.5(c) presents the inversion results using the regularization parameter  $\alpha = 0.1$ . The corresponding inversions using  $\alpha = 10$  are shown in Figure 4.6. Both results are in good agreement, and further numerical experiments also conclude that the inversion solutions are consistent for a wide ranges of  $\alpha$ .

Next, we consider a more complex density model as illustrated in Figure 4.7. Here, the test model consists of two dipping prisms underground, where the density of the long prism and the short prism are  $1.0\text{g/cm}^3$  and  $0.8\text{g/cm}^3$ , respectively. Figure 4.8 shows the gravity field generated by the density model given in Figure 4.7. Using the perturbed data with adding 2% Gaussian noise directly, the inversion solutions are shown in Figure 4.9. Similar to the previous case study, the inversion scheme is capable of capturing the features for the test case.

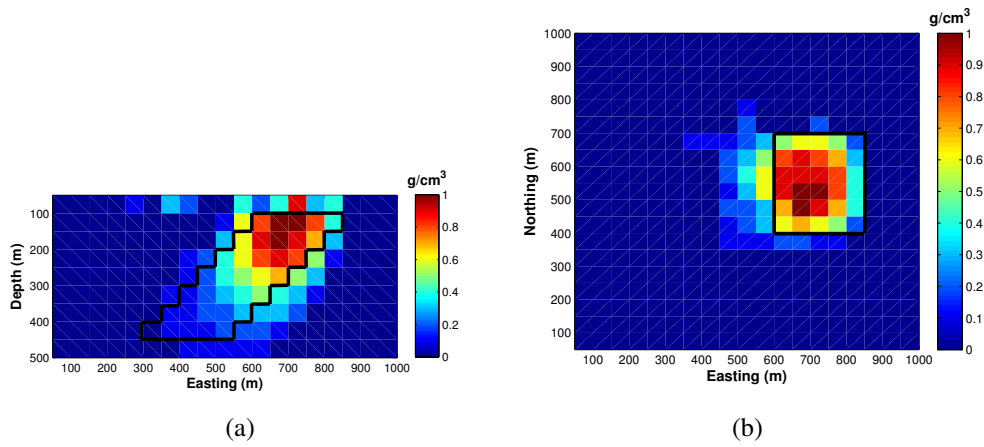


Figure 4.6: Inversion result of gravity field without noise and with 2% Gaussian noise.

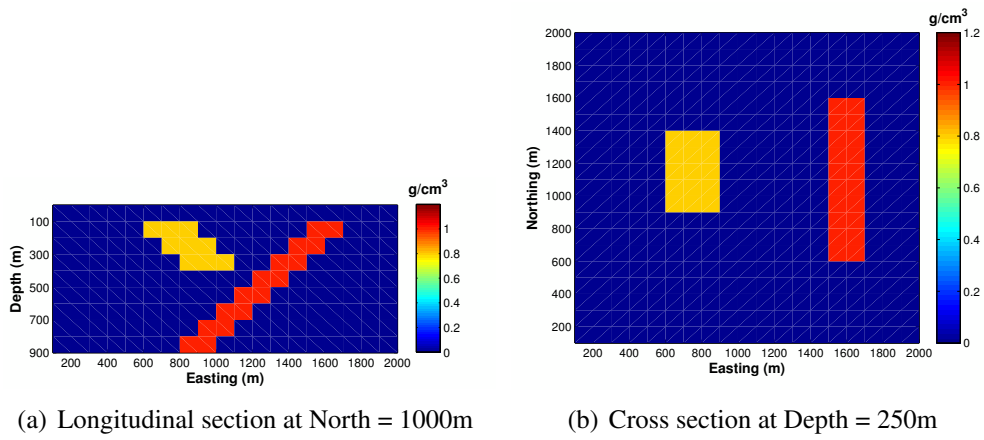


Figure 4.7: Synthetic density model II.

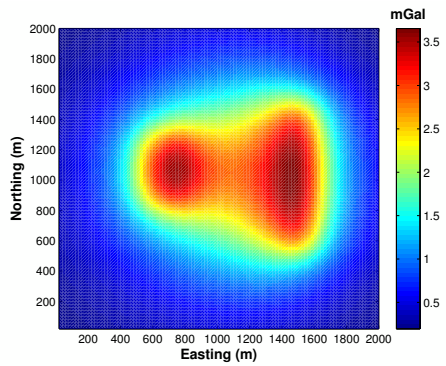


Figure 4.8: Gravity field generated by the synthetic model II.

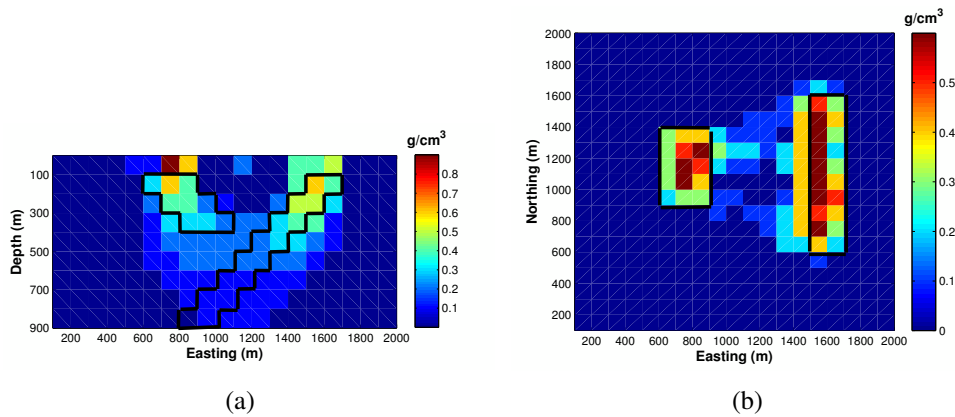


Figure 4.9: Inversion result for gravity field in Figure 4.8 with 2% Gaussian noise.

#### 4.4.2 Field data

In real geophysical applications, the underground structure can be much more complicated than the synthetic models. Figure 4.10 presents a test model using real field data showing a gravity anomaly in a  $5 \times 5$  km area. The interval between each two gridded observations points is 50 m in the north-south and east-west directions, therefore the observation field data is 100 by 100. To infer the underground density structure, we apply the proposed numerical inversion scheme to the 10000 data points. The black lines indicate the position of the inversion results to be investigated.

Figure 4.11 shows the inversion results at three different locations as indicated in Figure 4.10 and with four resolution levels. The details of the inversion resolutions, cell sizes and the corresponding computing time are summarized in in Table 4.1. Obviously, the inversion results are improving as a finer resolution is used. Even though the size of the linear systems grows rapidly as the resolution is increasing,

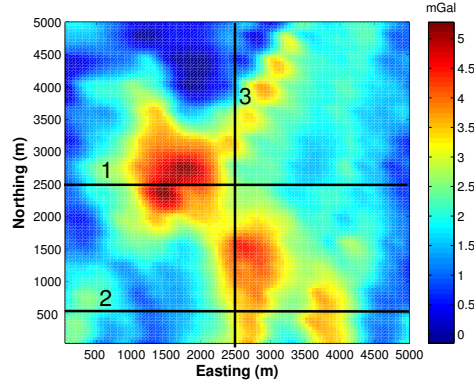


Figure 4.10: Real gravity field data.

it is important to note that the computing time for the numerical inversion increases only linearly. Figure 4.12 displays the computing time required with increasing number of unknowns. With 300,000 unknowns at the finest resolution in R4, the computing time using the proposed scheme is 186.82 seconds for 1000 iterations. However, for a standard iterative scheme without using FFT, the complexity will be  $O(n^2)$  and the estimated computing time using the same computer for 1000 iterations is estimated to be  $5.44 \times 10^7$  seconds. According to the information presented in Figure 4.12, the computing time can be estimated by the following equation:

$$\log(T) = 0.807 * \log(N) - 4.89, \quad (4.4.1)$$

where  $T$  is the computing time, and  $N$  is the number of unknown. According to (4.4.1), when the number of unknown  $N = 10,000,000$  in the recovered model, the estimated computing time is 3352s. It is also important to note that the compact storage requirement is  $O(n)$ , making the proposed BTTB-based schemes capable of inverting large scale data with a very modest computing resource.

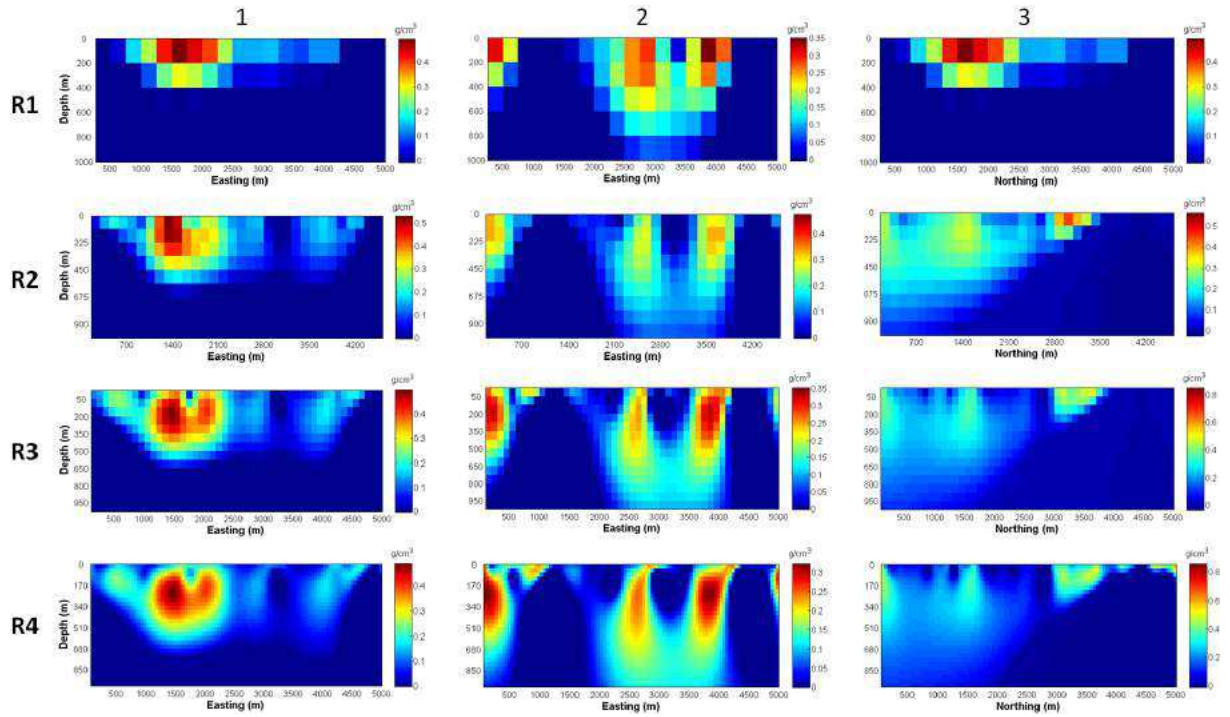


Figure 4.11: Inversion results at location 1, 2 and 3 in Figure 4.10 at four different resolutions.

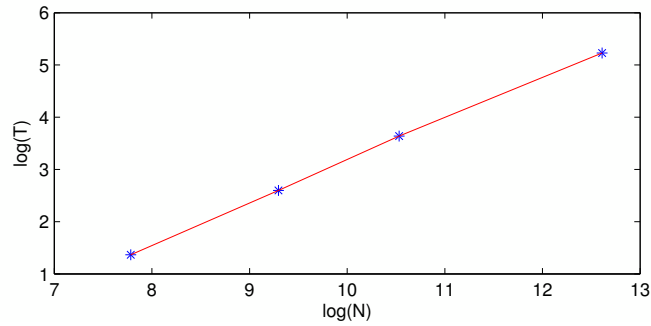


Figure 4.12: The logarithm of the number of unknowns versus the logarithm of the computing time.

Table 4.1: Computing time for inversion of gravity field real data

	Resolution	Cell size (Easting×Northing×Depth)	number of unknowns	number of iteration	$T$ (s)
R1	20×20×6	250m×250m×167m	2400	1000	3.92
R2	33×33×10	152m×152m×100m	10890	1000	13.45
R3	50×50×15	100m×100×67m	37500	1000	38.09
R4	100×100×30	50m×50m×30m	300000	1000	186.82

To address other issues in real field applications, we also investigate the sensitivity on the depth weighting parameter  $\beta$ , and the number of iterations needed. The inversion results presented in Figure 4.11 is based on  $\beta = 1.0$ . Repeating the simulation using  $\beta = 1.4$ , the corresponding result is shown in Figure 4.13, where the side sections are inverted along the direction 1,2 and 3 as indicated in Figure 4.10, and 4 is the inversion result at the cross section at 300 meters deep. In Figure 4.13 - 4, the recovered model contains negative value, which just under the negative point of the field data in Figure 4.10, showing the ability of the proposed positivity constrain to recover a negative model. It is also observed that there exists some discrepancy between the results in Figure 4.11 - R4 and Figure 4.13, however, for  $1.0 \leq \beta \leq 1.5$ , the inversion solutions are generally consistent. Although the inversion results presented in this work is based on the solution after 1000 iterations, the iteration can be terminated early. Figure 4.14 plots the misfit  $e$  versus the iteration number  $N$  for a typical inversion simulation, where  $\mathbf{e} = \Phi_d = \|\mathbf{d} - \mathbf{Tm}\|$ . It is clear that a rapid convergence is achieved and the iteration can be terminated after after a few hundred iterations.

## 4.5 Concluding Remarks

In this chapter, we present a BTTB-based numerical scheme and demonstrate that the proposed method is capable of performing large scale 3D gravity field inversion with a rapid convergence. The success of the new scheme is achieved by utilizing

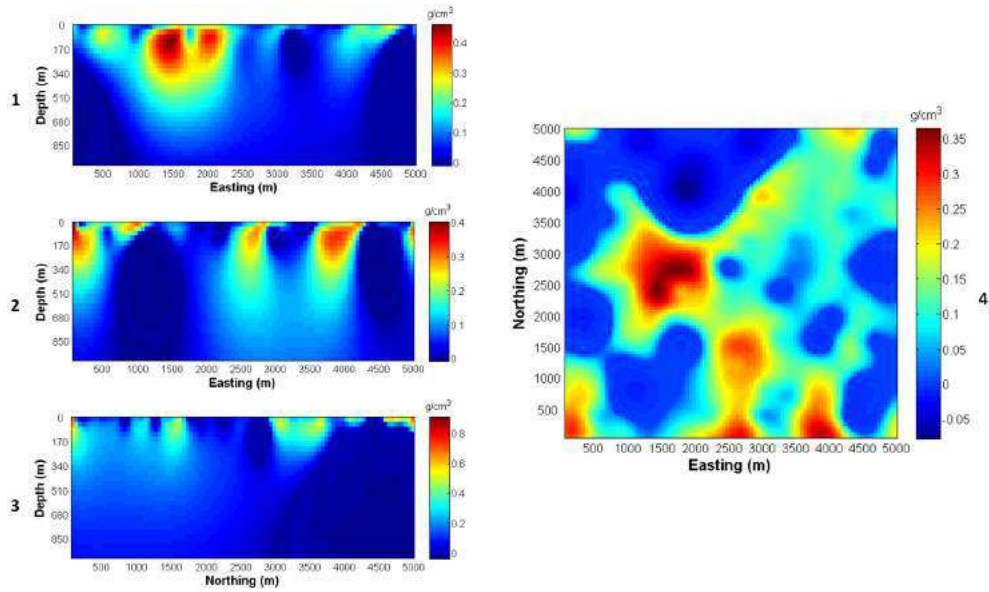


Figure 4.13: Inversion with weighting parameter  $\beta = 1.4$

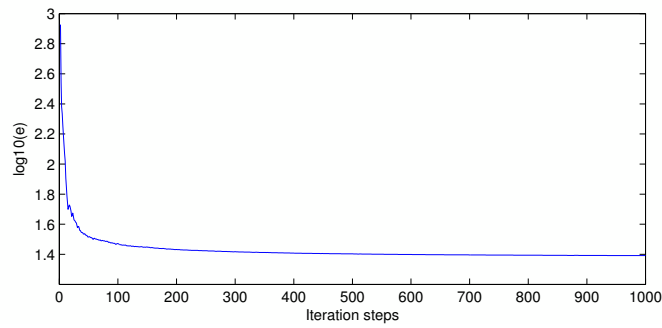


Figure 4.14: Misfit versus the iteration steps.

the properties of the Block-Toeplitz Toeplitz-Block structure. We also prove that it is reasonable to split any 3D gravity field model into a 2D multi-layer model, and the BTTB structure exists in each 2D layer. We further investigate the smoothness and focusing stabilizers under the BTTB framework, such that the convergent rate of the numerical inversion scheme can be rapidly accelerated. The most attractive features of the proposed inversion scheme are that the computation complexity is  $O(n \log n)$  and it requires  $O(n)$  storage. Unlike many existing standard iterative schemes such as that based on the conjugate gradient methods, the computing time for the proposed method depends linearly with the number of unknowns for large scale inversion problems. The new scheme can be regarded as an efficient and powerful tool for 3D large scale inversion and when high resolution is needed.

The proposed scheme has been tested for inversion models using the synthetic and real field data. The effect of the a depth weighting function and positivity constraint function has been investigated. The robustness of the numerical scheme is validated by introducing additional Gaussian noise to the observation data. We have optimized the scheme not only in computing the misfit functional, but also for the regularization stabilizers based on the BTTB framework. Based on the real data simulations, we conclude that large scale inversions can be easily preformed using a laptop with reasonable computing time. The proposed numerical scheme can also be extended for inversions using magnetic field data.

The work reported in this chapter has already been published in Geophysical

Journal International [119].

## Chapter 5

# ADI-FDTD for 2-D Transient Electromagnetic Problems

In the previous chapters, we have investigated the modelling and efficient computation for inverse source problem. In this chapter, we investigate the inverse scattering problem. Using an electromagnetic (EM) method to reconstruct the conductivity distribution, we need to exert artificial magnetic electric field to generate induced field, since the conductivity itself can not generate external fields. Interpretation of electromagnetic data in complex geological environments depends on the multidimensional forward and inverse modeling, and the topic is of great interest to geophysics community. The finite-difference time-domain (FDTD) method first introduced by Yee [115] and Taflove [102] is now generally regarded as one of the most commonly used tools in the EM exploration applications. Oristaglio and Hohmann [76] used the DuFort-Frankel scheme to simulate a 2D transient response to the shut-off of a line source. Lepin [62] extended the FDTD scheme into 3D cases by using the Fourier transform along the strike direction, in which a 2D problem was solved for discrete wavenumbers. Such model is usually referred as

a 2.5D problem, and it performs well for a general 3D structures [99]. Wang and Hohmann [112] extended the FDTD scheme to 3D applications, where the DuFort-Frankel scheme was employed with a staggered-grid. The divergence condition of the magnetic field was imposed and a displacement current term was introduced to ensure the numerical stability. Commer and Newman [21] developed a parallel version for 3D applications. By transforming the Maxwell equation to another form which was less frequency dependent, Maa achieved an efficient implementation of FDTD computation [68]. Other works based on the finite difference including the hybrid finite-difference method and parallel computing were reported in [116] and [97].

In addition to the finite difference (FD) method, the finite volume (FV) and finite element (FE) methods have also been frequently used. The work on FV method covers both the frequency domain [45, 22] and time domain [47]. With the advantage of dealing well with complex geometric domains as well as complicated geologic interfaces, the FE method is very popular in time domain [51, 52] and in frequency domain [53]. Goldman et al [41] applied the FE method in the spatial formulation for the 2D problem and the backward Euler method in the time-domain. Everett and Edwards [34] developed the finite-element time-domain (FETD) method to simulate the marine electromagnetic propagation in 2.5D case. Um et al [110] developed an iterative FETD to investigate the diffusion behavior in 3D earth, where an adaptive time step doubling method was considered to reduce

the computing time. Besides the time domain approach, many work has also been reported in the frequency domain. Without the consideration of time step, it is particularly suitable for applying FE to 2D [61], 2.5D [56] and 3D [86, 109] problems. Recent development on the FE method in EM includes the edge-based FE method [72, 19], multifrontal method [28], adaptive FE method [90, 43], parallel computation [86, 57] and other inversion related problems [92, 42].

However, it is well known that the computing cost associated with FE method is very expensive. It is not a trivial task to generate a proper grid system, the more complex the earth structure is, the more cost there will be needed. Since the resultant matrix in the FE method is frequently ill-conditioned, the solutions may require the use of direct methods [110, 109]. It is worth to note that the computational cost for a direct solver is  $O(N^3)$ , therefore a tremendous amount of storage requirement and computing time are demanded.

Compared with a FETD approach, one attractive advantage of the FDTD algorithm lies in its straightforward implementation. It is feasible to implement an efficient FDTD code with limited computing and storage resource. Further improvements are possible by considering implicit FDTD because of their favorable stability condition as well as computing efficiency, such as ADI-FDTD, Symplectic-FDTD, EC-S-FDTD, etc [37, 73, 101, 22, 38, 18]. With its unconditional stability, the ADI method first introduced by Peaceman Rachford [80] and Douglas [54] could take larger time step than the explicit schemes. Moreover, it is easy to extend

an ADI algorithm from 2D problems to 3D problems.

The storage requirement and computing cost usually depend on the model and the governing equations. Various FDTD formulations have been proposed using diffusion equation [76, 112, 21], Maxwell equations [59, 113, 94] and Helmholtz equation [98, 110, 109]. In this study, we consider a 2D model based on the diffusion equation simulating the electric field. The primary advantage of this choice is that the number of unknowns is much smaller than in other cases. The study of a 2D wave propagation problem is essential, since developing an efficient and accurate solution for a 2.5D model directly depends on the quality of a 2D scheme. Moreover, when implementing a 3D computational code, a 2D scheme can also be extended by adding variables without changing the governing equations.

The major contribution of the presented study are threefold. First, we implement accurate boundary conditions for the earth-air interface and the underground interface. A popular approach to avoid the discretization in the air is to extend one layer into the air [76, 2, 112, 21], and this procedure is known as upward continuation. Here, we imposed an integral equation at the earth-air interface, and this provides an accurate relationship between the normal derivative and horizontal derivative of the electric field. The challenge is how to incorporate the integral equation numerically. Moreover, for the boundary in the earth, the Neumann boundary condition is applied instead of the PEC (i.e. Dirichlet type boundary condition) in order to reduce the reflection error. Secondly we propose the ADI-FDTD scheme

including the treatment of a nonlocal boundary condition, which appears due to the integral boundary condition at the earth-air interface. The stability analysis and convergence order are reported. Finally, as an implicit scheme, numerical example demonstrates that the combined ADI-FDTD algorithm has a competitive advantage over the explicit FDTD in both efficiency and accuracy. This is because the ADI-FDTD is unconditionally stable and allows the use of larger time steps.

This chapter is organized as follows. In Section 5.1, we present the mathematical model for the 2D transient EM (TEM) problem with boundary conditions in the earth-air interface and underground interface. The ADI-FDTD formulation for this model are reported in Section 5.2. Then, Sections 5.3 and 5.4 present the stability analysis and error estimate. The proposed ADI-FDTD scheme is validated, and numerical simulations are reported in Section 5.5.

## 5.1 TEM Model

Consider a 2D transient electromagnetic (TEM) model in the  $x$ - $z$  plane with a rectangular domain  $\Omega = [0, a] \times [0, b]$  as depicted in Figure 5.1, and the time interval is  $[0, T]$ . Under the quasi-stationary assumption of the Maxwell's equations, the TEM model is constructed as the following initial-boundary value (IBV) problem [76]:

$$\mu_0\sigma \frac{\partial E}{\partial t} - \frac{\partial^2 E}{\partial x^2} + \frac{\partial^2 E}{\partial z^2} = -\mu_0 \frac{\partial J_s}{\partial t}, \quad \text{in } \Omega, \quad (5.1.1)$$

$$\frac{\partial E}{\partial n}(x, z = b, t) + \frac{1}{\pi} P \int_{-\infty}^{+\infty} \frac{1}{x - x'} \frac{\partial E}{\partial x'}(x', z = b, t) dx' = 0, \quad \text{on } \Gamma_1, \quad (5.1.2)$$

$$\frac{\partial E}{\partial n} = 0, \quad \text{on } \Gamma_2, \Gamma_3, \Gamma_4, \quad (5.1.3)$$

where  $E$  is the electric field,  $\mu_0$  is the permeability of the free space,  $\sigma = \sigma(x, z)$  is the conductivity distribution,  $J_s$  is the density of the source current in the  $y$ -direction.  $P$  represents a principal value integral and  $n$  is the outward pointing normal direction.

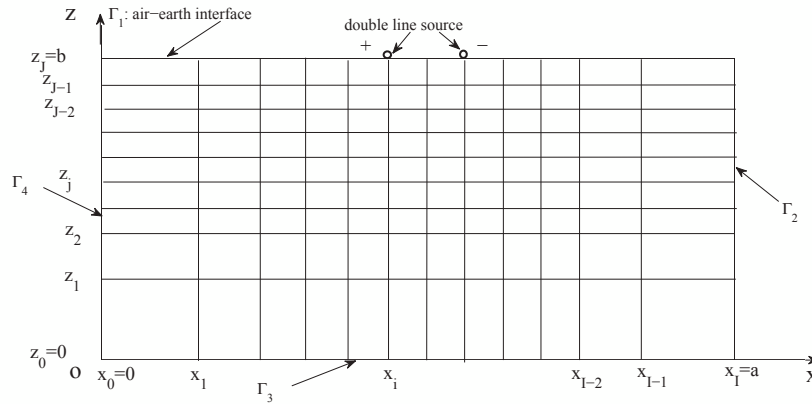


Figure 5.1: Geometry for the 2D TEM problem with the double line source.

The system (5.1.1)-(5.1.3) describes the electric field induced by the variation of the source  $J_s$  in the earth. Since the conductivity  $\sigma$  in the earth is normally much larger than the permittivity  $\epsilon$  so that wavelike features of the electric field vanish very quickly, therefore we consider the diffusion equation (5.1.1) as the governing equation. The upper boundary condition (5.1.2) is derived from the radiation boundary condition, it indicates the relationship to be satisfied for the electric field at the earth-air interface.

For the treatment of the earth-air interface in a 2D TEM modelling, a popular approach is to apply an upward continuation by extending one layer into the air [76,

112]. Moreover, to avoid the reflection error from the Dirichlet boundary condition, the computation domain must be large enough so that the values at the subsurface boundaries to be the analytical solution for a half-space.

In the present study, we handle the earth-air interface by imposing the exact integral boundary condition (5.1.2). In addition, the Dirichlet condition is replaced by a Neumann condition for the boundary in the earth ( $\Gamma_2, \Gamma_3, \Gamma_4$ ) (5.1.3). For the simulation of a sufficiently large domain, this would significantly reduce the reflections from the subsurfaces.

In fact, to avoid the singularity at the early time, the excitation of EM responses from the shut-off of the current source  $J_s$  is generally replaced by imposing the initial conditions on the electric field. Thus, we set  $J_s$  to zero and adding the following initial condition:

$$E(x, z, 0) = E_0(x, z), \quad \text{in } \Omega. \quad (5.1.4)$$

## 5.2 Numerical Formulation for ADI-FDTD with Integral Boundary

In this section, the ADI-FDTD scheme is proposed for the IBV problem (5.1.1)-(5.1.4).

First, let us introduce the partition of the computation domain as displayed in Figure 5.1, where  $x_i, i = 0, 1, \dots, I$ , and  $z_j, j = 0, 1, \dots, J$ , represent the mesh

grids along the  $x$  and  $z$  directions, respectively. Here,  $z_J$  is the earth-air interface. Let  $t^n$  denote the discretization for the time interval  $[0, T]$  and  $\Delta t_n = t^n - t^{n-1}$  be the time step. Also define  $x_{i+\frac{1}{2}} = (x_i + x_{i+1})/2$ ,  $z_{j+\frac{1}{2}} = (z_j + z_{j+1})/2$  and  $t^{n+\frac{1}{2}} = (t^n + t^{n+1})/2$ . Let  $\Delta x_i = x_i - x_{i-1}$ ,  $\Delta z_j = z_j - z_{j-1}$  be the spatial steps in the  $x$  and  $z$  directions. Define the central-difference operators as:

$$\delta_x E_{i,j} = \frac{E_{i+\frac{1}{2},j} - E_{i-\frac{1}{2},j}}{x_{i+\frac{1}{2}} - x_{i-\frac{1}{2}}}, \quad \delta_z E_{i,j} = \frac{E_{i,j+\frac{1}{2}} - E_{i,j-\frac{1}{2}}}{z_{j+\frac{1}{2}} - z_{j-\frac{1}{2}}}, \quad (5.2.1)$$

where  $x_{i+\frac{1}{2}} - x_{i-\frac{1}{2}} = \frac{1}{2}(\Delta x_i + \Delta x_{i+1})$ , and  $z_{j+\frac{1}{2}} - z_{j-\frac{1}{2}} = \frac{1}{2}(\Delta z_j + \Delta z_{j+1})$ .

The proposed ADI-FDTD scheme for the TEM model (5.1.1)-(5.1.4) is constructed as follows:

**Step 1 :** Compute the intermediate variable  $E^{n+\frac{1}{2}}$  using  $E^n$  implicitly in the  $x$  direction and explicitly in the  $z$  direction.

$$\begin{aligned} \mu\sigma_{i,j} \frac{E_{i,j}^{n+\frac{1}{2}} - E_{i,j}^n}{\Delta t_{n+1}/2} &= \delta_x^2 E_{i,j}^{n+\frac{1}{2}} + \delta_z^2 E_{i,j}^n \\ &= \frac{2(E_{i+1,j}^{n+\frac{1}{2}} - E_{i,j}^{n+\frac{1}{2}})}{\Delta x_{i+1}(\Delta x_i + \Delta x_{i+1})} - \frac{2(E_{i,j}^{n+\frac{1}{2}} - E_{i-1,j}^{n+\frac{1}{2}})}{\Delta x_i(\Delta x_i + \Delta x_{i+1})} \\ &\quad + \frac{2(E_{i,j+1}^n - E_{i,j}^n)}{\Delta z_{j+1}(\Delta z_j + \Delta z_{j+1})} - \frac{2(E_{i,j}^n - E_{i,j-1}^n)}{\Delta z_j(\Delta z_j + \Delta z_{j+1})}, \end{aligned} \quad (5.2.2)$$

$$i = 1, \dots, I-1, \quad j = 1, \dots, J-1,$$

with the following boundary conditions for  $\Gamma_2$ ,  $\Gamma_3$  and  $\Gamma_4$ :

$$E_{i,0}^{n+\frac{1}{2}} = E_{i,1}^{n+\frac{1}{2}}, \quad E_{0,j}^{n+\frac{1}{2}} = E_{1,j}^{n+\frac{1}{2}}, \quad E_{I,j}^{n+\frac{1}{2}} = E_{I-1,j}^{n+\frac{1}{2}}. \quad (5.2.3)$$

It is necessary to note that in the first step, there is no need to compute the values

of the intermediate variable  $E^{n+\frac{1}{2}}$  on the upper boundary  $\Gamma_1$  since they would not be used in the second-step calculation.

To clarify the computing procedure of this step, the scheme (5.2.2) is rearranged as:

$$\begin{aligned}
& \left(1 + \frac{\Delta t_{n+1}}{\mu\sigma_{i,j}\Delta x_i(\Delta x_i + \Delta x_{i+1})} + \frac{\Delta t_{n+1}}{\mu\sigma_{i,j}\Delta x_{i+1}(\Delta x_i + \Delta x_{i+1})}\right) E_{i,j}^{n+\frac{1}{2}} \\
& \quad - \frac{\Delta t_{n+1}}{\mu\sigma_{i,j}\Delta x_i(\Delta x_i + \Delta x_{i+1})} E_{i-1,j}^{n+\frac{1}{2}} - \frac{\Delta t_{n+1}}{\mu\sigma_{i,j}\Delta x_{i+1}(\Delta x_i + \Delta x_{i+1})} E_{i+1,j}^{n+\frac{1}{2}} = \\
& \left(1 - \frac{\Delta t_{n+1}}{\mu\sigma_{i,j}\Delta z_j(\Delta z_j + \Delta z_{j+1})} - \frac{\Delta t_{n+1}}{\mu\sigma_{i,j}\Delta z_{j+1}(\Delta z_j + \Delta z_{j+1})}\right) E_{i,j}^n \\
& \quad + \frac{\Delta t_{n+1}}{\mu\sigma_{i,j}\Delta z_j(\Delta z_j + \Delta z_{j+1})} E_{i,j-1}^n + \frac{\Delta t_{n+1}}{\mu\sigma_{i,j}\Delta z_{j+1}(\Delta z_j + \Delta z_{j+1})} E_{i,j+1}^n.
\end{aligned} \tag{5.2.4}$$

For a given index  $j$  ( $j = 1, \dots, J-1$ ) in the  $z$  direction, (5.2.4) and (5.2.3) lead to a tridiagonal linear system which could be computed effectively by the Thomas' algorithm with a cost of  $O(I)$  [103].

**Step 2 :** Compute  $E^{n+1}$  using  $E^{n+\frac{1}{2}}$  explicitly in the  $x$  direction and implicitly in the  $z$  direction.

$$\begin{aligned}
\mu\sigma_{i,j} \frac{E_{i,j}^{n+1} - E_{i,j}^{n+\frac{1}{2}}}{\Delta t_{n+1}/2} &= \delta_x^2 E_{i,j}^{n+\frac{1}{2}} + \delta_z^2 E_{i,j}^{n+1} \\
&= \frac{2(E_{i+1,j}^{n+\frac{1}{2}} - E_{i,j}^{n+\frac{1}{2}})}{\Delta x_{i+1}(\Delta x_i + \Delta x_{i+1})} - \frac{2(E_{i,j}^{n+\frac{1}{2}} - E_{i-1,j}^{n+\frac{1}{2}})}{\Delta x_i(\Delta x_i + \Delta x_{i+1})} \\
& \quad + \frac{2(E_{i,j+1}^{n+1} - E_{i,j}^{n+1})}{\Delta z_{j+1}(\Delta z_j + \Delta z_{j+1})} - \frac{2(E_{i,j}^{n+1} - E_{i,j-1}^{n+1})}{\Delta z_j(\Delta z_j + \Delta z_{j+1})},
\end{aligned} \tag{5.2.5}$$

$$i = 1, \dots, I-1, \quad j = 1, \dots, J-1,$$

with the boundary conditions for  $\Gamma_2$ ,  $\Gamma_3$  and  $\Gamma_4$ :

$$E_{i,0}^{n+1} = E_{i,1}^{n+1}, \quad E_{0,j}^{n+1} = E_{1,j}^{n+1}, \quad E_{I,j}^{n+1} = E_{I-1,j}^{n+1}. \quad (5.2.6)$$

The numerical scheme for the upper boundary  $\Gamma_1$  is given by (we will elaborate on this shortly):

$$\frac{3E_{i,J}^{n+1} - 4E_{i,J-1}^{n+1} + E_{i,J-2}^{n+1}}{2\Delta z_J} + \frac{1}{\pi} \sum_{k=1}^{I-2} \frac{E_{k+1,J}^{n+1} - E_{k,J}^{n+1}}{x_i - x_{k+\frac{1}{2}}} = 0. \quad (5.2.7)$$

Scheme (5.2.5) can be rewritten as

$$\begin{aligned} & \left(1 + \frac{\Delta t_{n+1}}{\mu\sigma_{i,j}\Delta z_j(\Delta z_j + \Delta z_{j+1})} + \frac{\Delta t_{n+1}}{\mu\sigma_{i,j}\Delta z_{j+1}(\Delta z_j + \Delta z_{j+1})}\right) E_{i,j}^{n+1} \\ & - \frac{\Delta t_{n+1}}{\mu\sigma_{i,j}\Delta z_j(\Delta z_j + \Delta z_{j+1})} E_{i,j-1}^{n+1} - \frac{\Delta t_{n+1}}{\mu\sigma_{i,j}\Delta z_{j+1}(\Delta z_j + \Delta z_{j+1})} E_{i,j+1}^{n+1} = \\ & \left(1 - \frac{\Delta t_{n+1}}{\mu\sigma_{i,j}\Delta x_i(\Delta x_i + \Delta x_{i+1})} - \frac{\Delta t_{n+1}}{\mu\sigma_{i,j}\Delta x_{i+1}(\Delta x_i + \Delta x_{i+1})}\right) E_{i,j}^{n+\frac{1}{2}} \\ & + \frac{\Delta t_{n+1}}{\mu\sigma_{i,j}\Delta x_i(\Delta x_i + \Delta x_{i+1})} E_{i-1,j}^{n+\frac{1}{2}} + \frac{\Delta t_{n+1}}{\mu\sigma_{i,j}\Delta x_{i+1}(\Delta x_i + \Delta x_{i+1})} E_{i+1,j}^{n+\frac{1}{2}}. \end{aligned} \quad (5.2.8)$$

For a given index  $i$  ( $i = 1, \dots, I - 1$ ) in the  $x$  direction, a tridiagonal linear system could be constructed by (5.2.8), (5.2.6) and (5.2.7).

For simplicity, we use homogeneous mesh grids and time steps, that is  $\Delta x = \Delta z = h$ ,  $\Delta t = T/N$ .

### Treatment of the integral boundary condition (5.1.2)

In the second step of the ADI-FDTD scheme, the electric field at the earth-air interface  $E_{i,j}^{n+1}$  ( $i = 0, \dots, I$ ) must be known in order to make the linear tridiago-

nal system solvable. This can be achieved by discretizing the boundary condition (5.1.2) using numerical differential and integral. We approximate the derivative term  $\frac{\partial E}{\partial n}$  by:

$$\frac{\partial E^{n+1}}{\partial n} \Big|_{i,J} \doteq \frac{3E_{i,J}^{n+1} - 4E_{i,J-1}^{n+1} + E_{i,J-2}^{n+1}}{2h}, \quad (5.2.9)$$

which is of second-order accurate. For the integral term, we employ the following discretization:

$$\begin{aligned} P \int_{-\infty}^{+\infty} \frac{1}{x-x'} \frac{\partial E}{\partial x'}(x', z=b, t^{n+1}) dx' &\doteq \sum_{k=1}^{I-2} \frac{\delta_x E_{k+\frac{1}{2},J}^{n+1}}{x_i - x_{k+\frac{1}{2}}} h \\ &= \sum_{k=1}^{I-2} \frac{E_{k+1,J}^{n+1} - E_{k,J}^{n+1}}{x_i - x_{k+\frac{1}{2}}}, \quad i = 1, \dots, I-1. \end{aligned} \quad (5.2.10)$$

Substituting (5.2.9) and (5.2.10) into (5.1.2), it leads to (5.2.7). Note that (5.2.7)

can be rewritten as

$$\begin{aligned} \frac{3}{2}E_{i,J}^{n+1} - \frac{E_{1,J}^{n+1}}{\pi(i-3/2)} + \frac{E_{I-1,J}^{n+1}}{\pi(i-I+3/2)} + \frac{1}{\pi} \sum_{k=2}^{I-2} \left( \frac{1}{i-k+1/2} - \frac{1}{i-k-1/2} \right) E_{k,J}^{n+1} \\ = \frac{4E_{i,J-1}^{n+1} - E_{i,J-2}^{n+1}}{2}, \quad i = 1, \dots, I-1. \end{aligned} \quad (5.2.11)$$

From (5.2.11), it is clear that the values of  $E^{n+1}$  at the earth-air interface, i.e.

$E_{1:I-1,J}^{n+1}$ , can be computed by solving the following linear system:

$$AE_{1:I-1,J}^{n+1} = BE_{1:I-1,J-1}^{n+1} + CE_{1:I-1,J-2}^{n+1}, \quad (5.2.12)$$

where  $B = \text{diag}(2)$ ,  $C = \text{diag}(-\frac{1}{2})$ . And the matrix  $A$  is given by

$$A_{(I-1) \times (I-1)} =$$

$$\begin{pmatrix} \frac{3}{2} + \frac{2}{\pi} & \frac{2}{\pi}(\frac{1}{3} - 1) & \frac{2}{\pi}(\frac{1}{5} - \frac{1}{3}) & \cdots & \frac{2}{\pi}(\frac{1}{2I-5} - \frac{1}{2I-7}) & -\frac{2}{\pi} \frac{1}{(2I-5)} \\ -\frac{2}{\pi} & \frac{3}{2} + \frac{4}{\pi} & \frac{2}{\pi}(\frac{1}{3} - 1) & \cdots & \frac{2}{\pi}(\frac{1}{2I-7} - \frac{1}{2I-9}) & -\frac{2}{\pi} \frac{1}{(2I-7)} \\ -\frac{2}{\pi} \frac{1}{3} & \frac{2}{\pi}(\frac{1}{3} - 1) & \frac{3}{2} + \frac{4}{\pi} & \cdots & \frac{2}{\pi}(\frac{1}{2I-9} - \frac{1}{2I-11}) & -\frac{2}{\pi} \frac{1}{(2I-9)} \\ \vdots & \vdots & \vdots & \cdots & \vdots & \vdots \\ -\frac{2}{\pi} \frac{1}{(2I-7)} & \frac{2}{\pi}(\frac{1}{2I-7} - \frac{1}{2I-9}) & \frac{2}{\pi}(\frac{1}{2I-9} - \frac{1}{2I-11}) & \cdots & \frac{3}{2} + \frac{4}{\pi} & -\frac{2}{\pi} \\ -\frac{2}{\pi} \frac{1}{(2I-5)} & \frac{2}{\pi}(\frac{1}{2I-5} - \frac{1}{2I-7}) & \frac{2}{\pi}(\frac{1}{2I-7} - \frac{1}{2I-9}) & \cdots & \frac{2}{\pi}(\frac{1}{3} - 1) & \frac{3}{2} + \frac{2}{\pi} \end{pmatrix}$$

$$= \begin{pmatrix} \beta(1) & \alpha^T & \beta_1(1) \\ \beta(2 : I-2) & A_0 & \beta_1(2 : I-2) \\ \beta(I-1) & \alpha_1^T & \beta_1(I-1) \end{pmatrix},$$

(5.2.13)

where

$$\begin{aligned}
\beta &= A(1 : I - 1, 1) = \left( \frac{3}{2} + \frac{2}{\pi}, -\frac{2}{\pi}, \dots, -\frac{2}{\pi} \frac{1}{(2I - 5)} \right)^T, \\
\beta_1 &= A(1 : I - 1, I - 1) = \left( -\frac{2}{\pi} \frac{1}{(2I - 5)}, -\frac{2}{\pi} \frac{1}{(2I - 7)}, \dots, \frac{3}{2} + \frac{2}{\pi} \right)^T, \\
\alpha &= A(1, 2 : I - 2)^T = \left( \frac{2}{\pi} \left( \frac{1}{3} - 1 \right), \frac{2}{\pi} \left( \frac{1}{5} - \frac{1}{3} \right), \dots, \frac{2}{\pi} \left( \frac{1}{2I - 5} - \frac{1}{2I - 7} \right) \right)^T, \\
\alpha_1 &= A(I - 1, 2 : I - 2)^T = \left( \frac{2}{\pi} \left( \frac{1}{2I - 5} - \frac{1}{2I - 7} \right), \frac{2}{\pi} \left( \frac{1}{2I - 7} - \frac{1}{2I - 9} \right), \dots, \frac{2}{\pi} \left( \frac{1}{3} - 1 \right) \right)^T.
\end{aligned} \tag{5.2.14}$$

It is obvious that  $A_0$  is an  $(I - 3) \times (I - 3)$  symmetric matrix.

However, with the unknowns  $E_{1:I-1, J-1}^{n+1}$  and  $E_{1:I-1, J-2}^{n+1}$  in (5.2.12), it is impossible to compute  $E_{1:I-1, J}^{n+1}$ . To resolve the problem, we eliminate  $E_{1:I-1, J-1}^{n+1}$  and  $E_{1:I-1, J-2}^{n+1}$  using (5.2.5).

First, let us express the system (5.2.5) in a matrix form, for each  $i$  from 1 to  $I - 1$ , we have

$$PE_{i,1:J}^{n+1} = F, \tag{5.2.15}$$

with

$$P = \begin{pmatrix} -a & 1+a & 0 & 0 & \dots & 0 & 0 \\ -a & 1+2a & -a & 0 & \dots & 0 & 0 \\ \vdots & \vdots & \vdots & \vdots & & \vdots & \vdots \\ 0 & 0 & \dots & -a & 1+2a & -a & 0 \\ 0 & 0 & \dots & 0 & -a & 1+2a & -a \end{pmatrix}_{(J-1) \times (J)} \tag{5.2.16}$$

where  $a = \frac{\Delta t}{2\mu\sigma h^2}$ ,  $F$  represents the RHS of this linear system.

Now, a downward recursion algorithm could be applied to the tridiagonal system (5.2.15) eliminating the lower diagonal and yielding the diagonal element to be unity (upper triangularization). The last two equations in the system are given by

$$E_{i,J-1}^{n+1} = p_{i,1}^{n+1} E_{i,J}^{n+1} + q_{i,1}^{n+1}, \quad (5.2.17)$$

$$E_{i,J-2}^{n+1} = p_{i,2}^{n+1} E_{i,J-1}^{n+1} + q_{i,2}^{n+1}.$$

Substituting the first equation of (5.2.17) into the second one, we obtain

$$E_{i,J-2}^{n+1} = p_{i,1}^{n+1} p_{i,2}^{n+1} E_{i,J}^{n+1} + p_{i,2}^{n+1} q_{i,1}^{n+1} + q_{i,2}^{n+1}. \quad (5.2.18)$$

Using (5.2.17) and (5.2.18), we could replace  $E_{1:I-1,J-1}^{n+1}$  and  $E_{1:I-1,J-2}^{n+1}$  in (5.2.12) to complete the linear system with respect to  $E_{1:I-1,J}^{n+1}$  and solve it by a linear solver. With the values of  $E_{1:I-1,J}^{n+1}$ , the second step of the ADI-FDTD scheme can be implemented.

**Remark 1.** *The proposed ADI-FDTD scheme is easy and efficient to implement. For the integral boundary condition (5.1.2), there is only one extra linear system to compute in each iteration besides a sequence of tridiagonal linear systems. However, the extra cost is negligible since there are many fast solvers. In addition, in each substep, the original 2D problem is transformed to a series of 1D problems with tridiagonal linear systems.*

### 5.3 Stability analysis of ADI-FDTD in $L^2$ norm

Now, we analyze the stability of the proposed ADI-FDTD scheme for the model (5.1.1)-(5.1.4)<sup>1</sup>. Firstly, define the following discrete  $L^2$  norms and the corresponding inner product:

$$\begin{aligned}
 \|E^n\|^2 &= \sum_{j=1}^{J-1} \sum_{i=1}^{I-1} E_{i,j}^{n2} h^2, & \|\delta_x E^n\|^2 &= \sum_{j=1}^{J-1} \sum_{i=0}^{I-1} (\delta_x E_{i+\frac{1}{2},j}^n)^2 h^2, \\
 \|\delta_z E^n\|^2 &= \sum_{j=0}^{J-1} \sum_{i=1}^{I-1} (\delta_z E_{i,j+\frac{1}{2}}^n)^2 h^2, & \|\delta_x \delta_z E^n\|^2 &= \sum_{j=0}^{J-1} \sum_{i=0}^{I-1} (\delta_x \delta_z E_{i+\frac{1}{2},j+\frac{1}{2}}^n)^2 h^2, \\
 (U, V) &= \sum_{j=1}^{J-1} \sum_{i=1}^{I-1} U_{i,j} V_{i,j} h^2,
 \end{aligned} \tag{5.3.1}$$

and

$$\begin{aligned}
 \|E^n\|_{\Gamma_1}^2 &= \sum_{i=1}^{I-1} E_{i,J}^{n2} \frac{h^2}{2}, & \|E^n\|_{\Gamma_2}^2 &= \sum_{j=1}^{J-1} E_{I,j}^{n2} \frac{h^2}{2}, \\
 \|E^n\|_{\Gamma_3}^2 &= \sum_{i=1}^{I-1} E_{i,0}^{n2} \frac{h^2}{2}, & \|E^n\|_{\Gamma_4}^2 &= \sum_{j=1}^{J-1} E_{0,j}^{n2} \frac{h^2}{2},
 \end{aligned} \tag{5.3.2}$$

where  $\Gamma_1$  refers to the earth-air interface,  $\Gamma_2$ ,  $\Gamma_3$  and  $\Gamma_4$  are the three subsurfaces counterclockwise as shown in Figure 5.1.

The discrete  $L^2$  norm of  $E$  in the inner domain without boundaries is defined by (5.3.1), and (5.3.2) gives the discrete  $L^2$  norm of  $E$  on the four boundaries respectively. By estimating the discrete energy of this system, we will analyze the stability of the ADI-FDTD algorithm.

---

<sup>1</sup>The main work in theoretical analysis of stability is conducted by Dr. Wanshan Li

Eliminating the intermediate variables  $E^{n+\frac{1}{2}}$  from the schemes (5.2.2) and (5.2.5), it is not hard to verify that the ADI scheme is equivalent to the following scheme for all the inner points:

$$\begin{aligned} \frac{E_{i,j}^{n+1} - E_{i,j}^n}{\Delta t} - \frac{1}{2\mu\sigma}(\delta_x^2 + \delta_z^2)(E^n + E^{n+1})_{i,j} + \frac{\Delta t}{4\mu^2\sigma^2}\delta_x^2\delta_z^2(E^{n+1} - E^n)_{i,j} = 0, \\ i = 1, \dots, I-1, \quad j = 1, \dots, J-1. \end{aligned} \quad (5.3.3)$$

Multiplying  $(E^n + E^{n+1})_{i,j}$  to both sides of (5.3.3), computing the inner product and denoting the three items on the left hand side as  $I_1$ ,  $I_2$  and  $I_3$ , respectively, it follows that with the definition in (5.3.1),

$$\begin{aligned} I_1 &= \left( \frac{E^{n+1} - E^n}{\Delta t}, (E^n + E^{n+1}) \right) = \frac{1}{\Delta t} (\|E^{n+1}\|^2 - \|E^n\|^2), \\ I_2 &= -\frac{1}{2\mu\sigma} \left( (\delta_x^2 + \delta_z^2)(E^n + E^{n+1}), (E^n + E^{n+1}) \right), \\ I_3 &= \frac{\Delta t}{4\mu^2\sigma^2} \left( \delta_x^2\delta_z^2(E^{n+1} - E^n), (E^n + E^{n+1}) \right). \end{aligned} \quad (5.3.4)$$

Using the discrete Green formula and imposing the Neumann boundary conditions on the subsurface  $\Gamma_2$ ,  $\Gamma_3$  and  $\Gamma_4$  (5.2.6), for the  $\delta_x^2$  and  $\delta_z^2$  terms in  $I_2$ , we deduce respectively, that

$$I_{2_1} = -\frac{1}{2\mu\sigma} \left( \delta_x^2(E^n + E^{n+1}), (E^n + E^{n+1}) \right) = \frac{1}{2\mu\sigma} \|\delta_x(E^n + E^{n+1})\|^2, \quad (5.3.5)$$

$$\begin{aligned}
I_{2_2} &= -\frac{1}{2\mu\sigma} \left( \delta_z^2(E^n + E^{n+1}), (E^n + E^{n+1}) \right) \\
&= \frac{1}{2\mu\sigma} \left\{ \|\delta_z(E^n + E^{n+1})\|^2 - \sum_{i=1}^{I-1} [(E^n + E^{n+1})_{i,J} - (E^n + E^{n+1})_{i,J-1}] \right. \\
&\quad \left. \times (E^n + E^{n+1})_{i,J} \right\}.
\end{aligned} \tag{5.3.6}$$

In fact, the boundary schemes on subsurfaces  $\Gamma_2$ – $\Gamma_4$  (5.2.6) imply the following relationship:

$$\begin{aligned}
\delta_z E_{0,j+\frac{1}{2}}^n &= \delta_z E_{1,j+\frac{1}{2}}^n, \quad \delta_z E_{I,j+\frac{1}{2}}^n = \delta_z E_{I-1,j+\frac{1}{2}}^n, \quad j = 0, \dots, J-1, \\
\delta_x E_{i+\frac{1}{2},0}^n &= \delta_x E_{i+\frac{1}{2},1}^n, \quad i = 0, \dots, I-1.
\end{aligned} \tag{5.3.7}$$

By the discrete Green formula and (5.3.7), for  $I_3$ , we derive

$$\begin{aligned}
I_3 &= \frac{\Delta t}{4\mu^2\sigma^2} \sum_{j=1}^{J-1} \sum_{i=1}^{I-1} \delta_x^2 \delta_z^2 (E^{n+1} - E^n)_{i,j} (E^{n+1} + E^n)_{i,j} h^2 \\
&= \frac{\Delta t}{4\mu^2\sigma^2} \left\{ \|\delta_x \delta_z E^{n+1}\|^2 - \|\delta_x \delta_z E^n\|^2 \right. \\
&\quad \left. - \sum_{i=0}^{I-1} [\delta_x (E^{n+1} - E^n)_{i+\frac{1}{2},J} - \delta_x (E^{n+1} - E^n)_{i+\frac{1}{2},J-1}] \times \delta_x (E^n + E^{n+1})_{i+\frac{1}{2},J} \right\}.
\end{aligned} \tag{5.3.8}$$

The last terms in the RHS of (5.3.6) and (5.3.8) need to be dealt with carefully, since they involve the values of  $E$  at the earth-air interface.

Firstly, we introduce the following lemma.

**Lemma 1.** *Assume that  $E(x, z, t)$  is the exact solution of the IBV problem (5.1.1)–(5.1.4), which is of sufficient smoothness, and  $E_{i,j}^n$  is the numerical solution of the ADI-FDTD scheme (5.2.2)–(5.2.6). Then there exists a constant  $\bar{C}$  independent of*

$\Delta t$  and  $h$ , such that

$$\|E^n\|_{\Gamma_1}^2 \leq \bar{C} \sum_{i=1}^{I-1} (E_{i,J-1}^{n^2} + E_{i,J-2}^{n^2}) h^2. \quad (5.3.9)$$

*Proof.* Taking the inner product of  $E_{1:I-1,J}$  with both sides of (5.2.12) at the  $n$ -th time level, and considering the left-hand side  $E_{1:I-1,J}^{n^T} A E_{1:I-1,J}^n$  ( $A$  is of the form (5.2.13)), we have

$$\begin{aligned} & E_{1:I-1,J}^{n^T} A E_{1:I-1,J}^n \\ &= E_{2:I-2,J}^{n^T} A_0 E_{2:I-2,J}^n + E_{1:I-1,J}^{n^T} \beta E_{1,J}^n + E_{1:I-1,J}^{n^T} \beta_1 E_{I-1,J}^n \\ & \quad + \sum_{k=2}^{I-2} E_{1,J}^n \alpha(k-1) E_{k,J}^n + \sum_{k=2}^{I-2} E_{I-1,J}^n \alpha_1(k-1) E_{k,J}^n \\ &= E_{2:I-2,J}^{n^T} A_0 E_{2:I-2,J}^n + \beta(1)(E_{I-1,J}^{n^2} + E_{1,J}^{n^2}) + 2\beta(I-1)E_{1,J}^n E_{I-1,J}^n \\ & \quad + \sum_{k=2}^{I-2} (\alpha(I-k-1) + \beta(I-k)) E_{k,J}^n E_{I-1,J}^n \\ & \quad + \sum_{k=2}^{I-2} (\alpha(k-1) + \beta(k)) E_{k,J}^n E_{1,J}^n. \end{aligned} \quad (5.3.10)$$

Note that  $A_0$  is a symmetric and strictly diagonal-dominant matrix, thus  $A_0$  is positive-definite and we can estimate its eigenvalues, that is,

$$\left(\frac{3}{2} + \frac{4}{\pi(I-3)}\right) \leq \lambda(A_0) \leq \left(\frac{3}{2} + \frac{8}{\pi}\right). \quad (5.3.11)$$

In addition, by applying the Cauchy-Schwartz inequality, monotonic decreasing

and convergence of some series, we conclude that the bound of  $\|E^n\|_{\Gamma_1}^2$  is given by:

$$\|E^n\|_{\Gamma_1}^2 = \sum_{k=1}^{I-1} E_{k,J}^{n^2} \frac{h^2}{2} \leq M_1 \sum_{k=1}^{I-1} E_{k,J-1}^{n^2} \frac{h^2}{2} + M_2 \sum_{k=1}^{I-1} E_{k,J-2}^{n^2} \frac{h^2}{2},$$

where

$$M_1 = 1/\left(\frac{3C_1}{2} - C_1^2 - \frac{C_1 C_2}{4} + \frac{4C_1}{\pi(I-3)} - \frac{50C_0 C_1}{9\pi}\right),$$

$$M_2 = 1/\left(6C_2 - 4C_1 C_2 - C_2^2 + \frac{16C_2}{\pi(I-3)} - \frac{200C_0 C_2}{9\pi}\right),$$

$C_1, C_2$  are some positive constants independent of  $\Delta t$  and  $h$ .

(5.3.12)

Therefore, it confirms (5.3.9) with  $\bar{C} = \max\{\frac{M_1}{2}, \frac{M_2}{2}\}$ .  $\square$

**Remark 2.** Lemma 1 reflects that the energy on the boundaries could be bounded by the inner energy, that is,

$$\|E^n\|_{\Gamma_1}^2 \leq \bar{C} \|E^n\|^2. \quad (5.3.13)$$

Using Lemma 1, we can treat the last terms in the RHS of  $I_{2_2}$  and  $I_3$  to present the following result,

$$\begin{aligned} & \|E^{n+1}\|^2 + \frac{\Delta t^2}{4\mu^2\sigma^2} \|\delta_x \delta_z E^{n+1}\|^2 \\ & \leq \|E^n\|^2 + \frac{\Delta t^2}{4\mu^2\sigma^2} \|\delta_x \delta_z E^n\|^2 + \left(\frac{\Delta t M}{2\mu\sigma h^2} + \frac{\Delta t^2 M}{\mu^2\sigma^2 h^4}\right) (\|E^n\|^2 + \|E^{n+1}\|^2), \end{aligned} \quad (5.3.14)$$

where  $M = \max(3M_1 + 1, 3M_2)$ .

Summing  $n$  for both sides of (5.3.14), we obtain

$$\begin{aligned} & \|E^n\|^2 + \frac{\Delta t^2}{4\mu^2\sigma^2} \|\delta_x\delta_z E^n\|^2 \\ & \leq \|E^0\|^2 + \frac{\Delta t^2}{4\mu^2\sigma^2} \|\delta_x\delta_z E^0\|^2 + 2\Delta t \left( \frac{M}{2\mu\sigma h^2} + \frac{\Delta t M}{\mu^2\sigma^2 h^4} \right) \sum_{k=0}^n \|E^k\|^2. \end{aligned} \quad (5.3.15)$$

By the Gronwall inequality [44], it implies that:

$$\max_{n \leq [T/\Delta t]} \|E^n\|^2 \leq e^{\left( \frac{M}{\mu\sigma h^2} + \frac{2\Delta t M}{\mu^2\sigma^2 h^4} \right) T} \|E^0\|^2. \quad (5.3.16)$$

In a typical TEM problem, the spatial step  $h$  is frequently taken as no less than 10 due to the large scale of the computational domain ( $10^3 - 10^4$ ), but the time step  $\Delta t$  is  $O(10^{-6})$ . The total simulation time for receiving the EM response is generally of the  $10^{-3}$  order, thus the exponential term  $e^{\left( \frac{M}{\mu\sigma h^2} + \frac{2\Delta t M}{\mu^2\sigma^2 h^4} \right) T}$  could be bounded by some constant. We now derive the stability conclusion of the TEM problem as follows.

**Theorem 3.** (Stability) Assume that  $E(x, z, t)$  is the exact solution of the equation (5.1.1)-(5.1.4) and is of sufficient smoothness. Let  $E_{i,j}^n$  be the numerical solution of the ADI scheme (5.2.2)-(5.2.6), with the definition of discrete  $L^2$  norm, there exists a positive constant  $K$ , such that

$$\max_{n \leq [T/\Delta t]} \|E^n\|^2 \leq e^{KT} \|E^0\|^2. \quad (5.3.17)$$

## 5.4 Convergence analysis of ADI-FDTD

We now analyze the convergence of the proposed algorithm by the energy method.<sup>1</sup>

First, let the error define by,

$$\xi_{i,j}^n = E(x_i, z_j, t^n) - E_{i,j}^n, \quad i = 0, \dots, I, \quad j = 0, \dots, J. \quad (5.4.1)$$

For the truncation error at all interior and boundary grids, we have the following

Lemma.

**Lemma 2.** *Assume that  $E(x, z, t)$  is the exact solution of the IBV problem (5.1.1)-(5.1.4) and is of sufficient smoothness. Let  $E_{i,j}^n$  be the numerical solution of the ADI-FDTD scheme (5.2.2)-(5.2.6), it holds that*

$$\begin{aligned} \max_{i=1, \dots, I-1, j=1, \dots, J-1} \{|R_{i,j}^{n+\frac{1}{2}}|\} &\leq O(\Delta t^2 + h^2), \\ \max_{j=0, \dots, J} \{|\xi_{0,j}^n|, |\xi_{I,j}^n|\} &\leq O(\Delta t^2 + h^2), \\ \max_{i=1, \dots, I-1} \{|\xi_{i,0}^n|, |\tilde{R}_{i,J}^n|\} &\leq O(\Delta t^2 + h^2), \end{aligned} \quad (5.4.2)$$

where  $R_{i,j}^{n+\frac{1}{2}}$  denotes the truncation error for the interior points,  $\xi_{I,j}^n$ ,  $\xi_{i,0}^n$ ,  $\xi_{0,j}^n$  represent the truncation errors on the three subsurfaces  $\Gamma_2 - \Gamma_4$ , respectively and  $\tilde{R}_{i,J}^n$  is the truncation error at the earth-air interface  $\Gamma_1$ .

*Proof.* For the interior points, from the inner equivalent scheme (5.3.3), we derive

---

<sup>1</sup>The main work in theoretical analysis of convergence is conducted by Dr. Wanshan Li

the error equation:

$$\begin{aligned} \frac{\xi_{i,j}^{n+1} - \xi_{i,j}^n}{\Delta t} - \frac{1}{2\mu\sigma}(\delta_x^2 + \delta_z^2)(\xi^n + \xi^{n+1})_{i,j} + \frac{\Delta t}{4\mu^2\sigma^2}\delta_x^2\delta_z^2(\xi^{n+1} - \xi^n)_{i,j} &= R_{i,j}^{n+\frac{1}{2}}, \\ i = 1, \dots, I-1, \quad j = 1, \dots, J-1. \end{aligned} \tag{5.4.3}$$

By Taylor expansion,

$$\begin{aligned} R_{i,j}^{n+\frac{1}{2}} &= \frac{E(x_i, z_j, t^{n+1}) - E(x_i, z_j, t^n)}{\Delta t} - \frac{1}{2\mu\sigma}(\delta_x^2 + \delta_z^2)\{E(x_i, z_j, t^n) \\ &\quad + E(x_i, z_j, t^{n+1})\} + \frac{\Delta t}{4\mu^2\sigma^2}\delta_x^2\delta_z^2\{E(x_i, z_j, t^{n+1}) - E(x_i, z_j, t^n)\} \\ &= O(\Delta t^2 + h^2), \quad i = 1, \dots, I-1, \quad j = 1, \dots, J-1. \end{aligned} \tag{5.4.4}$$

Secondly, in view of the boundary schemes for the subsurfaces (5.2.6), by Taylor expansion, we have,

$$\xi_{0,j}^n = E(x_0, z_j, t^n) - E_{0,j}^n = \xi_{1,j}^n - \frac{h^2}{2}\frac{\partial^2 E}{\partial x^2}(x_0, z_j, t^n) + O(h^3), \quad j = 0, \dots, J. \tag{5.4.5}$$

Similarly,

$$\begin{aligned} \xi_{I,j}^n &= \xi_{I-1,j}^n - \frac{h^2}{2}\frac{\partial^2 E}{\partial x^2}(x_I, z_j, t^n) + O(h^3), \quad j = 0, \dots, J, \\ \xi_{i,0}^n &= \xi_{i,1}^n - \frac{h^2}{2}\frac{\partial^2 E}{\partial z^2}(x_i, z_0, t^n) + O(h^3), \quad i = 0, \dots, I. \end{aligned} \tag{5.4.6}$$

By considering the scheme for the earth-air interface (5.2.9) and (5.2.10), we

have the corresponding error equation

$$\frac{3\xi_{i,J}^n - 4\xi_{i,J-1}^n + \xi_{i,J-2}^n}{2h} + \frac{1}{\pi} \sum_{k=1}^{I-2} \frac{\xi_{k+1,J}^n - \xi_{k,J}^n}{x_i - x_{k+\frac{1}{2}}} = \tilde{R}_{i,J}^n, \quad i = 1, \dots, I-1. \quad (5.4.7)$$

Using Taylor expansion and the upward continuation (5.1.2), we have:

$$\begin{aligned} \tilde{R}_{i,J}^n &= \frac{3E(x_i, z_J, t^n) - 4E(x_i, z_{J-1}, t^n) + E(x_i, z_{J-2}, t^n)}{2h} \\ &+ \frac{1}{\pi} \sum_{k=1}^{I-2} \frac{E(x_{k+1}, z_J, t^n) - E(x_k, z_J, t^n)}{x_i - x_{k+\frac{1}{2}}} \\ &= O(h^2). \quad (\text{since the mid-point integral formula is } O(h^2)) \end{aligned} \quad (5.4.8)$$

□

To derive the error estimation for the ADI-FDTD scheme in the discrete  $L^2$  norm, multiplying both sides of (5.4.3) with  $(\xi_{i,j}^n + \xi_{i,j}^{n+1})$  and computing the inner product, we obtain

$$\begin{aligned} Err_1 &= \left( \frac{\xi^{n+1} - \xi^n}{\Delta t}, \xi^{n+1} + \xi^n \right) = \frac{1}{\Delta t} (\|\xi^{n+1}\|^2 - \|\xi^n\|^2), \\ Err_2 &= \left( -\frac{1}{2\mu\sigma} (\delta_x^2 + \delta_z^2) (\xi^n + \xi^{n+1}), \xi^n + \xi^{n+1} \right) = Err_{2_1} + Err_{2_2}, \\ Err_3 &= \left( \frac{\Delta t}{4\mu^2\sigma^2} \delta_x^2 \delta_z^2 (\xi^{n+1} - \xi^n), \xi^{n+1} + \xi^n \right), \\ Err_4 &= \left( R^{n+\frac{1}{2}}, \xi^n + \xi^{n+1} \right). \end{aligned} \quad (5.4.9)$$

Since  $Err_{2_1}$ ,  $Err_{2_2}$ ,  $Err_3$  and  $Err_4$  are estimated using Lemma 2 and similar method as that for the stability analysis, thus we will omit the detailed procedures

and present the final conclusion,

$$\begin{aligned} \|\xi^n\|^2 + \frac{\Delta t^2}{4\mu^2\sigma^2h^2} \|\delta_x\delta_z\xi^n\|^2 &\leq \|\xi^0\|^2 + \frac{\Delta t^2}{4\mu^2\sigma^2h^2} \|\delta_x\delta_z\xi^0\|^2 \\ &+ \Delta t \left(1 + \frac{M_0}{\mu\sigma h^2} + \frac{2\Delta t M_0}{\mu^2\sigma^2h^4}\right) \sum_{k=1}^n \|\xi^k\|^2 + O(\Delta t^4 + h^4). \end{aligned} \quad (5.4.10)$$

Notice that  $\xi_{i,j}^0 = 0$ , and by the Gronwall Lemma, we obtain the following theorem.

**Theorem 4.** (Convergence) Assume that  $E(x, z, t)$  is the exact solution of the IVB problem (5.1.2)-(5.1.4) and is of sufficient smoothness, let  $E_{i,j}^n$  be the numerical solution of the ADI-FDTD scheme (5.2.2)-(5.2.6) and define error  $\xi_{i,j}^n = E(x_i, z_j, t^n) - E_{i,j}^n$ , then there exists a positive constant  $M$ , such that

$$\max_{n \leq [T/\Delta t]} \|\xi^n\|^2 \leq M(\Delta t^2 + h^2). \quad (5.4.11)$$

## 5.5 Numerical Simulations

To validate the proposed ADI-FDTD scheme for 2D TEM models, we present the computational results for the following test cases. Particular attentions will focus on demonstrating the accuracy and performance advantages of the presented algorithm over the popular FDTD method based on DuFort-Frankel method. Three test cases have been taken as test examples to validate our ADI-FDTD considered in [76].

### 5.5.1 Half-space

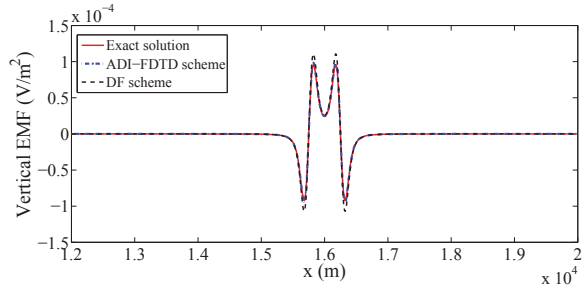
As a first check of the proposed numerical algorithm, we compute the responses of a homogeneous half-space to the shut-off of a steady current in a double line source at the surface. The test case is chosen because the analytical solution is available for both the electric field at the surface and in the half-space. The initial condition is taken as that reported in [76].

The computational domain is  $[0,32000\text{m}] \times [0,10000\text{m}]$  and the double line source is set at the centre of the earth-air interface with the negative limb located at  $x = 16250\text{m}$  and the positive limb at  $x = 15750\text{m}$ . The current is  $I = 1\text{A}$  and the electric conductivity of the ground is  $\sigma = 1/300\text{S/m}$ .

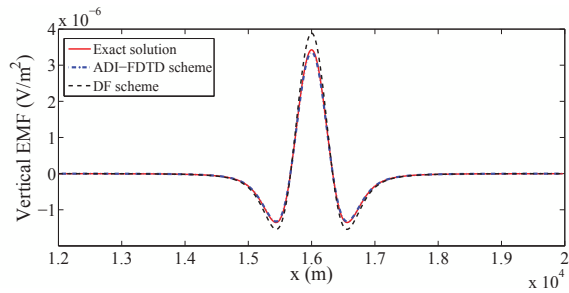
In our simulations, the inhomogeneous grids are adopted along  $x$  and  $z$  directions with an increasing step size according to the distance from the source, with the smallest step size  $\Delta x = \Delta z = h_{min} = 10\text{m}$  for the grids near the source. In terms of the initial condition, we take  $t_0 = 2.0 \times 10^{-6}$  and the top eight-layer electric field is assigned. The time step  $\Delta t$  used in the computation is listed in Table 5.1.

Table 5.1: Time steps in second for the ADI-FDTD and DF schemes

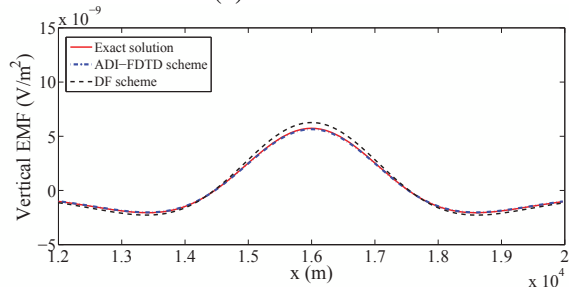
response time(ms)	$\Delta t$ for DF	$\Delta t$ for ADI-FDTD
(0, 0.1)	1.1793e-7	9.4345e-7
(0.1, 1)	1.1793e-6	1.8869e-5
> 1	2.3586e-6	3.7738e-5



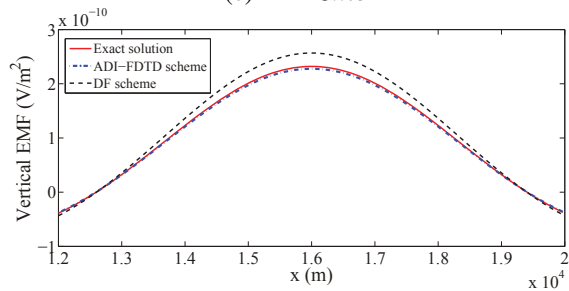
(a)  $T = 0.007ms$



(b)  $T = 0.1ms$



(c)  $T = 3ms$



(d)  $T = 15ms$

Figure 5.2: Comparison of analytical and numerical solutions computed by the ADI-FDTD and DF schemes for the vertical EMF ( $\partial_t B_z$ ) induced by a double line source on a half-space. Profiles are at (a)0.007 ms, (b)0.1 ms, (c)3 ms, (d)15 ms after the source current was switched off.

Table 5.2: CPU time in second for the ADI-FDTD and DF schemes

simulation time(ms)	DF	ADI-FDTD
0.007	9	52
0.1	128	265
3	442	482
15	1292	1240

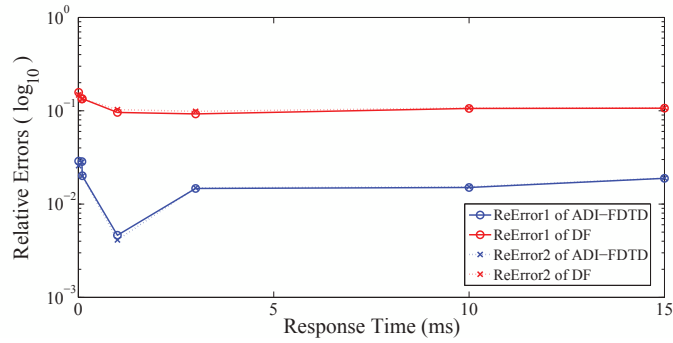


Figure 5.3: Relative  $L_\infty$  and  $L^2$  errors for the ADI-FDTD and DF schemes

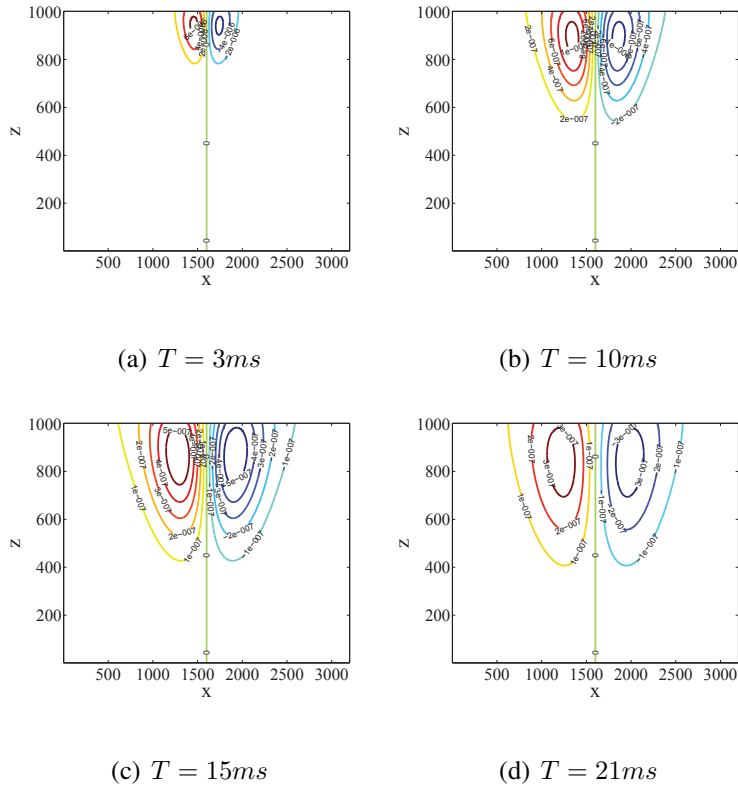


Figure 5.4: Contours of electric field in a half-space computed by the ADI-FDTD scheme induced by a switched-off 500m wide double line source at the earth-air interface. Profiles are at (a)3 ms, (b)10 ms, (c)15 ms, (d)21 ms after source current was switched off.

We now compare the performance of the developed ADI-FDTD scheme and that based on DF method [76]. The DF scheme is also unconditionally stable, but the time step  $\Delta t$  could not be taken very large in numerical simulations since oscillatory solutions might occur. Compared with the DF-FDTD method, it is worth to note that more accurate numerical results could be achieved by using the proposed ADI-FDTD algorithm.

Using the time steps listed in Table 5.1, the solution snapshots are shown in Figure 5.2, and the corresponding CPU times are reported in Table 5.2. Due to the transient of the initial electric fields, at the very beginning (generally before 0.1ms), the time steps must be chosen small enough to describe the responses without distortion. Thus it gives rise to a little longer CPU times for the ADI-FDTD method than the DF scheme at the early time. However, consider that the early time is very short compared with the total computational time, the improvement in accuracy (Ref. Figure 5.2, Figure 5.3) is more significant. In practical applications, the late time responses are generally required instead of the early time responses. From Table 5.2, after 3ms, the CPU times for these two algorithms are of the same order.

The vertical electromotive force (EMF) at the earth-air interface of the numerical solution and the exact solution are shown in Figure 5.2, and they could be obtained by measurement. Figure 5.2(a) and Figure 5.2(b) present the short time response to the switched-off of the current in the double line source, while Figure 5.2(c) and Figure 5.2(d) are the long time responses. The relative  $L_\infty$  and  $L^2$  er-

errors defined as follows are also illustrated in Figure 5.3 with respect to the response time. It is obvious to see that the ADI-FDTD scheme with large time steps produces more accurate solutions than the DF scheme with relatively small time steps. The advantage of using the presented method is clear especially for computing the late time solution. Figure 5.3 confirms that when comparing with the numerical solutions by the DF scheme, an improvement in accuracy of an order of magnitude can be achieved by using the ADI-FDTD scheme.

$$ReError1 = \frac{\|E_{numerical} - E_{exact}\|_{L^\infty(\Gamma_1)}}{\|E_{exact}\|_{L^\infty(\Gamma_1)}},$$

$$ReError2 = \frac{\|E_{numerical} - E_{exact}\|_{L^2(\Gamma_1)}}{\|E_{exact}\|_{L^2(\Gamma_1)}}.$$

Figure 5.4 gives the contours of the electric field in the whole simulation domain, which illustrates the profile of the induced field propagation. We clearly observe the diffusion of the smoke ring profiles for the electric field as time marching forward.

### 5.5.2 Half-space with conductor (large contrast)

The second test case shown in Figure 5.5 is to model a  $300\Omega\text{-m}$  half-space containing a thin rectangular ore body with the electric conductivity 1000 times more than the surroundings. The thin ore body with the scale of  $20\text{m} \times 300\text{m}$  located at 300m away from the negative line source to the left along the  $x$  direction, thus the distance of the ore body from the center of double line source is about 550m.

In this example, the time steps for the simulation are taken as in Table 5.3. For

the sake of exhibiting the influence of the anomaly elaborately, a small enough  $\Delta t$  is set for the very early time till 0.01ms. Furthermore, to demonstrate the efficiency and effectiveness of the proposed scheme, we adopt a larger time steps after 0.01ms, compared with DF scheme, as shown in Table 5.3. The vertical EMF, horizontal EMF curves and contours of the electric field induced by the switched-off of double line source are reported in Figure 5.6, Figure 5.7 and Figure 5.8, respectively.

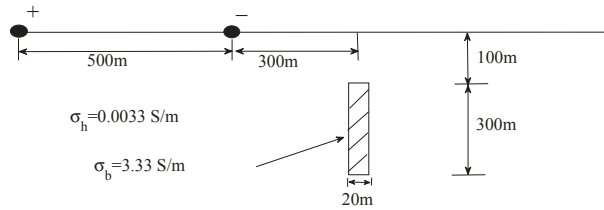


Figure 5.5: Model geometry for half-space with large-contrast conductor.

The vertical EMF ( $-\partial_t B_z$ ) profiles using the ADI-FDTD algorithm in Figure 5.6 are featured by the crossover from positive to negative values on account of the existence of the thin vertical conductor, and the location of crossover in Figure 5.6 is gradually moving to the exact horizontal position of the thin anomaly. In addition, the peak of the horizontal EMF ( $-\partial_t B_x$ ) using the ADI-FDTD algorithm displayed in Figure 5.7 could also serve to examine the horizontal position of the thin body approximately.

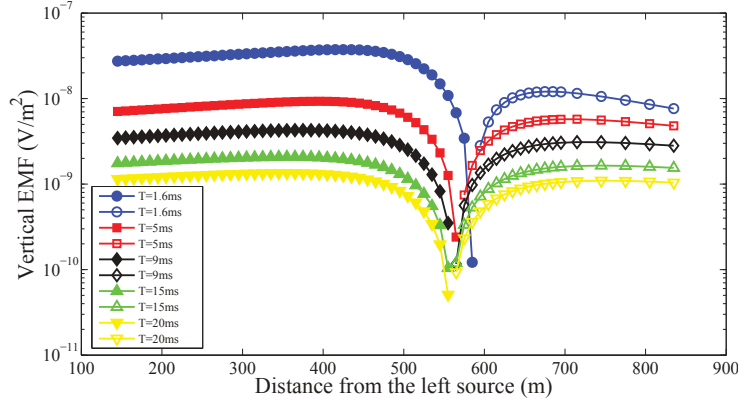


Figure 5.6: Profiles of the vertical EMF ( $\partial_t B_z$ ) by the ADI-FDTD scheme for the half-space conductor with a 1000:1 contrast. The negative line source is on the right. Open marks indicate negative values and dark marks represent positive ones.

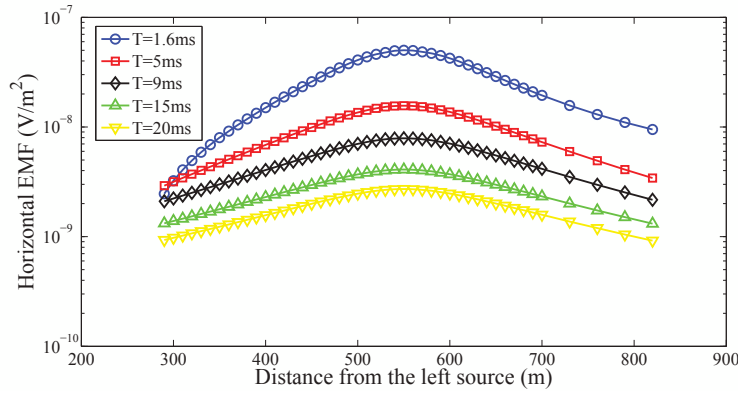
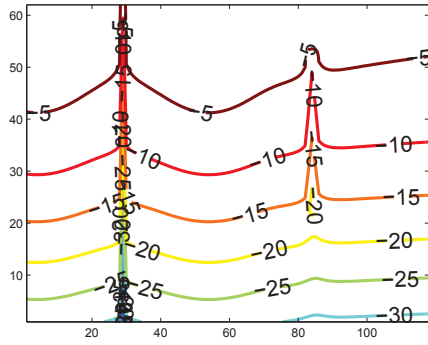


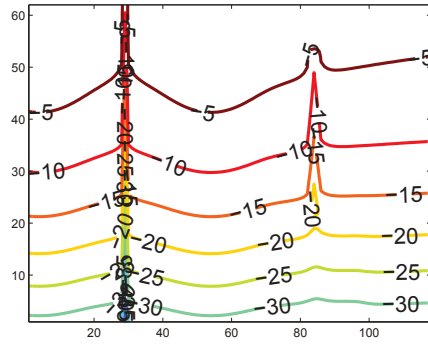
Figure 5.7: Profiles of the horizontal EMF ( $\partial_t B_x$ ) by the ADI-FDTD scheme for the half-space conductor with a 1000:1 contrast. The negative line source is on the right. Open marks indicate negative values.

Table 5.3: Time steps in second for ADI-FDTD and DF schemes

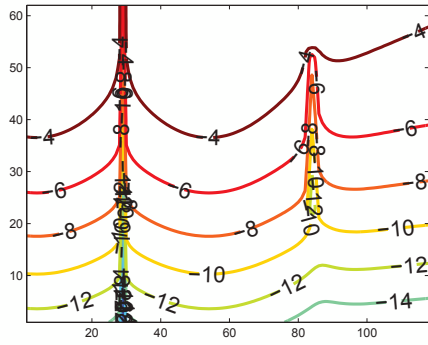
response time(ms)	$\Delta t$ for DF	$\Delta t$ for ADI-FDTD
(0, 0.01)	4.7172e-8	4.7172e-8
(0.01, 0.1)	1.1793e-7	9.4345e-7
(0.1, 1)	1.1793e-6	1.8869e-5
> 1	2.3586e-6	3.7738e-5



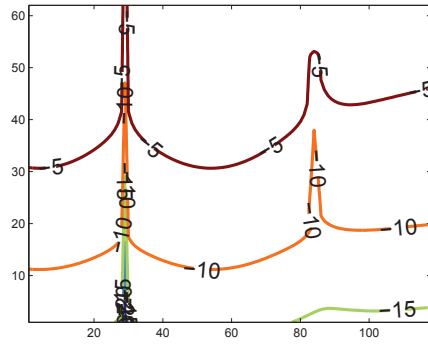
(a) ADI,  $T = 0.006ms$



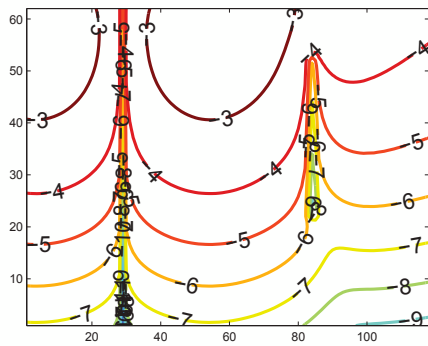
(b) DF,  $T = 0.006ms$



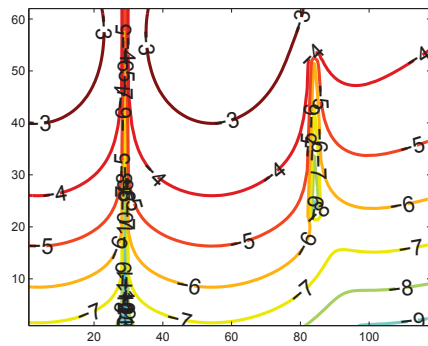
(c) ADI,  $T = 0.015ms$



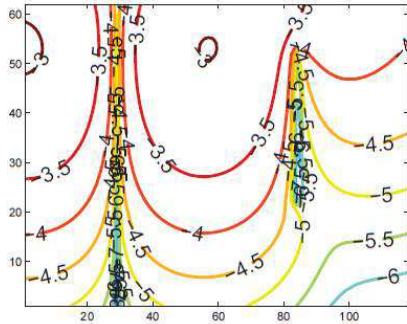
(d) DF,  $T = 0.015ms$



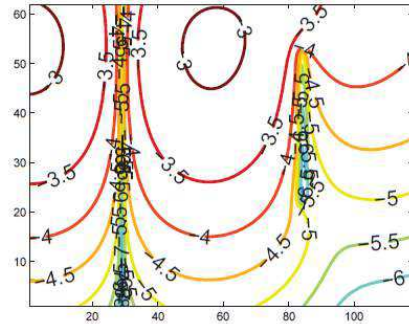
(e) ADI,  $T = 0.036ms$



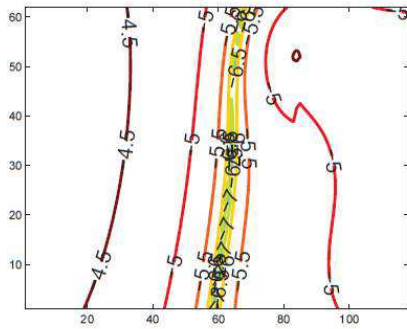
(f) DF,  $T = 0.036ms$



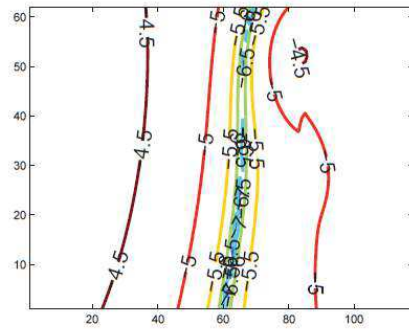
(g) ADI,  $T = 0.08ms$



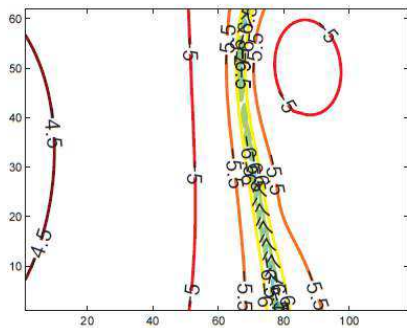
(h) DF,  $T = 0.08ms$



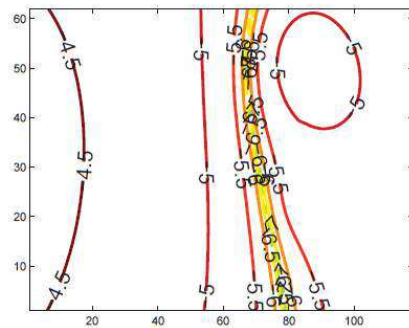
(i) ADI,  $T = 0.6ms$



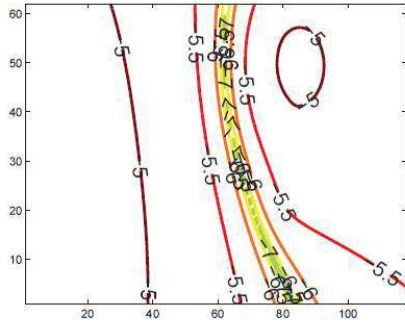
(j) DF,  $T = 0.6ms$



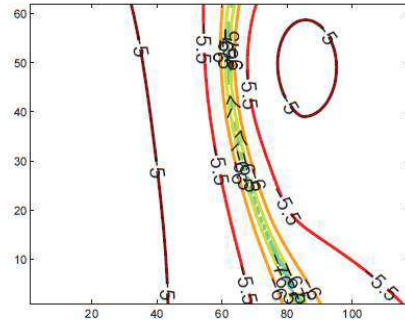
(k) ADI,  $T = 1.0ms$



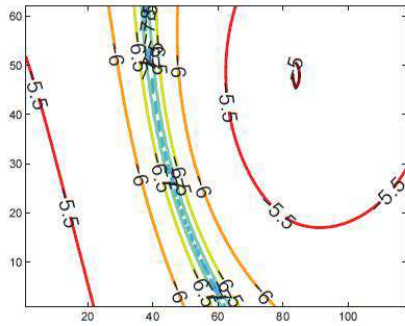
(l) DF,  $T = 1.0ms$



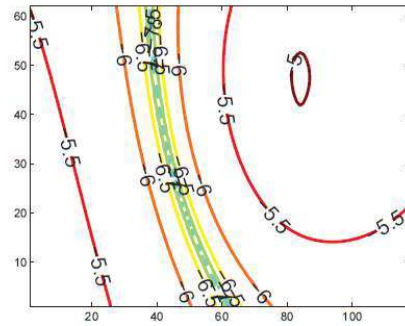
(m) ADI,  $T = 1.6ms$



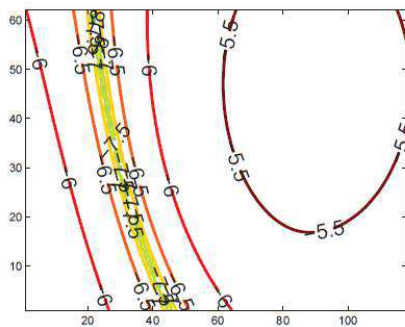
(n) DF,  $T = 1.6ms$



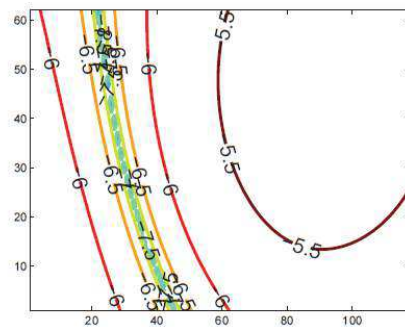
(o) ADI,  $T = 3.7ms$



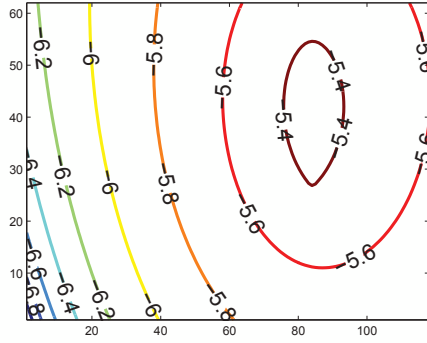
(p) DF,  $T = 3.7ms$



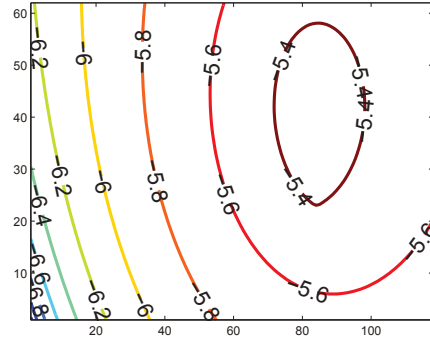
(q) ADI,  $T = 5ms$



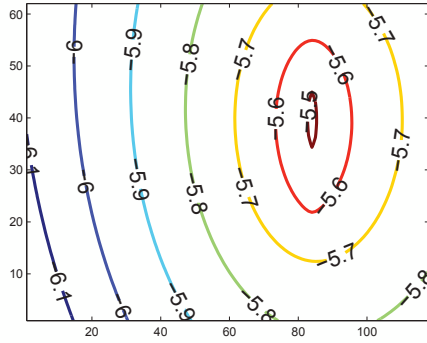
(r) DF,  $T = 5ms$



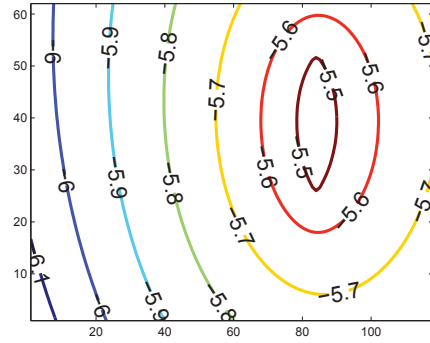
(g) ADI,  $T = 9ms$



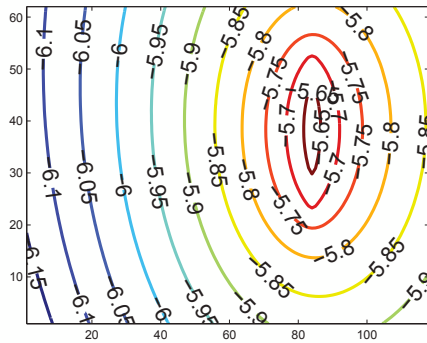
(h) DF,  $T = 9ms$



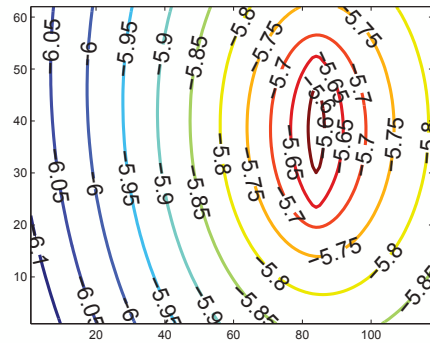
(i) ADI,  $T = 15ms$



(j) DF,  $T = 15ms$



(k) ADI,  $T = 20ms$



(l) DF,  $T = 20ms$

Figure 5.8: Contours of electric field (the values are the logarithm of  $E$ ) computed by the ADI-FDTD scheme (on the left) and the DF scheme (on the right) for the half-space with the conductor of 1000:1, induced by a switched-off 500m wide double line source at the earth-air interface.

Figure 5.8 compares the contours of the electric fields for this large contrast model using ADI-FDTD scheme(on the left) as well as the DF scheme(on the right) and the snapshots presented cover a wide range of time from the very early time 0.006ms to the late time 20ms. It is clear to observe that the two sets of results are generally consistent with each other except for some subtle distinction. Results by the ADI-FDTD method capture the responses well for both early times and late times.

To illustrate the characters of the electric field around the thin conductor and double line source, only the central and uniform regions of the numerical grids are shown. The crossover on the left of the first four subfigures makes clear the position of the source center, while the crossover on the right highlights the main domain containing the thin conductor. The following subfigures reflect that when the diffusion of electric field encounters the thin anomaly, they are distorted by the interaction with this conductor. The snapshot taken at 3.7ms displays a fully developed target response and the further evolution of the electric field involves its gradual equalization and decay within the conductor.

### **5.5.3 Half-space with conductor (small contrast)**

We now consider a small contrast(100:1) version of the second test model as illustrated in Figure 5.9<sup>1</sup>. The parameters for this simulation are set the same as those

---

<sup>1</sup>The figures in this section and following sections are prepared by Dr. Wanshan Li

in the large contrast case, except that the half-space resistivity is  $100\Omega\text{-m}$ , while the body resistivity is  $1\Omega\text{-m}$ .

From the vertical EMF presented in Figure 5.10, it is clear that even though the crossover appears at nearly the exact target position at 1 ms, it moves to the right and away from the target with time advancing. This may be attributed to the currents in the half-space, whose contribution covers some of the effect from the currents flowing in the ore body.

On the other hand, the horizontal EMF profiles shown in Figure 5.11 obviously illustrate the location of the anomaly by their peaks. Generally, in contrast to the crossover point of the vertical EMF, the peak in the horizontal EMF is always directly above the target in the millisecond time range and thus giving a better indication of the conductor location. We also report the snapshots by the ADI-FDTD and DF schemes in Figure 5.12 to reveal some details of the development of the electric field in early time and later the interaction between the smoke ring and the conductor, and their results are in good agreement.

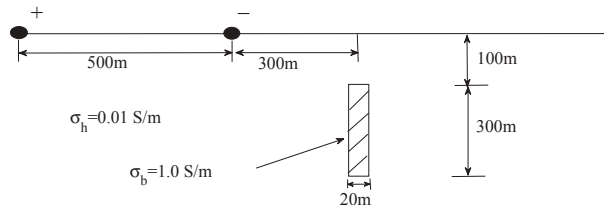


Figure 5.9: Model geometry for overburden and half-space with small-contrast conductor.

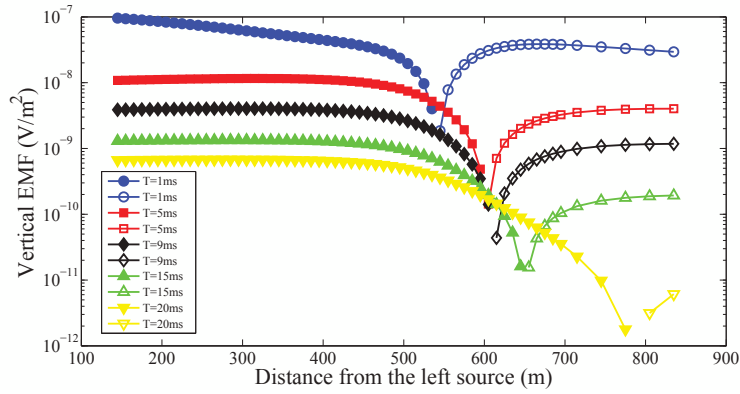


Figure 5.10: Profiles of the vertical EMF ( $\partial_t B_z$ ) by the ADI-FDTD scheme for the half-space with small contrast conductor model. The negative line source is on the right. Open marks indicate negative values and dark marks represent positive ones.

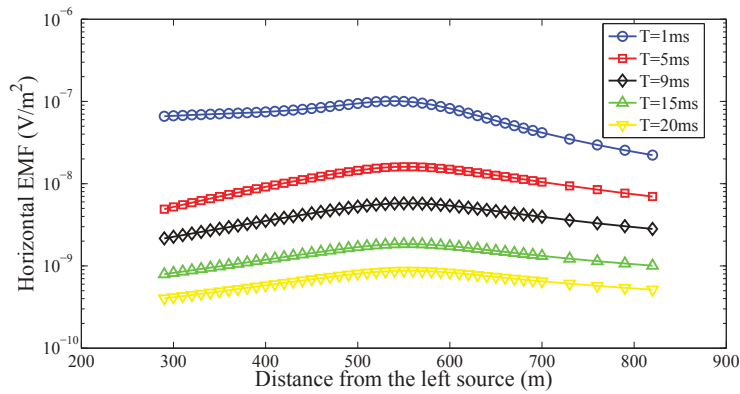
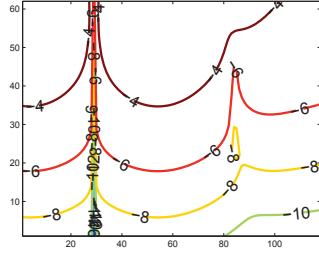
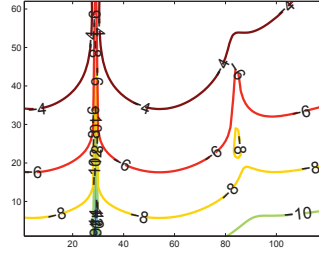


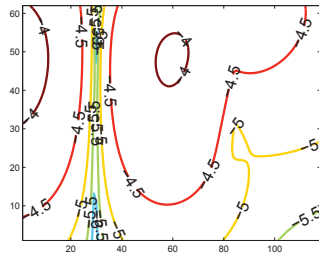
Figure 5.11: Profiles of the horizontal EMF ( $\partial_t B_x$ ) by the ADI-FDTD scheme for the half-space with small contrast conductor model. The negative line source is on the right. Open marks indicate negative values.



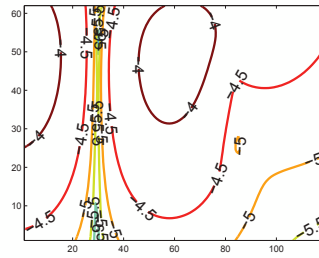
(a) ADI,  $T = 0.08ms$



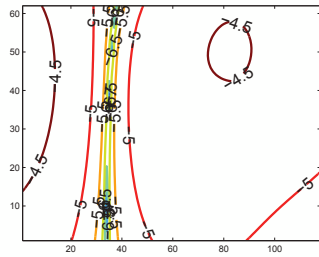
(b) DF,  $T = 0.08ms$



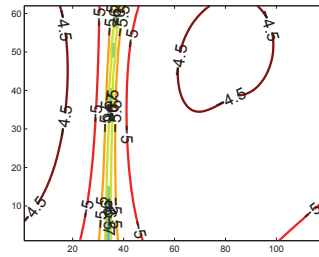
(c) ADI,  $T = 0.5ms$



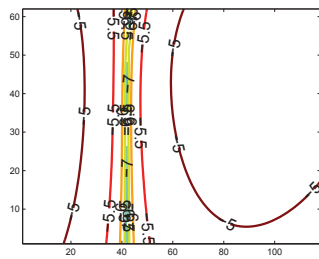
(d) DF,  $T = 0.5ms$



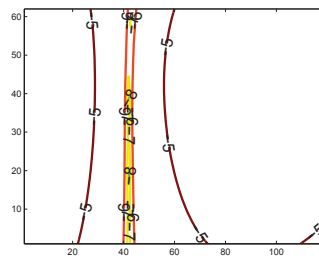
(e) ADI,  $T = 1ms$



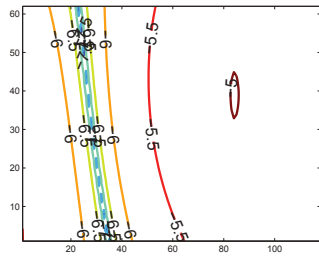
(f) DF,  $T = 1ms$



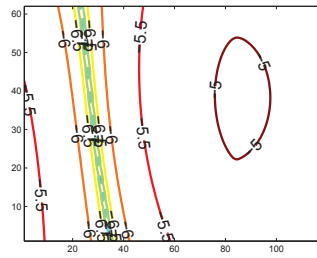
(g) ADI,  $T = 1.6ms$



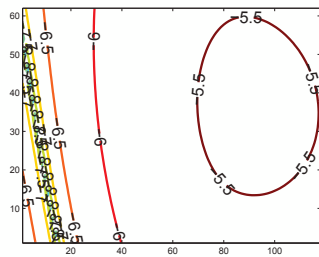
(h) DF,  $T = 1.6ms$



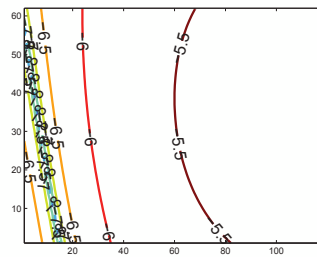
(i) ADI,  $T = 5ms$



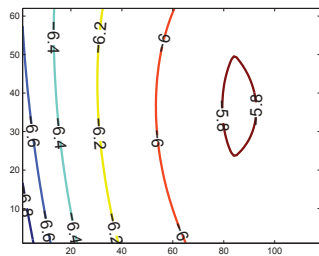
(j) DF,  $T = 5ms$



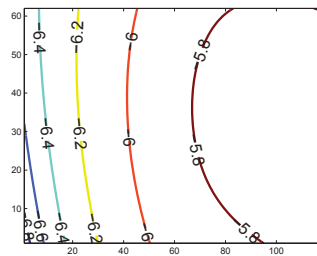
(k) ADI,  $T = 9ms$



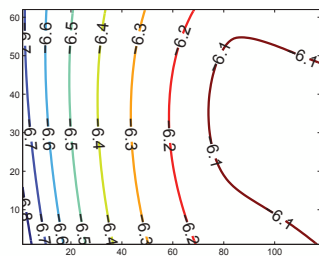
(l) DF,  $T = 9ms$



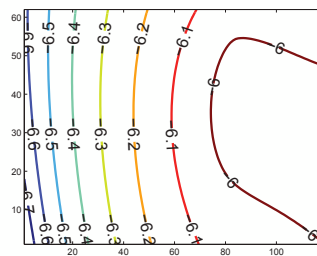
(m) ADI,  $T = 15ms$



(n) DF,  $T = 15ms$



(o) ADI,  $T = 20ms$



(p) DF,  $T = 20ms$

Figure 5.12: Contours of electric field (the values are the logarithm of  $E$ ) computed by the ADI-FDTD scheme (on the left) and the DF scheme (on the right) for the half-space with small contrast conductor model, induced by a switched-off 500m wide double line source at the earth-air interface.

## 5.6 Concluding Remarks

We present an efficient and accurate ADI-FDTD algorithm to simulate EM diffusion phenomenon in a 2D earth excited by the electric line sources. Comparisons with the analytical and DuFort-Frankel solutions confirm the accuracy and efficiency of the proposed algorithm. The ADI technique is applied such that the resultant tri-diagonal system can be effectively computed by the Thomas algorithm. To ensure an accurate representation for the earth-air interface, an integral formulation is imposed at the interface boundary. A novel numerical discretization scheme for the integral equation is presented and it is incorporated to the ADI scheme implicitly. With the numerical implementation for the integral boundary condition, the stability and convergence analysis for the ADI-FDTD scheme are reported. Numerical simulations clearly demonstrate that the proposed ADI-FDTD scheme produces more accurate computed solutions than those resulted by the DuFort-Frankel scheme both in the early time and late time computation.

It is worth to investigate further applications and improvements of the proposed ADI-FDTD algorithm. For example, consider using the secondary field instead of total field in the model. Secondary field is defined as the difference between the total field and the field of a background model, and they vary more slowly than the total field in both time and space. The application of an absorbing boundary condition including a perfectly matched layer (PML) for the underground interface

is also an interesting topic. Finally, it is important to extend the present approach for 2.5D and 3D problems.

The work reported in this chapter has been accepted and will appear in *Communications in Computational Physics* [63].

# Chapter 6

## Conclusion

This thesis is focused on the numerical analysis and mathematical modeling for the geophysical exploration problems. Potential field inversion is an important methods related to mining and oil industry. By measuring the potential field and apply the inversion schemes to the observation data, the underground structure can be recovered. The numerical inversion scheme is the key to the quality of the recovered model. Conventional inversion schemes require a huge amount of computational cost and storage requirement, which can be only run on super computer clusters.

In Chapter 2, we present a novel computational method based on conjugate gradient method. Taking advantage of Block-Toeplitz Toeplitz-Block structure, we develop a robust and efficient downward continuation scheme. The method is validated on synthetic and field data, and its superiority is verified by comparing with recently developed wavenumber domain and Taylor series methods.

Chapter 3 presents an efficient numerical inversion scheme using the idea of multi-grid technique. The scheme is efficient for the aeromagnetic field data. The most important feature of the proposed method is that it preserves the BTTB structure in each level, such that the error with different frequencies can be efficiently

removed. By synthetic and field simulation, we have shown that the BTTB-MG method is a competitive alternative to a regularized method, particularly when a high accuracy is required for the perturbed data.

Chapter 4 presents the 3D gravity field inversion problem. Compared with the 2D inversion problem, 3D inversion is much more challenging due to the complexity of the model and extremely heavy computational work load. It is reported that for the inversion with several million unknowns, the time cost of the inversion scheme can be as high as hundreds of hours by using super workstation. We expand our 2D method to the 3D gravity inversion, and made several improvements for both the regularization and preconditioner. Numerical simulations based on synthetic and real data show that for the 3D inversion with several million unknowns, our numerical scheme can be run on a laptop within several minutes to finish the inversion process. Besides, we give the strict mathematical proofs for the convergence and consistency of the numerical solution, which has not been investigated before.

In chapter 5, we investigate the electromagnetic method in exploration, which is based on modeling the electromagnetic (EM) wave diffusion underground to recover the conductivity distribution. EM problem is a very challenging problem in terms of algorithm complexity and stability. We proposed an implicit ADI-FDTD scheme to simulate the diffusion behavior of the EM wave. The time and space grids in our proposed scheme can be much larger than that in the conventional Du-Fort-Frankel method, while the accuracy of the numerical solution is superior to the conventional

method for an order.

# Bibliography

- [1] J. Abbiss and P. Earwicker. Compact operator equations, regularization and super-resolution. *Mathematics in Signal Processing, T. Durrani et al., eds., Clarendon Press, Oxford, 1987.*
- [2] J. I. Adhidjaja, G. W. Hohmann, and M. L. Oristaglio. Two-dimensional transient electromagnetic responses. *Geophysics*, 50(12):2849–2861, 1985.
- [3] M. B. Allen and E. L. Isaacson. *Numerical analysis for applied science*, volume 35. John Wiley & Sons, 2011.
- [4] U. Ascher and E. Haber. Grid refinement and scaling for distributed parameter estimation problems. *Inverse Problems*, 17(3):571, 2001.
- [5] A. Asnaashari, R. Brossier, S. Garambois, F. Audebert, P. Thore, and J. Virieux. Regularized seismic full waveform inversion with prior model information. *Geophysics*, 78(2):R25–R36, 2013.
- [6] H. R. Babu, A. Subrahmanyam, and D. A. Rao. A comparative study of the relation figures of magnetic anomalies due to two-dimensional dike and vertical step models. *Geophysics*, 47(6):926–931, 1982.
- [7] M. Beiki and L. B. Pedersen. Eigenvector analysis of gravity gradient tensor to locate geologic bodies. *Geophysics*, 75(6):I37–I49, 2010.
- [8] A. Björck. *Numerical methods for least squares problems*. SIAM, 1996.
- [9] R. J. Blakely. *Potential theory in gravity and magnetic applications*. Cambridge University Press, 1996.
- [10] I. C. Briggs. Machine contouring using minimum curvature. *Geophysics*, 39(1):39–48, 1974.
- [11] W. L. Briggs and S. F. McCormick. *A multigrid tutorial*, volume 72. SIAM, 2000.

- [12] A. G. Camacho, F. G. Montesinos, and R. Vieira. Gravity inversion by means of growing bodies. *Geophysics*, 65(1):95–101, 2000.
- [13] F. Caratori Tontini, L. Cocchi, and C. Carmisciano. Rapid 3-D forward model of potential fields with application to the Palinuro seamount magnetic anomaly (southern Tyrrhenian sea, Italy). *Journal of Geophysical Research: Solid Earth (1978–2012)*, 114(B2), 2009.
- [14] R. Cassinis. *The solution of the inverse problem in geophysical interpretation*, volume 11. Springer Science & Business Media, 2013.
- [15] R. H. Chan and X. Q. Jin. *An introduction to iterative Toeplitz solvers*, volume 5. SIAM, 2007.
- [16] R. H. Chan, J. G. Nagy, and R. J. Plemmons. FFT-based preconditioners for Toeplitz-Block least squares problems. *SIAM journal on numerical analysis*, 30(6):1740–1768, 1993.
- [17] R. H. Chan and M. K. Ng. Conjugate gradient methods for Toeplitz systems. *SIAM review*, 38(3):427–482, 1996.
- [18] W. Chen, X. Li, and D. Liang. Symmetric energy-conserved splitting FDTD scheme for the Maxwell’s equations. *Communications in Computational Physics*, 6(4):804–825, 2009.
- [19] Y. Chung, J.-S. Son, T. J. Lee, H. J. Kim, and C. Shin. Three-dimensional modelling of controlled-source electromagnetic surveys using an edge finite-element method with a direct solver. *Geophysical Prospecting*, 2014.
- [20] G. K. Clarke. Optimum second-derivative and downward-continuation filters. *Geophysics*, 34(3):424–437, 1969.
- [21] M. Commer and G. Newman. A parallel finite-difference approach for 3D transient electromagnetic modeling with galvanic sources. *Geophysics*, 69(5):1192–1202, 2004.
- [22] S. Constable and C. J. Weiss. Mapping thin resistors and hydrocarbons with marine EM methods: Insights from 1D modeling. *Geophysics*, 71(2):G43–G51, 2006.

- [23] G. Cooper. Gridding gravity data using an equivalent layer. *Computers & Geosciences*, 26(2):227–233, 2000.
- [24] G. Cooper. The stable downward continuation of potential field data. *Exploration Geophysics*, 35(4):260–265, 2004.
- [25] L. Cordell. A scattered equivalent-source method for interpolation and gridding of potential-field data in three dimensions. *Geophysics*, 57(4):629–636, 1992.
- [26] L. H. Cox, G. A. Wilson, and M. S. Zhdanov. 3D inversion of airborne electromagnetic data using a moving footprint. *Exploration Geophysics*, 41(4):250–259, 2010.
- [27] M. Čuma, G. A. Wilson, and M. S. Zhdanov. Large-scale 3D inversion of potential field data. *Geophysical Prospecting*, 60(6):1186–1199, 2012.
- [28] N. V. Silva, J. V. Morgan, L. MacGregor, and M. Warner. A finite element multifrontal method for 3D csem modeling in the frequency domain. *Geophysics*, 77(2):E101–E115, 2012.
- [29] K. Davis and Y. Li. Fast solution of geophysical inversion using adaptive mesh, space-filling curves and wavelet compression. *Geophysical Journal International*, 185(1):157–166, 2011.
- [30] K. Davis and Y. Li. Efficient 3D inversion of magnetic data via octree-mesh discretization, space-filling curves, and wavelets. *Geophysics*, 78(5):J61–J73, 2013.
- [31] P. J. Davis. *Circulant matrices*. American Mathematical Soc., 1979.
- [32] W. C. Dean. Frequency analysis for gravity and magnetic interpretation. *Geophysics*, 23(1):97–127, 1958.
- [33] L. Eldén. An algorithm for the regularization of ill-conditioned, banded least squares problems. *SIAM journal on scientific and statistical computing*, 5(1):237–254, 1984.

- [34] M. Everett and R. Edwards. Transient marine electromagnetics: the 2.5-D forward problem. *Geophysical Journal International*, 113(3):545–561, 1993.
- [35] M. Fedi and G. Florio. Detection of potential fields source boundaries by enhanced horizontal derivative method. *Geophysical prospecting*, 49(1):40–58, 2001.
- [36] M. Fedi and G. Florio. A stable downward continuation by using the ISVD method. *Geophysical Journal International*, 151(1):146–156, 2002.
- [37] R. W. Freund and N. M. Nachtigal. An implementation of the QMR method based on coupled two-term recurrences. *SIAM Journal on Scientific Computing*, 15(2):313–337, 1994.
- [38] L. Gao and D. Liang. New energy-conserved identities and super-convergence of the symmetric EC-S-FDTD scheme for Maxwell’s equations in 2D. *Communications in Computational Physics*, 11(5):1673–1696, 2012.
- [39] A. García-Yeguas, I. Koulakov, J. M. Ibáñez, and A. Rietbrock. High resolution 3D p wave velocity structure beneath Tenerife island (Canary islands, Spain) based on tomographic inversion of active-source data. *Journal of Geophysical Research: Solid Earth (1978–2012)*, 117(B9), 2012.
- [40] S. P. Gay Jr. Standard curves for interpretation of magnetic anomalies over long tabular bodies. *Geophysics*, 28(2):161–200, 1963.
- [41] Y. Goldman, C. Hubans, S. Nicoletis, and S. Spitz. A finite-element solution for the transient electromagnetic response of an arbitrary two-dimensional resistivity distribution. *Geophysics*, 51(7):1450–1461, 1986.
- [42] A. Grayver, R. Streich, and O. Ritter. Three-dimensional parallel distributed inversion of CSEM data using a direct forward solver. *Geophysical Journal International*, 193(3):1432–1446, 2013.
- [43] A. V. Grayver and M. Bürg. Robust and scalable 3-D geo-electromagnetic modelling approach using the finite element method. *Geophysical Journal International*, page ggu119, 2014.

- [44] T. H. Gronwall. Note on the derivatives with respect to a parameter of the solutions of a system of differential equations. *Annals of Mathematics*, 20(2):292–296, 1919.
- [45] E. Haber and U. M. Ascher. Fast finite volume simulation of 3D electromagnetic problems with highly discontinuous coefficients. *SIAM Journal on Scientific Computing*, 22(6):1943–1961, 2001.
- [46] E. Haber, S. Heldmann, and U. Ascher. Adaptive finite volume method for distributed non-smooth parameter identification. *Inverse Problems*, 23(4):1659, 2007.
- [47] E. Haber and C. Schwarzbach. Parallel inversion of large-scale airborne time-domain electromagnetic data with multiple octree meshes. *Inverse Problems*, 30(5):055011, 2014.
- [48] J. Hadamard. Sur les problmes aux drives partielles et leur signification physique. *Princeton University Bulletin*, 49 – 52, 1902.
- [49] P. C. Hansen. *The L-curve and its use in the numerical treatment of inverse problems*. IMM, Department of Mathematical Modelling, Technical University of Denmark, 1999.
- [50] P. Hornby, F. Boschetti, and F. Horowitz. Analysis of potential field data in the wavelet domain. *Geophysical Journal International*, 137(1):175–196, 1999.
- [51] J. Huang and A. Wood. Analysis and numerical solution of transient electromagnetic scattering from overfilled cavities. *Communications in Computational Physics*, 1(6):1043–1055, 2006.
- [52] J. Huang, A. W. Wood, and M. J. Havrilla. A hybrid finite element-laplace transform method for the analysis of transient electromagnetic scattering by an over-filled cavity in the ground plane. *Communications in Computational Physics*, 5(1):126–141, 2009.
- [53] X. Jiang, L. Zhang, and W. Zheng. Adaptive HP-finite element computations for time-harmonic Maxwells equations. *Communications in Computational Physics*, 13(2):559–582, 2013.

- [54] J. Douglas. On the numerical integration  $\frac{\partial^2 u}{\partial x^2} + \frac{\partial^2 u}{\partial y^2} = \frac{\partial u}{\partial t}$  by implicit methods. *Journal of Society for Industrial and Applied Mathematics*, 3(1):42–65, 1955.
- [55] K. Key. 1D inversion of multicomponent, multifrequency marine CSEM data: Methodology and synthetic studies for resolving thin resistive layers. *Geophysics*, 74(2):F9–F20, 2009.
- [56] K. Key and J. Oval. A parallel goal-oriented adaptive finite element method for 2.5-D electromagnetic modelling. *Geophysical Journal International*, 186(1):137–154, 2011.
- [57] J. Koldan, V. Puzyrev, J. de la Puente, G. Houzeaux, and J. M. Cela. Algebraic multigrid preconditioning within parallel finite-element solvers for 3-D electromagnetic modelling problems in geophysics. *Geophysical Journal International*, 197(3):1442–1458, 2014.
- [58] R. A. Krahenbuhl and Y. Li. Inversion of gravity data using a binary formulation. *Geophysical Journal International*, 167(2):543–556, 2006.
- [59] J. T. Kuo and D.-h. Cho. Transient time-domain electromagnetics. *Geophysics*, 45(2):271–291, 1980.
- [60] R. Lane and A. Guillen. Geologically-inspired constraints for a potential field litho-inversion scheme. In *Proceedings of IAMG*, volume 5, pages 181–186, 2005.
- [61] K. H. Lee. Electromagnetic scattering by two-dimensional inhomogeneity due to an oscillating magnetic dipole. 1978.
- [62] M. Leppin. Electromagnetic modeling of 3-D sources over 2-D inhomogeneities in the time domain. *Geophysics*, 57(8):994–1003, 1992.
- [63] W. Li, Y. Zhang, Y. S. Wong, and D. Liang. ADI-FDTD method for two-dimensional transient electromagnetic problems. *Communications in Computational Physics*, 19(1):94–123, 2016.
- [64] Y. Li and D. W. Oldenburg. 3-D inversion of magnetic data. *Geophysics*, 61(2):394–408, 1996.

- [65] Y. Li and D. W. Oldenburg. 3-D inversion of gravity data. *Geophysics*, 63(1):109–119, 1998.
- [66] Y. Li and D. W. Oldenburg. Fast inversion of large-scale magnetic data using wavelet transforms and a logarithmic barrier method. *Geophysical Journal International*, 152(2):251–265, 2003.
- [67] G. Ma, C. Liu, D. Huang, and L. Li. A stable iterative downward continuation of potential field data. *Journal of Applied Geophysics*, 98:205–211, 2013.
- [68] F. A. Maaø. Fast finite-difference time-domain modeling for marine-subsurface electromagnetic problems. *Geophysics*, 72(2):A19–A23, 2007.
- [69] M. Malinowski, S. Operto, and A. Ribodetti. High-resolution seismic attenuation imaging from wide-aperture onshore data by visco-acoustic frequency-domain full-waveform inversion. *Geophysical Journal International*, 186(3):1179–1204, 2011.
- [70] C. A. Mendonca and J. B. Silva. Interpolation of potential-field data by equivalent layer and minimum curvature: A comparative analysis. *Geophysics*, 60(2):399–407, 1995.
- [71] W. Menke. *Geophysical data analysis: discrete inverse theory*. Academic press, 2012.
- [72] S. Mukherjee and M. E. Everett. 3d controlled-source electromagnetic edge-based finite element modeling of conductive and permeable heterogeneities. *Geophysics*, 76(4):F215–F226, 2011.
- [73] T. Namiki. A new FDTD algorithm based on alternating-direction implicit method. *IEEE Transactions on Microwave Theory and Techniques*, 47(10):2003–2007, 1999.
- [74] M. Okabe. Analytical expressions for gravity anomalies due to homogeneous polyhedral bodies and translations into magnetic anomalies. *Geophysics*, 44(4):730–741, 1979.
- [75] D. Oldenburg, P. McGillivray, and R. Ellis. Generalized subspace methods for large-scale inverse problems. *Geophysical Journal International*, 114(1):12–20, 1993.

- [76] M. L. Oristaglio and G. W. Hohmann. Diffusion of electromagnetic fields into a two-dimensional earth: A finite-difference approach. *Geophysics*, 49(7):870–894, 1984.
- [77] C. C. Paige and M. A. Saunders. Lsqr: An algorithm for sparse linear equations and sparse least squares. *ACM Transactions on Mathematical Software (TOMS)*, 8(1):43–71, 1982.
- [78] R. Pašteka, R. Karcol, D. Kušnirák, and A. Mojzeš. Regcont: A Matlab based program for stable downward continuation of geophysical potential fields using Tikhonov regularization. *Computers & Geosciences*, 49:278–289, 2012.
- [79] R. S. Pawlowski. Preferential continuation for potential-field anomaly enhancement. *Geophysics*, 60(2):390–398, 1995.
- [80] D. W. Peaceman and H. H. Rachford Jr. The numerical solution of parabolic and elliptic differential equations. *Journal of the Society for Industrial and Applied Mathematics*, 3(1):28–41, 1955.
- [81] D. O. Pérez, D. R. Velis, and M. D. Sacchi. High-resolution prestack seismic inversion using a hybrid fista least-squares strategy. *Geophysics*, 78(5):R185–R195, 2013.
- [82] M. Pilkington. 3-D magnetic imaging using conjugate gradients. *Geophysics*, 62(4):1132–1142, 1997.
- [83] M. Pilkington and D. Crossley. Determination of crustal interface topography from potential fields. *Geophysics*, 51(6):1277–1284, 1986.
- [84] O. Portniaguine and M. S. Zhdanov. 3-D magnetic inversion with data compression and image focusing. *Geophysics*, 67(5):1532–1541, 2002.
- [85] A. Pustisek. Noniterative three-dimensional inversion of magnetic data. *Geophysics*, 55(6):782–785, 1990.
- [86] V. Puzyrev, J. Koldan, J. de la Puente, G. Houzeaux, M. Vázquez, and J. M. Cela. A parallel finite-element method for three-dimensional controlled-source electromagnetic forward modelling. *Geophysical Journal International*, page ggt027, 2013.

- [87] D. A. Rao and H. R. Babu. Nomograms for rapid evaluation of magnetic anomalies over long tabular bodies. *pure and applied geophysics*, 119(5):1037–1050, 1981.
- [88] R. Rao, V. Vijayakumar, G. Virupakshi, and M. Rao. A note on the interpretation of magnetic anomalies of infinite thin sheets by using relation figures. *Geophysical prospecting*, 33(5):746–752, 1985.
- [89] M. Rauth and T. Strohmer. Smooth approximation of potential fields from noisy scattered data. *Geophysics*, 63(1):85–94, 1998.
- [90] Z. Ren, T. Kalscheuer, S. Greenhalgh, and H. Maurer. A goal-oriented adaptive finite-element approach for plane wave 3-D electromagnetic modelling. *Geophysical Journal International*, 194(2):700–718, 2013.
- [91] A. Salem and D. Ravat. A combined analytic signal and Euler method (AN-EUL) for automatic interpretation of magnetic data. *Geophysics*, 68(6):1952–1961, 2003.
- [92] C. Schwarzbach and E. Haber. Finite element based inversion for time-harmonic electromagnetic problems. *Geophysical Journal International*, 193(2):615–634, 2013.
- [93] P. Shamsipour, D. Marcotte, M. Chouteau, and P. Keating. 3D stochastic inversion of gravity data using cokriging and cosimulation. *Geophysics*, 75(1):I1–I10, 2010.
- [94] W.-H. T. Sheu, L. Y. Liang, and J.-H. Li. Development of an explicit symplectic scheme that optimizes the dispersion-relation equation for the Maxwell’s equations. *Communications in Computational Physics*, 13(4):1107–1133, 2013.
- [95] J. B. Silva and G. W. Hohmann. Nonlinear magnetic inversion using a random search method. *Geophysics*, 48(12):1645–1658, 1983.
- [96] J. B. Silva, A. S. Oliveira, and V. C. Barbosa. Gravity inversion of 2D basement relief using entropic regularization. *Geophysics*, 75(3):I29–I35, 2010.

- [97] M. Sommer, S. Hölz, M. Moorkamp, A. Swidinsky, B. Heincke, C. Scholl, and M. Jegen. GPU parallelization of a three dimensional marine CSEM code. *Computers & Geosciences*, 58:91–99, 2013.
- [98] R. Streich. 3D finite-difference frequency-domain modeling of controlled-source electromagnetic data: Direct solution and optimization for high accuracy. *Geophysics*, 74(5):F95–F105, 2009.
- [99] R. Streich, M. Becken, and O. Ritter. 2.5 D controlled-source EM modeling with general 3D source geometries. *Geophysics*, 76(6):F387–F393, 2011.
- [100] H. W. Sun, X. Q. Jin, and Q. S. Chang. Convergence of the multigrid method of ill-conditioned block toeplitz systems. *BIT Numerical Mathematics*, 41(1):179–190, 2001.
- [101] Y. Sun and F. Tao. Symplectic and multisymplectic numerical methods for Maxwell’s equations. *Journal of Computational Physics*, 230(5):2076–2094, 2011.
- [102] A. Taflove. Application of the finite-difference time-domain method to sinusoidal steady-state electromagnetic-penetration problems. *Electromagnetic Compatibility, IEEE Transactions on*, (3):191–202, 1980.
- [103] L. Thomas. *Elliptic Problems in Linear Differential Equations over a Network*. 1949.
- [104] D. Thompson. Euldph: A new technique for making computer-assisted depth estimates from magnetic data. *Geophysics*, 47(1):31–37, 1982.
- [105] A. N. Tikhonov and V. Y. Arsenin. *Solutions of ill-posed problems*. 1977.
- [106] A. N. Tikhonov, V. B. Glasko, OK. Litvinen, and V. P. Melikhov. Analytic continuation of a potential in the direction of disturbing masses by the regularization method. *Geophysics*, 34(6):1020.
- [107] H. Trompat, F. Boschetti, and P. Hornby. Improved downward continuation of potential field data. *Exploration Geophysics*, 34(4):249–256, 2003.
- [108] L. Uieda and V. C. Barbosa. Robust 3D gravity gradient inversion by planting anomalous densities. *Geophysics*, 77(4):G55–G66, 2012.

- [109] E. S. Um, M. Commer, and G. A. Newman. Efficient pre-conditioned iterative solution strategies for the electromagnetic diffusion in the earth: finite-element frequency-domain approach. *Geophysical Journal International*, page ggt071, 2013.
- [110] E. S. Um, J. M. Harris, and D. L. Alumbaugh. 3D time-domain simulation of electromagnetic diffusion phenomena: A finite-element electric-field approach. *Geophysics*, 75(4):F115–F126, 2010.
- [111] J. Vanthienen, C. Mues, G. Wets, and K. Delaere. A tool-supported approach to inter-tabular verification. *Expert systems with applications*, 15(3):277–285, 1998.
- [112] T. Wang and G. W. Hohmann. A finite-difference, time-domain solution for three-dimensional electromagnetic modeling. *Geophysics*, 58(6):797–809, 1993.
- [113] Z. Xie, B. Wang, and Z. Zhang. Space-time discontinuous galerkin method for Maxwell’s equations. *Communications in Computational Physics*, 14(4):916–939, 2013.
- [114] S. Z. Xu, J. Yang, C. Yang, P. Xiao, S. Chen, and Z. Guo. The iteration method for downward continuation of a potential field from a horizontal plane. *Geophysical Prospecting*, 55(6):883–889, 2007.
- [115] K. S. Yee et al. Numerical solution of initial boundary value problems involving Maxwell’s equations in isotropic media. *IEEE Trans. Antennas Propag*, 14(3):302–307, 1966.
- [116] M. Zaslavsky, V. Druskin, S. Davydycheva, L. Knizhnerman, A. Abubakar, and T. Habashy. Hybrid finite-difference integral equation solver for 3D frequency domain anisotropic electromagnetic problems. *Geophysics*, 76(2):F123–F137, 2011.
- [117] X. Zeng, X. Li, J. Su, D. Liu, and H. Zou. An adaptive iterative method for downward continuation of potential-field data from a horizontal plane. *Geophysics*, 78(4):J43–J52, 2013.

- [118] H. Zhang, D. Ravat, and X. Hu. An improved and stable downward continuation of potential field data: The truncated Taylor series iterative downward continuation method. *Geophysics*, 78(5):J75–J86, 2013.
- [119] Y. Zhang and Y. S. Wong. BTTB-based numerical schemes for three-dimensional gravity field inversion. *Geophysical Journal International*, 203(1):243–256, 2015.
- [120] Y. Zhang, Y. S. Wong, J. Deng, S. Lei, and J. Lambert. Numerical inversion schemes for magnetization using aeromagnetic data. *International Journal of Numerical Analysis & Modeling*, 12(4):684–703, 2015.
- [121] Y. Zhang, Y. S. Wong, and Y. Lin. BTTB-RRCG method for downward continuation of potential field data. *Journal of Applied Geophysics*, 126:74–86, 2016.
- [122] M. Zhdanov. *Geophysical inverse theory and regularization problems*, 2002.
- [123] M. Zhdanov. *Geophysical inverse theory and regularization problems: Methods in geochemistry and geophysics*. Elsevier Amsterdam, 2002.
- [124] M. S. Zhdanov. New advances in regularized inversion of gravity and electromagnetic data. *Geophysical Prospecting*, 57(4):463–478, 2009.
- [125] M. S. Zhdanov, R. Ellis, and S. Mukherjee. Three-dimensional regularized focusing inversion of gravity gradient tensor component data. *Geophysics*, 69(4):925–937, 2004.
- [126] M. S. Zhdanov, A. Green, A. Gribenko, and M. Cuma. Large-scale three-dimensional inversion of earthscope MT data using the integral equation method. *Izvestiya, Physics of the Solid Earth*, 46(8):670–678, 2010.